Pontifícia Universidade Católica
do Rio de Janeiro

João Gabriel Giesbrecht Formiga Paiva

Pulsed Laser Ablation of Iron and Nickel Targets in Water and its Implications in Astrochemistry

Dissertação de Mestrado

Dissertation presented to the Programa de Pós-Graduação em Física of PUC-Rio in partial fulfillment of the requirements for the degree of Mestre em Ciências - Física.

Advisor : Prof. Dr. Tommaso Del Rosso
Co-advisor: Prof. Dr. Daniele Fulvio

Rio de Janeiro
April 2021

Pontifícia Universidade Católica
do Rio de Janeiro

João Gabriel Giesbrecht Formiga Paiva

Pulsed Laser Ablation of Iron and Nickel Targets in Water and its Implications in Astrochemistry

Dissertation presented to the Programa de Pós-Graduação em Física of PUC-Rio in partial fulfillment of the requirements for the degree of Mestre em Ciências - Física. Approved by the Examination Committee:

Prof. Dr. Tommaso Del Rosso
Advisor
Departamento de Física – PUC-Rio

Prof. Dr. Daniele Fulvio
Co-advisor
Departamento de Física – PUC-Rio

Prof. Dr. Geronimo Perez
UFF

Prof. Dr. Jefferson Ferraz Damasceno Felix Araújo
Departamento de Física – PUC-Rio

Rio de Janeiro, April 23rd, 2021

João Gabriel Giesbrecht Formiga Paiva

Graduado em Física Bacharelado pela Universidade do Estado do Rio de Janeiro(UERJ, 2018)

Bibliographic data

Paiva, J. G. G. F.

Pulsed Laser Ablation of Iron and Nickel Targets in Water and its Implications in Astrochemistry / João Gabriel Giesbrecht Formiga Paiva; advisor: Tommaso Del Rosso; co-advisor: Daniele Fulvio. – Rio de Janeiro: PUC-Rio, Departamento de Física, 2021.

v., 130 f: il. color. ; 30 cm

Dissertação (mestrado) - Pontifícia Universidade Católica do Rio de Janeiro, Departamento de Física.

Inclui bibliografia

1. Física – Teses. 2. Matéria Condensada – Teses. 3. Ablação por Laser Pulsado;. 4. Nanopartículas Magnéticas;. 5. Nanoestruturas de carbono;. 6. Intemperismo espacial;. I. Del Rosso, Tommaso. II. Fulvio, Daniele. III. Pontifícia Universidade Católica do Rio de Janeiro. Departamento de Física. IV. Título.

CDD: 620.20

To my aunt Mônica Giesbrecht

Acknowledgments

First of all, I would like to thank Prof. Tommaso Del Rosso and Prof. Daniele Fulvio for all the guidance, patience, support, advice and all the great amount of teachings about parts of Physics that I practically did not know. I am very grateful to have worked and learned a lot with you two throughout my Master's. Thank you both so much!

I would also like to thank Prof. Geronimo Perez, Dr. Braulio Soares Arcanjo, Prof. Gino Mariotto, Prof. Yutao Xing, Prof. Omar Pandoli and Prof. Jefferson Ferraz for their collaboration with our group and for providing extremely important experimental data for this dissertation.

I also need to thank to now Dr. Tahir for the patience in teaching me very important experiments and for always helping me when he could throughout my Master's Degree.

I am very grateful to my parents, Tânia and Alípio, who have been always given me a great deal of support since when I decided that I would like to study Physics. If I didn't have your support and incentives, I probably wouldn't have made it this far. Immense gratitude to be their son.

I also thank all the support of my family, especially my uncle Dr. Carlos Maurício Chaves, who also encouraged me to do Physics and was always following my journey.

I would also like to thank the many friends I made at PUC-Rio and who were always on my side when they could, whether helping with Physics doubts or talking about life. Lucas, Pedro, Carol, Vinícius, Igor Brandão, Igor Ulrichsen, Antônio, Suellen, Fernanda, Cíntia, Gleice, Eloi, Luciano, Quaid, Matheus Samuel, Matheus Seixas, Judson, Aline, André, Francisco, Alexandre, Pablo, Felipe, Gabriel, Flávio, Shuai, Yan, Arthur, Rian and Bruno. Thank you all for our friendship! I also thank my friends from Recreio and graduation who have been given me great support so far, especially Daniel, Breno, Victor, Carol, Gabriel, Louise, Julio, Bruno, Thales, Kevin and Fellipe. Thankful that our friendship has lasted since school and university!

I thank all Professors and members of the Department of Physics at PUC-Rio for hosting me in the Master's Degree and always helping me with the course when they could. I have immense respect for you.

Finally, but not less important, I would like to thank CNPq and CAPES for their important financial support. Without them, this research couldn't be done.

This study was financed in part by the Coordenação de Aperfeiçoamento de Pessoal de Nível Superior - Brasil (CAPES) - Finance Code 001.

Abstract

Paiva, J. G. G. F.; Del Rosso, Tommaso (Advisor); Fulvio, Daniele (Co-Advisor). **Pulsed Laser Ablation of Iron and Nickel Targets in Water and its Implications in Astrochemistry**. Rio de Janeiro, 2021. 130p. Dissertação de mestrado – Departamento de Física, Pontifícia Universidade Católica do Rio de Janeiro.

The proposed research points to the possibility to perform CO2 reduction reaction (CO2RR) to solid carbon nanomaterials by the pulsed laser ablation (PLA) of magnetic target of iron (Fe) and nickel (Ni) in pure deionized water. The synthesized colloidal dispersions were characterized by different optical spectroscopies (UV-Vis, ICP-MS, FTIR and Raman) and transmission electron microscopy (TEM), revealing the presence of nanosized transition metal oxide and hydroxide nanoparticles, together with organic nanomaterial. The latter is well visible by TEM, energy-dispersive X-Ray spectroscopy (EDS), electron energy-loss spectroscopy(EELS), and Raman spectroscopy, which indicates the presence of amorphous graphitic carbon and CH vibrations. In the case of Ni derived nanomaterial, FTIR results confirm the presence of a beta-Ni(OH)2 hydroxide phase, while Raman and TEM measurements suggest also the presence of Ni(HCO3)2 nanosheets. The experimental results were finally discussed in the frame of the origin and evolution of simple and complex molecules of astrochemical interest, with special focus on those species potentially formed on the surface of metallic minor bodies in the solar system and cosmic dust grains in the interstellar medium(ISM).

Keywords

Pulsed Laser Ablation; Magnetic Nanoparticles; Carbon Nanostructures; Space Weathering;

Resumo

Paiva, J. G. G. F.; Del Rosso, Tommaso; Fulvio, Daniele. **Ablação por Laser Pulsado de Alvos de Ferro e Níquel em Água e suas Implicações em Astroquímica**. Rio de Janeiro, 2021. 130p. Dissertação de Mestrado – Departamento de Física, Pontifícia Universidade Católica do Rio de Janeiro.

A pesquisa aponta para a possibilidade de realizar a reação de redução de CO2 (CO2RR) para a formação de nanomateriais de carbono por ablação a laser pulsado(PLA) de alvos magnéticos de Ferro(Fe) e Níquel(Ni) em água pura deionizada. Os materiais coloidais sintetizados foram caracterizados por diferentes técnicas de espectroscopias ópticas (UV-Vis, ICP-MS, FTIR e Raman) e microscopia eletrônica de transmissão (TEM), revelando a presença de nanopartículas de óxidos e hidróxidos de metais de transição, junto com nanomaterial orgânico. Esse último, é bem visível por TEM, espectroscopia de raio-X por dispersão em energia (EDS), espectroscopia por perda de energia de elétrons (EELS), e espectroscopia Raman, que indica a presença de carbono amorfo grafítico e vibrações CH. No caso do nanomaterial obtido do Níquel, os resultados FTIR confirmam a presença da fase do hidróxido beta-Ni(OH)2, enquanto as medidas Raman e TEM sugerem também a presença de nano-folhas de Ni(HCO3)2. Os resultados experimentais foram enfim discutidos no contexto da origem e da evolução de moléculas simples e complexas de interesse astroquímico, com foco especial nas espécies potencialmente formadas na superfície de pequenos corpos metálicos do Sistema Solar e grãos de poeira cósmica do meio interestelar.

Palavras-chave

Ablação por Laser Pulsado; Nanopartículas Magnéticas; Nanoestruturas de carbono; Intemperismo espacial;

Table of contents

List of figures

List of tables

Somewhere, something incredible is waiting to be known

Carl Sagan, .

List of Abbreviations

NPs –Nanoparticles
$(NPs)^{mix}$ – NPs mixed
$(NPs)^{pr}$ – NPs precipitant
$(NPs)^{sp}$ – NPs supernatant
PLA – Pulsed Laser Ablation
LASiS – Laser Ablation Synthesis in Solution
ICP-MS – Inductively coupled mass spectroscopy
HRTEM – High Resolution Transmission Electron Microscope
TEM – Transmission Electron Microscope
SAED – Selected area electron diffraction
EDS – Energy-dispersive X-Ray spectroscopy
EELS – Electron energy-loss spectroscopy
FTIR – Fourier-transform infrared spectroscopy
PL – Photoluminescence
WS – Water splitting process
FT – Fischer-Tropsch mechanism
ISM – Interstellar medium

1
Introduction

1.1
State of Art

The first synthesis of metal-oxide nanoparticles (NPs) by pulsed laser ablation in liquid solution (LASiS) was demonstrated by Patil et al. in research on the formation of a metastable form of iron [1]. Since then, several laboratories in the world have contributed to advances in research on LASiS, and the number of publications and citations in this field, per year, increased from five publications and five citations to about 50 publications and 700 citations, from 1998 to 2011, respectively [2].

Many advances have been made in the control of NPs size and stability, as well as in their composition [3, 4]. A fundamental point accepted by the entire scientific community is that the composition of the NPs core is the mirror of the target composition, at least when LASiS is performed in water [3, 4].

From this research, we reinforce the introduction of a new paradigm regarding NPs composition, as observed previously in the *NanoLaserLab* of the Department of Physics of PUC-Rio, Rio de Janeiro, Brazil [5]. In those previous studies, we observed the synthesis of molecular organic material and different kinds of carbon nanostructures during the pulsed laser ablation (PLA) of Au, Ag and Fe targets in water, without the addition of surfactants or organic stabilizing agents. These results were explained based on a CO_2 reduction reaction (CO_2RR) to solid carbon (CO_2/C) [6]. We suggested that the reactions induced by PLA are possible due to the catalytic properties of transition metals and transition metal oxide domains present in the synthesized nanoparticles [7, 8].

In the study presented here, we continued the investigation on Fe targets, and investigated the possibility to perform CO_2RR by PLA of nickel (Ni) in water environment, without the addition of any solute in the water. The presence of carbon based material has been detected, in the case of Fe target, by electron energy-loss spectroscopy(EELS) and energy-dispersive X-ray spectroscopy(EDS) and, in the case of Ni target, by Raman spectroscopy and EDS. The results showed by Raman spectra of Ni NPs evidenced the

presence of amorphous graphitic carbon, with characteristic peaks in the region of (D band) 1349 cm^{-1} and (G band) 1590 cm^{-1} [9, 10], and CH_2 and/or CH_3 stretching, with peaks around the region of 2900 cm^{-1}.

Moreover, TEM investigation of the colloidal dispersion obtained by LASiS in water on Ni targets revealed the presence of nanostructures different from small spherical nanoparticles. Specifically, we found nanostructures, containing both the respective nickel, carbon and oxygen atoms. And very similar to the $Ni(HCO_3)_2$ nanosheets as reported by X.Zhang et al. [11]. The presence of the carbonate group $CO_3{}^{-2}$ could in fact be the reason for an intense and sharp Raman peak close to 1100 cm^{-1} observed in different regions of the samples of Ni NPs. Further studies are necessary to draw conclusions on these structures, especially X-ray diffraction (DRX) and X-ray photo-electron spectroscopy (XPS), which have not been possible due to the limited access to most of the laboratory infrastructures during the COVID-19 pandemic [12].

Another important experimental result found in our research consists of the dimension of the synthesized metal-oxide NPs. While most of the literature on PLA of Fe targets in water report small linear dimension of 17 nm for Fe NPs [13] and 3-5.3 nm for Ni NPs [14] using pulses at the wavelength of 532 nm, we demonstrate that under specific experimental conditions,it is possible to synthesize NPs with an average diameter of about 2 nm using laser pulses at the wavelength of 532 nm, with potential applications in gene therapy in human cells [15, 16].

Moreover, the simple magnetization separation method we used allowed in the case of Fe target to identify families of nanoparticles with different average sizes, thus making it possible to obtain a sharper statistical distribution of the size of the NPs colloidal dispersion [5].

Considering the Ni derived nanomaterial, it didn't show a clear difference of average sizes after the implementation of the same magnetization separation method. In addition, by Fourier-transform infrared spectroscopy(FTIR) and Raman spectroscopy, we observed the presence of β-$Ni(OH)_2$ and NiO in our Ni NPs samples.

The experimental results, especially related to the identification of organic nanomaterial, are important, not only for material sciences, but also for astrochemistry. In fact, from the physical point of view, the use of the LASiS technique has been largely reported in the literature for laboratory simulation of the space weathering of objects of astrophysical interest [17, 18, 19, 20]. In the case of Fe and Ni, for example, they are material components present in the composition of minor bodies of the Solar System (such as asteroids, comets, satellites, or planets) and cosmic dusts of the Interstellar Medium(ISM)

[21, 22, 23]. Moreover, ice containing carbon based organic and inorganic molecules, such as carbon monoxide, carbon dioxide and methane is present around them, and may be simulated in a first approximation by the presence of water environment during the PLA process.

It's assumed in different studies that the interactions between minor bodies of the Solar System and micrometeorites, or between cosmic dust grains in the ISM could induce Fischer-Tropsch(FT) reactions, which may lead to a conversion of the CO and CO_2 present in the ice into organic molecules on their surfaces [24, 25, 20].

The formation of organic material through FT reactions happening over these astrophysical bodies could be related to the observed production of organic nanomaterial during the PLA synthesis process. In this frame, we suppose that Fe and Ni oxide nanomaterials formed during the interaction between micrometeorites and asteroids, or between cosmic dusts, could assist in the catalysis of CO_2 reduction reactions.

1.2 Objectives

The main objective of the present research was to demonstrate the possibility to perform the CO_2RR by PLA of Fe and Ni targets in an aqueous medium and relate the experimental results to the current theoretical framework on the formation and evolution of complex molecules in the space environment.

The research needed to achieve this main objective, involves different experimental techniques, aiming at both the synthesis and the characterization of the produced nanomaterials. In this context, we can make a list of objectives of the research, in particular:

1) Determination and control of the NPs size;

2) Observation and identification of the metal-oxide (or hydroxide) NPs by TEM, EDS, EELS, FTIR and Raman;

2) Observation and identification of carbon-based material by TEM, EDS, EELS, FTIR and Raman.

1.3 Contributions and infrastructure

The synthesis of nanomaterial by LASiS was made in the *NanoLaserLab* of the Department of Physics of PUC-Rio, under the supervision of Prof. Dr. Tommaso Del Rosso. In the same department, the Optical Spectroscopy Multiuser Laboratory also provided the apparatus for the NPs characterization

by UV-Vis spectroscopy and Fourier-transform infrared spectroscopy (FTIR). ICP-MS measurements were performed in the Department of Chemistry of PUC-Rio.

Collaborations with other institutes were also established to perform transmission electron microscopy(TEM), energy-dispersive X-ray spectroscopy(EDS), electron energy-loss spectroscopy(EELS) and Raman spectroscopy. The TEM and EDS measurements were performed by Prof. Dr. Geronimo Perez from the Department of Mechanical Engineering of the Federal Fluminense University (UFF) and Dr. Braulio Soares Archanjo from the National Institute of Metrology, Standardization and Industrial Quality of Rio de Janeiro (INMETRO). As for the EELS, the measurements were performed by Prof. Yutao Xing of the Institute of Physics of the Federal Fluminense University(UFF).

Prof. Dr. Gino Mariotto from the Department of Informatics of the University of Verona (Italy), performed Raman spectroscopy on the Ni NPs samples.

1.4 Organization

In Chapter 2, "Theoretical references", we show the most important concepts necessary to understand the topics of our research. We present the theory of LASiS of metal targets, and the information about the differences observed in the NPs formation by variation in the laser parameters, solutes, solvents, and the metal targets itself. We describe the typical Fe and Ni based oxide and hidroxides present in nature, and finally highlight our theoretical proposal [5] on the formation of organic material by CO_2RR during LASiS, and its relationship with astrochemistry.

In Chapter 3, "Instrumentation and experimental methods", is initially presented the experimental set-up and procedures used for the synthesis of nanoparticles by LASiS. Afterward, we briefly describe the other experimental techniques used for the characterization of nanomaterials, such as TEM, EDS, EELS, UV-Vis, ICP-MS and Raman spectroscopies.

In Chapter 4, "Results and discussions", we present the obtained experimental data and discuss the results, comparing them with those found in the literature.

In Chapter 5, "Conclusions", we summarize the conclusions on the experimental results and briefly introduce a list of characterization techniques still needed to conclude the research.

2
Theoretical references

2.1
Astrophysics background

With the objective of describing the astrochemical and astrophysical relationship with the laser ablation methodology, we first need to give a short background for the sake of the reader's understanding. For this, we will provide, in the next two subsections, a general description of the Solar System and the interstellar medium.

2.1.1
Minor bodies of the Solar System

Firstly, it is possible to describe any stellar system as the group of objects in space bounded with a star by means of gravitational force. In the case of Earth, our stellar system is known as Solar System and this term will be used through out this dissertation.

As for the objects that composes the Solar System, there is our star, the Sun in the center of it, the planets circulating the Sun on elliptical orbits, the satellites orbiting those planets, asteroid belts, located between Mars and Jupiter, constituted by a group of various sizes of rocks, and the comets, bodies that are made of ice and rocks coming from the outer regions of the Solar System. All of them with exception of the Sun and the eight planets can be named as the minor bodies of the Solar System.

Specifically, asteroids are a group of minor bodies with great relevance, considering that we have direct information about their composition by studying the meteorites, the rocks that enter Earth's atmosphere and reach its surface. Different studies were and are continuously done on meteorites to infer their elemental composition and mineralogical properties. The information extrapolated by studying meteorites can help us to better understand the origin and evolution of the whole Solar System and their components. In the case of this research, we mainly focus on the class of iron meteorites, which present a great amount of Fe in their composition as well as Ni, both metals that were used as targets for the PLA experiment. Despite this, our results can also be

applied, to some extent, to the class of stony-iron meteorites, i.e., those meteorites which, besides silicates, also present Fe and Ni in their composition. For example, it was observed in pallasites, a rare class of stony-irons meteorites, that their metal composition could be similar to the one of some iron meteorites, but with a higher quantity of nickel, around 7-13 % (in wt %) [26].

2.1.2 Interstellar medium and cosmic dust

In space, the region between the stellar systems, it is commonly called interstellar medium(ISM). In these regions, besides the radiation commonly present in space in various wavelengths, are found molecular and atomic gases, interstellar ices and cosmic dust [23].

Astronomers define cosmic dust as the solid component made of carbons and silicates. The typical dimensions of cosmic dust grains are below 1 μm, but they can be even smaller, in the order of 0.001 μm [23]. The envelopes, or external layers, surrounding the stars are the sources of such dust grains, since they may be composed of silicates, oxygen and carbons. The dust could then come to the interstellar region via the radiation pressure due to the star, opposing its gravitational field [23].

But there is also the possibility of them being produced by a supernova, one of the final events occurring in the lifetime of stars. The supernovae explodes, liberating matter and radiation throughout the surrounding space [23].

Moreover, the dust that would come from circumstellar regions and supernova sources can mix with other elements and molecules present in the interstellar medium.

For the focus of this research, both silicate and carbon cosmic dust are important. Silicate cosmic dust could come from the red giant stars, a higher state of stellar evolution, where the stars are rich in oxygen. Silicate cosmic dust is also thought to be mainly made by SiO_4 alongside other elements, which could be magnesium and even iron [23].

Carbon cosmic dusts may be in the form of fullerenes, graphites, nanodiamonds and amorphous carbons [23]. Also, this type of dust can be made in stars that evolved until forming carbon inside of it. The carbon is later ejected in the surrounding space, creating the core of carbonaceous cosmic dust grains.

2.2 Laser Ablation Synthesis in Solution(LASiS)

Laser ablation is an experimental technique of great relevance today, especially when considering its applications in areas such as pulsed laser thin films deposition and synthesis of nanomaterials [27, 3, 4].

The term "ablation" defines the removal of surface atoms [28]. When using laser pulses, the removal is due to the interaction between the photons and the target's surface, allowing the formation of a plasma over the region of interaction with the target, which contains ions from both the solid target and the environment, the latter constituted by the liquid (L) and the gaseous species (G) dissolved inside [28]. In the case of interest of the present research, the metal (M) is Fe or Ni, the liquid is water, and the dissolved gases are the ones constitutive of air (CO_2, N_2, O_2). In Figure 2.1, it is represented the plasma plume created over the target. Depending on the distance from the target, the temperature will decrease (ambient temperature in the liquid direction), and different species (M, L, G) will be in the excited or ionized state, denoted with an asterisk. In comparison to the traditional literature, we insert the gaseous species dissolved in the water, as an important component participating to the chemical and physical properties of the nanomaterials synthesized by LASiS. In particular we put attention to the small percentage of CO_2 present in the air (~ 0.04 % partial pressure) [29], and attribute the presence of organic nanomaterial in the colloidal dispersion, to the reaction of reduction of the gas dissolved in the water environment during LASiS.

In the next subsections will be presented the phenomenology of LASIS, considering $t = 0$ as the instant in which the laser pulse hits the target. These principal steps occurring during LASiS are represented in Figure 2.2.

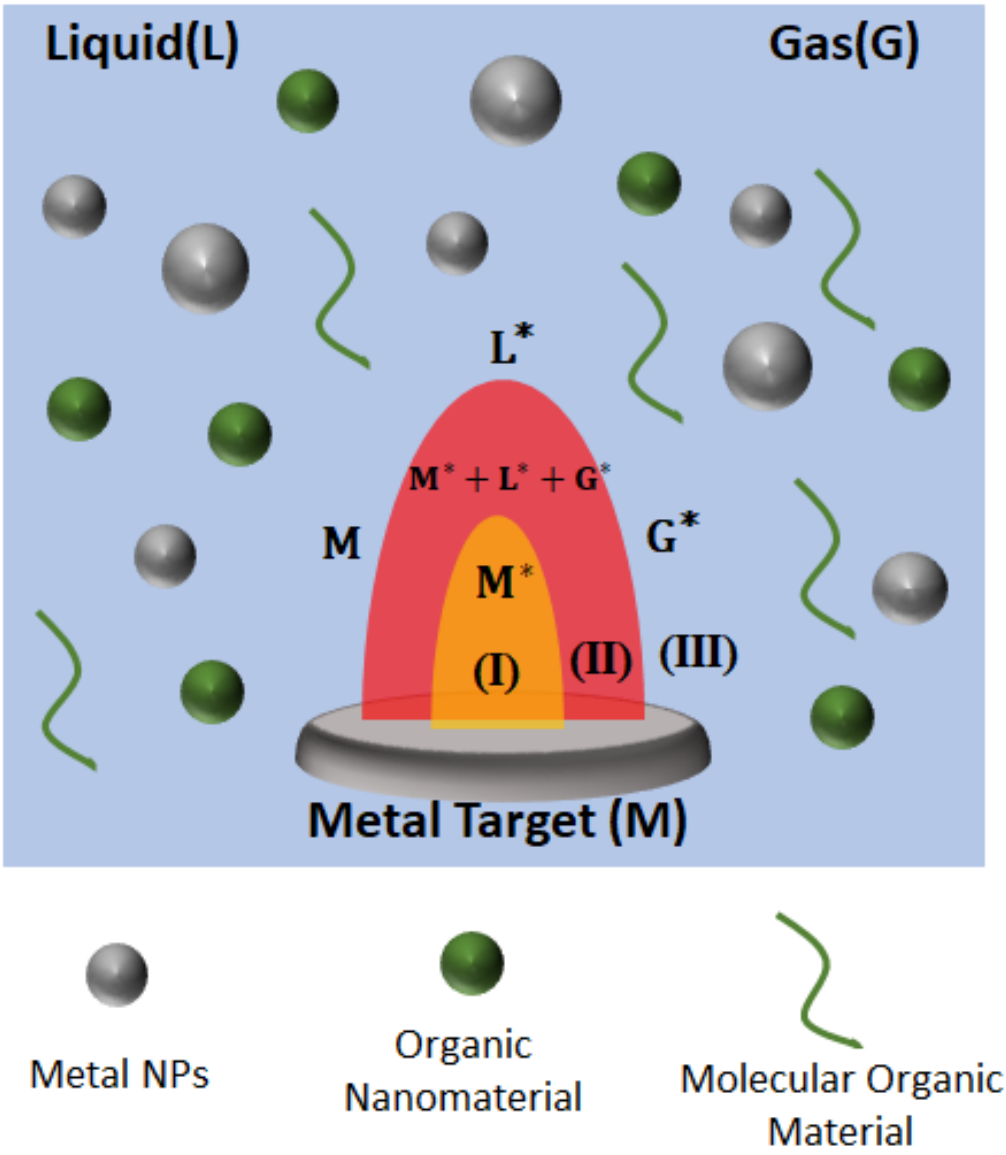

Figure 2.1: Representation of the plasma plume generated after interaction between laser and the metal target. The plasma contains a region (I) near to the target which is only constituted by metal ions(M^*) and a second region (II) where it's present a combination of ions and excited species of metal(M), liquid (L) and gas(G), symbolically represented by M^*+ L^*+ G^*. Near above the plasma, the region (III) classify the liquid medium cointaining metal species(M) and ionized species of the liquid (L^*) and gas (G^*). At the bottom of the figure are represented the symbols used for the identfication of metal NPs, organic nanomaterial and molecular organic material.

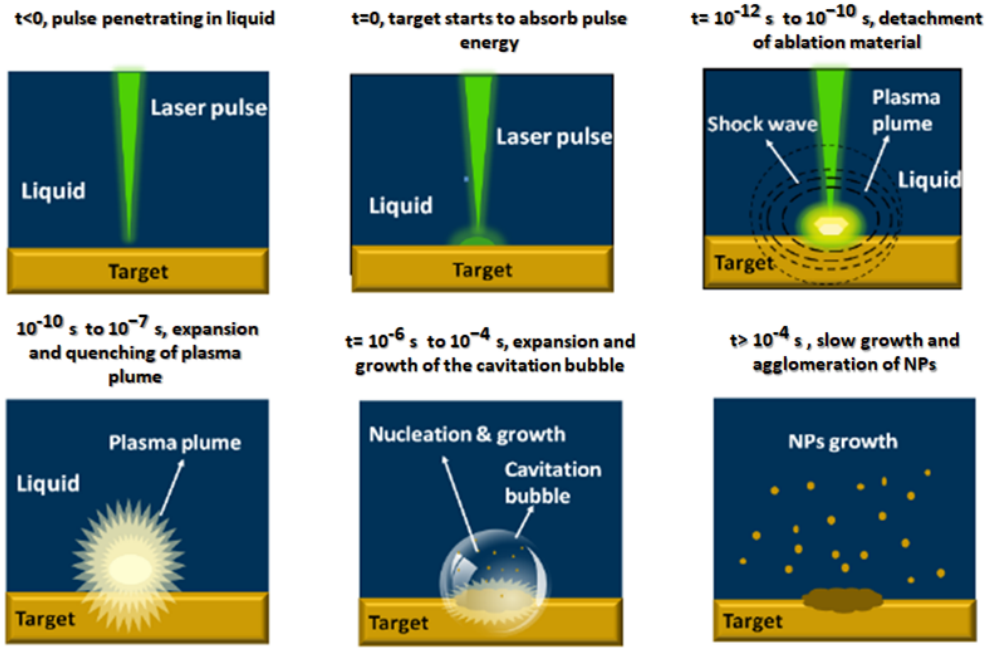

Figure 2.2: Temporal scheme of the various processes involved in LASiS. Adapted from [3, 5].

2.2.1
Laser pulse absorption by the liquid

In t<0, the laser pulse is emitted and penetrates the liquid, before reaching the target. Considering the interaction between the laser and the liquid, nonlinear optical effects and multiphoton absorption by the liquid can happen and may affect the whole ablation process. The possibility to trigger nonlinear optical effects depends on the working fluence F (measured in J/cm^2, which is, respectively, the energy divided by the area of interaction) used in the ablation , and the solvent of the liquid environment [3, 30, 31]. The nonlinear optical effects may be accompanied by breakdown of the liquid molecules which, in the case of water, produce principally an oxygen-hydrogen plasma, with both free and solvated electrons, radicals ·OH and ·H as transient elements, and O_2, H_2 and H_2O_2 as stable products [32, 33] Anyway, laser induced breakdown of water is most easily accomplished with ultra-short laser pulses (ps, fs) [34], and may be reached by ns pulses at the wavelength of 532 nm only with fluences as high as 100 J/cm^2 [35], which is more than one order of magnitude higher than the value of F used in the present research. Hence, we exclude that the laser pulses used might provoke the production of a significant amount of direct optical breakdown of water, which is instead triggered by the formation of the plasma plume during the ablation of the solid target.

2.2.2
Laser pulse absorption by the target

When the laser pulse finally hits the target in t=0, there is an instantaneous absorption of photons by the electrons of the solid, in which the thickness of the region of interaction is proportional to the material skin depth [3, 36].

Since the density of photons is high during this step, linear and nonlinear absorption occur in the target. Both of them depend on the intensity of the electric field in the target, which depends on the fluence F and the pulse duration [3, 36].

2.2.3
Detachment of the target material

After absorption of the laser by the target, the excited electrons transfer their energy to phonons until both reach thermal equilibrium (i.e. electron-phonon thermalization) in a time scale of about 10^{-12} s (1 ps). In sequence, the detachment of the material from the region of interaction begins. The detached material is ejected in the form of clusters of liquid drops, electrons, ions and atoms, forming the so-called plasma plume [3, 37].

Depending on the difference of the duration of the laser pulses and the electron-phonon relaxation time (of the order of ps), distinct mechanisms are involved in the material detachment process [3, 4].

For example, in ultrashort pulses duration, which is of the order of fs and ps, the electron-phonon thermalization is reached on a time scale larger than the pulse duration, so that processes like multiphoton absorption and photoionization are predominant [5, 3]. Moreover, there is an ultra-fast heating in this case, far from the thermodynamic equilibrium, and the detachment of the material is called fragmentation[3].

In contrast, in the case of a pulse duration of the order of ns(similarly to the case of the laser source used in the present research), electron-phonon energy transport may occur before the end of the laser pulse, leading to the possibility of describing the removal of material by classical thermodynamics [3, 38]. So, alongside vaporization and melting of the material, "explosive boiling" phenomena occur, which consists of rapid and high heating of the material at a thermodynamic critical temperature [5, 3, 38].

After a time of about 10^{-10} s, the recoil pressure of the ejected material can generate a shockwave propagating in the direction of the target and a specular one propagating into the liquid with a supersonic velocity of the order of 10^3 m/s [3]. The propagation of the shockwaves in the target and liquid, may carry between 10 to 50 % of the pulse energy, and also allows the detachment of the material from the region where the laser hits [3].

2.2.4 Plasma plume expansion and confinement

Due to a great amount of kinetic energy in the plasma after its formation, it expands on a time scale of about 1 ns [39, 40]. Then, the confinement of the plasma occurs by the action of the buffer produced by the liquid [3]. Considering that the heated plasma species transfer their thermal energy to the external regions of the metal targets, the heating of the target by the plasma lasts some nanoseconds after the end of the laser pulse [3, 39, 40]. Together with the target, the plasma also transfers thermal energy to the surrounding liquid, cooling itself, and creating an external region formed by the plasma species and excited molecules or atoms constituting the surrounding medium, as depicted in Figure 2.1. It is interesting to note that exist a part of the plasma (II), just above the region constituted by the only metal species (I), where the ions and excited species come from metal (M), liquid (L) and gaseous (G) components.

This expansion and cooling of the plasma occur on a time scale of about

10^{-7} s [3].

2.2.5
Cavitation bubble generation

After the plasma is extinguished and its thermal energy is transferred to the liquid, a cavitation bubble is generated, emerging between 10^{-7} and 10^{-6} s. [3, 40, 5]

The cavitation bubble expands, traveling at a supersonic velocity of about 10^3 m/s for a distance of the order of mm until 10^{-4} s. At this moment, the cavitation bubble internal pressure becomes lower than the external pressure caused by the liquid, and the bubble collapses, emitting the second shockwave of the whole process [3, 41, 42]. To have an idea of its time length, Wagener et al. observed that the total duration of the cavitation bubble was estimated at approximately 350 μs [43].

Moreover, when the cavitation bubble collapses, secondary bubbles appear, called persistent microbubbles or permanent bubbles, as shown in Figure 2.3 [44, 45]. This type of bubble can last for a range of milliseconds, visible for a longer time than the cavitation bubbles [45]. The persistent microbubbles may act as a shield, absorbing part of the laser pulse energy and interfering with the interaction between the laser pulse and the target in LASiS [44, 45, 5]. Gases, such as H_2, O_2, H_2O_2 and N_2, were also identified inside these microbubbles made in PLA using various transition metals immersed in water [44]. Specifically, these results were found by Kalus et al., using gas chromatography [44]. Their appearance is associated to the nanoparticle laser-induced water breakdown, with water splitting (WS) process [44, 32]. As we are going to see in a posterior section, the persistent microbubbles will be essential objects to sustain our proposal on the CO_2RR during LASiS in water.

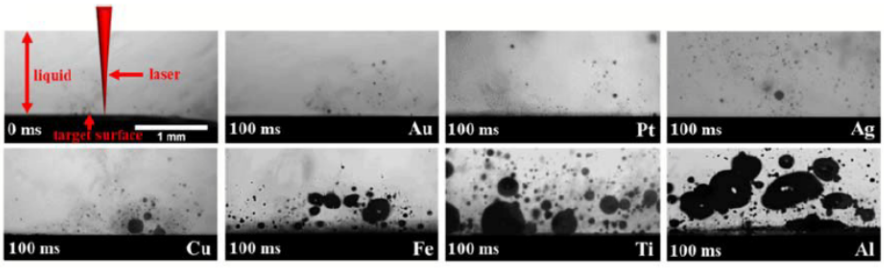

Figure 2.3: Shadowgraphs of persistent microbubbles observed during PLA of Au, Pt, Ag, Cu, Fe, Ti and Al targets immersed in water after a delay of 100 ms. Taken from [44].

2.2.6
Growing of nanoparticles

It is not clear what is the step where nanoparticles are effectively formed. Probably, a part of the NPs are formed during the plasma expansion and carried at the surface of the cavitation bubble , and another part may be generated during the collapse of the bubbles. The growth of NPs happens by the coalescence of small clusters, which is reflected in the polycrystalline nature of the nanomaterials produced by LASiS. In general, the synthesis of NPs by PLA is considered as a combination of both top-down and bottom-up processes [3, 4, 40]. The top-down process is related to the formation of the plasma [3, 4, 40], and the bottom-up process, to the recombination of the plasma in small clusters and their following coalescence [3, 4, 40].

2.3
The effects of laser pulse parameters: duration, fluence and wavelength

It was mentioned before that a variation in the pulse duration may contribute to changes in the physical mechanisms involved in PLA, and affects the size distribution of NPs. When using ps and ns laser-pulses, both thermal and nonlinear optical effects are effective in the detachment of the material, and the nanomaterial is generally characterized by a larger statistical distribution of sizes. Better results in term of the polydispersion of the synthesized NPs are obtained when using ns laser pulses. In fact, "plasma shielding" (absorption of the laser pulse energy by the plasma) occurs with laser-pulses with duration higher than 10^{-10}, so that the temperature and pressure of the plasma increases in the process [3, 36], with the possibility that the liquid drops present in the plasma plume may be further vaporized, enhancing the uniformity of the species present in the plasma, which will subsequently recombine in the form of NPs. This is the reason why, in most of the cases, a monomodal log-normal function is used to describe the statistical distribution of the nanomaterial size, when ns laser pulses are used [3, 4].

In general, also the variation in the laser fluence may affect the sizes and the production rate of the nanoparticles [46]. In the case of ns laser pulses with lower fluences, the target material is mostly removed by evaporation, with the subsequent nucleation of the vaporized atoms [46]. Nevertheless, with the increase in laser fluence, a great amount of energy is released to a large part of the target, causing also melting to occur , enhancing both the average size and production rate of the NPs [46]. This effect, was for example recorded by Lasemi et al., who observed that an increase in laser pulse fluence for Fe and Ni targets, resulted in an increase in the average size and width distribution

of NPs [47, 48].

The size distribution of the produced NPs also depends in a complex way on the laser pulse wavelength , whose effects also depend on the nature of the ablated material [13, 49]. For instance, it is known that the process of photo-fragmentation occurs in the case of Au NPs when laser pulses at the wavelength of 532 nm are used, with a narrowing of the size distribution [133, 134].

As for Fe NPs, it was observed a decrease in the average diameter of NPs from 17 nm to 7 nm with an increase in the wavelength, changing 532 nm to 1064 nm [13]. The study evidenced that the dispersion of the target absorption was responsible for this observation, so that volume and decay time of the plasma plume was higher with pulses at 532 nm, with the synthesis of bigger nanoparticles[13].

In the case of PLA of Ni in pure water, the research in [14] observed average sizes of NPs around 3-5 nm using laser pulses at 532 nm(8 ns, E = 40 mJ/pulse), while the study in [49] identified a bimodal distribution with one average size of NPs around 10 nm and other around 100 nm using a laser pulses at 337 nm(10 ns, $F = 50$ J/cm^2). The generation of a bimodal distribution was interpreted in the context of two effects: phase explosion(for the NPs with 10 nm) and Rayleigh-Taylor instability(for the NPs with 100 nm) [49]. Phase explosion refers to a process happening when there is a high-intensity pulsed laser ablation, which promotes a homogeneous nucleation and forms a combination of nanoscale droplets and vapor [49]. As for Rayleigh-Taylor instability, it can occur when a very dense fluid is pushed against a low density fluid by an acceleration, such as gravity [49]. This may result in an ejection of the molten material to the periphery of the laser spot area, with the formation of larger nanoparticles [49].

2.4 Influence of material parameters

As in the previous section, it is also important to know the effects that the nature of both target and liquid have in the products of LASiS, principally their chemical composition at the end of the synthesis.

2.4.1 Solute

The use of solutes in the LASiS experiments allows to enhance the plasma confinement on the target surface, and may control both dimension and stability of the produced nanomaterial. The confinement of the plasma plume is increased by the liquid viscosity, and the presence of surfactant or

stabilizing agents is generally used to control and limit the dimension of the NPs, since they reduce the time available for the interaction and coalescence of the nanoparticles seeds, which are readily surrounded and stabilized by the solutes in the system [3, 50].

2.4.2 Solvent

The solvent is another important parameter, since its chemical nature may influence the characteristics (size, composition) of the nanomaterials [3]. Considering metals such as Au, Ag or Fe, it is well known that their synthesis by PLA in pure water leads to the formation of NPs formed by metal and oxidized species [3, 4]. On the other hand, when particular organic solvents are used (i.e., toluene, hexane, ethanol), a solid carbon shell may be created around the core of the NPs. This effect is represented in Figure 2.4 where is represented an iron oxide NP surrounded by a graphitic shell, obtained by ablation of Fe target in acetone [51].

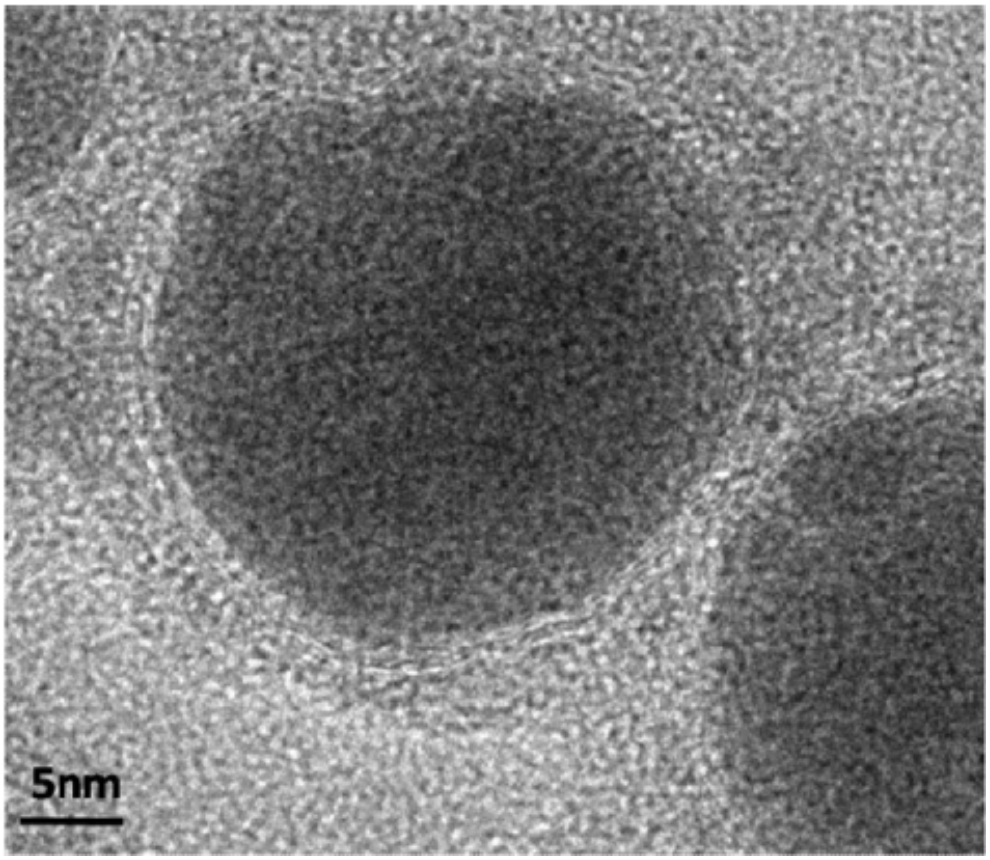

Figure 2.4: HRTEM image presenting a core of iron nanoparticle with a graphitic shell, obtained by PLA of Fe target in acetone. Taken from [51].

2.5
Electronic properties of iron (Fe) and nickel (Ni)

Transition metal targets are particularly interesting in the field of PLA in water since, differently from other materials, they can trigger chemical reactions during the process, as will be described in detail in the next section. In specific, Fe and Ni are important metals even for astrochemistry/astrophysics, considering that they are present in the compositions of different type of bodies from space, as it was mentioned in the first section of this chapter. Thus, this section focus on the description of the physical properties of these fascinating materials, whose use in the development of catalytic reactions is commonly reported in the literature [8, 52].

Considering that this section will deal with general descriptions of these metals and their oxides (and hydroxides, for the Ni case), it is interesting to know that the transition metals are composed of five unstable d-orbitals and one unstable s-orbital in the valence band. These groups of orbitals make possible a higher variety of oxidation states in comparison with alkali/alkaline, which, in contrast, have more fixed oxidation states(+1/+2) [5]. In this sense, the number of unpaired s- and d-orbitals of transition metals are important data, especially when considering that these orbitals can be associated with oxidation reactions and, consequently, to the formation of oxides. The electronic configurations of s- and d-orbitals for Fe and Ni are shown in Figure 2.5.

However, in the context of PLA, the metal ions formed wouldn't be free species in an aqueous environment. They would form a coordination sphere, a structure that connects the metals with the molecules and ions of its environment. A liquid, such as water, would have electrons that interact with the unstable orbitals of the metal ion and form an aqueous complex. If considering water, for example, this coordination sphere would be weak, since this solvent is a weak binder. This would favor interactions between the metal ions and other molecules, such as CO_2 and the hydrogen and hydroxide radicals produced during PLA.

Regarding the oxides, some of these possible compounds of Fe and Ni are inside the group of metal semiconductors. The semiconductors are characterized by having two bands, called valence band (VB) and conduction band (CB), separated by an energetic band called band gap (BG). In semiconductors, it is also possible to excite the electrons from the valence band to the conduction band in different ways, such as in optical, electrical or thermal routes, as shown in Figure 2.6. The excitation of an electron from the VB to the CB, generates a so called electron-hole pair. In this case, the material

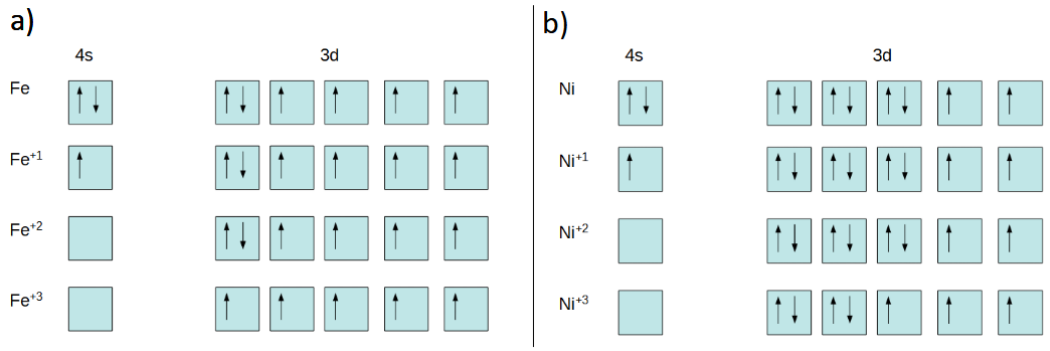

Figure 2.5: (a) Oxidation States of iron.(b) Oxidation states of nickel.

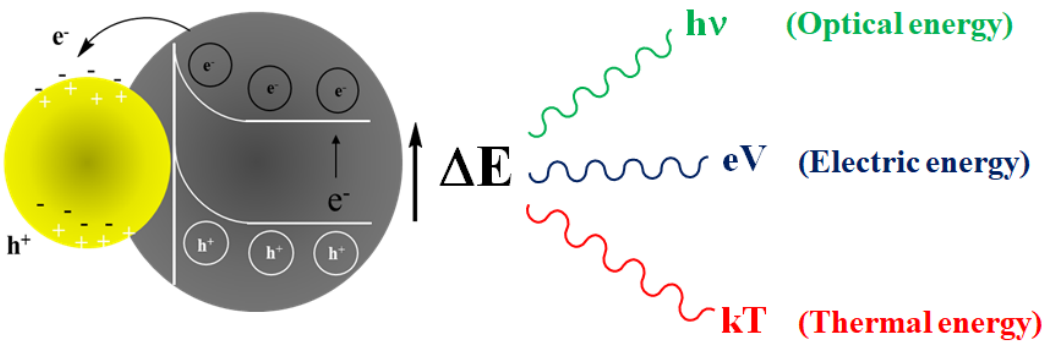

Figure 2.6: Representation of the formation of an electron-hole pair in a semiconductor. The energy necessary to overcome the BG can be obtained by optical, electrical and thermal mechanisms. Taken from [5].

could serve as a donor of electrons, considering the electrons in the conduction band, or a site for the capture of electrons of another compound, considering the holes in the valence band.

Iron oxides

Iron is a ferromagnetic chemical element belonging to group 8 of the periodic table. It is widely present on our planet, distributed in various types of chemical interaction for being very reactive. Furthermore, this metal is widely present in meteorites [21, 22].

Considering that in the present research water is used as solvent, the formation of iron-oxides during LASiS is expected from the literature, as will be explained in subsection 2.5.1. The principal oxidized phases of iron are wustite (FeO), hematite (Fe_2O_3), magnetite (Fe_3O_4), and maghemite (γ-Fe_2O_3).

Wustite, which has an oxidation state of -2, is one of the oxidized forms of Fe. It is characterized as a cubic crystalline structure and is thermally unstable

[53]. It presents a band gap of about 2.4 eV [54].

Hematite has Fe with an oxidation state +3 . It is one of the most stable oxidized forms of iron, and presents weak ferromagnetic interaction at room temperature [5]. Hematite is also a semiconductor, with a band gap between 1.9 - 2.2 eV [55, 54].

Together with hematite, also maghemite has an oxidation state +3, besides being thermally unstable. Its structure can be converted to hematite at temperatures higher than 550 K [56]. This type of oxide has a band gap of 2.0 eV [57].

As for magnetite, it is a material composed of two types of iron oxide with both Fe oxidation states being +2 and +3 and it can be represented by two chemical formulas: Fe_3O_4 or $FeO.Fe_2O_3$. It has efficient magnetic properties, since it is ferromagnetic at room temperature [5]. This compound also has a crystalline structure similar to maghemite and becomes hematite at temperatures higher than 673 K [56]. Magnetite is characterized by a band gap of 0.2 - 0.5 eV [58, 54].

Nickel oxides and hydroxides

Nickel is a ferromagnetic chemical element belonging to group 10 of the periodic table. It has great resistance against corrosion and oxidation and it is also found in some types of meteorites [21, 22].

However, Ni can be present in different forms of oxides and hydroxides.

In respect to the Ni oxides, the most important ones can be classified as: nickel oxide type II (NiO) and nickel oxide type III (Ni_2O_3 and NiO_2).

The first one is a chemical compound with characteristics between semiconductor and insulator, admitting that it has a band gap of energy ranging from $3.6 - 4.0$ eV [59]. It also has properties that favor the possibility of water splitting by photocatalysis, especially in the process of hydrogen evolution [60]. However, it is more used as a cocatalyser, because of the high band gap value [60].

As for Ni_2O_3 and NiO_2, they are inorganic compounds that are not well characterized and do not have clear functionalities either. In addition, some studies have indicated that these chemical compounds have a band gap between 3.3 eV and 3.7 eV [61, 62].

One of the most stable forms of nickel hydroxides are the Ni(II) hydroxides, $Ni(OH)_2$, characterized by a band gap of 3.0-3.5 eV [63]. $Ni(OH)_2$ hydroxides can be found in two phases: β-$Ni(OH)_2$ and α-$Ni(OH)_2$, whose different crystal unit cell is reported in Figure 2.7.

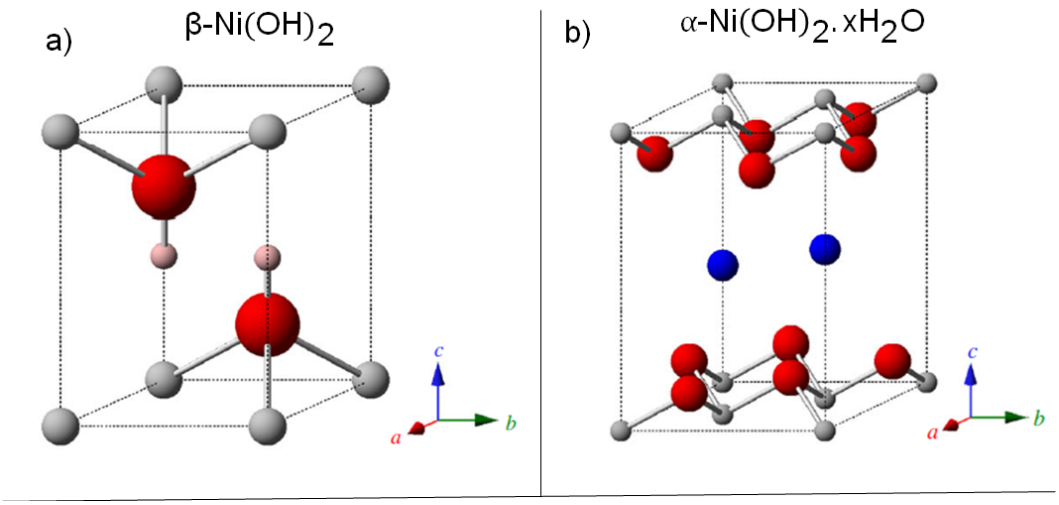

Figure 2.7: Ball-and-stick unit cell representation of (a) molecules of β-$Ni(OH)_2$ and (b) molecules of α-$Ni(OH)_2$ interacting with 2 molecules of H_2O. The large red spheres represent O^{-2}; the medium size grey spheres represent Ni^{+2};the small pink spheres represent H^+; the small blue spheres represent H_2O. Taken from [63].

Specifically, β-$Ni(OH)_2$ appears in nature as a mineral called theophrastite [63, 64]. This phase has a hexagonal scalenohedral symmetry, a similar structure to brucite, $Mg(OH)_2$ [63, 64].

Differently, α-$Ni(OH)_2$ has trigonal symmetry and consists of planes of β-$Ni(OH)_2$ intercalated with water molecules [63, 64]. It can be also denoted as α-$Ni(OH)_2.xH_2O$. Although it might be guessed by Figure 2.7 that the water molecules are in fixed states, this is a wrong assumption. The water molecules are actually free to translate and rotate according to its plane [63]. Their layer, alongside the water molecules itself, can be removed at temperatures of 240-300^o C, decomposing the hydroxide and forming NiO [63].

It is known that α-$Ni(OH)_2$ may have β-$Ni(OH)_2$ planes that not only interact with water molecules, but also anions such as (NO_3^-), sulfates(SO_4^{-2}) and carbonates(CO_3^{-2}) [63, 65]. These structures are defined as α-$Ni(OH)_2$ derivatives, as long as the whole structure is still resembling brucite [63, 65].

Finally, we highlight that also nanostructures of nickel bicarbonate $Ni(HCO_3)_2$ have been reported, both in form of NPs [66] or nanosheets [11], as represented in Figure 2.8.

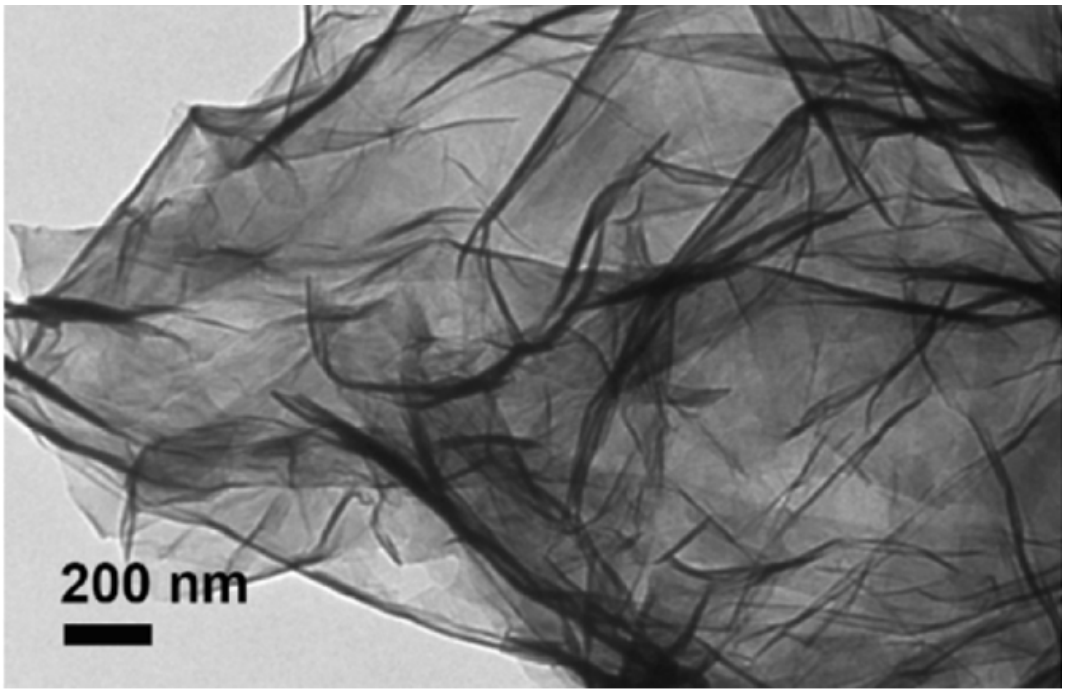

Figure 2.8: TEM image of the $Ni(HCO_3)_2$ nanosheets synthesized by template-free solvothermal method at reaction time of 3 h. Taken from [11].

2.5.1
Fe and Ni oxides and hydroxides obtained by LASiS in water

The LASiS of pure metal iron in water can produce simultaneously all the principal iron-oxides, with majority of magnetite and minor traces of wustite, hematite and maghemite [67, 68, 69].

Considering PLA of pure Ni in water, NiO has been identified in various experiments together with pure metal NPs, whereas the appearance of Ni_2O_3 is still questioned [14, 49, 70]. $Ni(OH)_2$ has been reported by Gellini et al., [70], where it was proposed that Ni^{+2} produced by the oxygen dissolved in water, would generate $Ni(OH)_2$ by the reaction with water. Then, following a dehydration process, this hydroxide compound would transform in NiO [70].

Finally, some studies also identified core-shell types of NPs, with a combination of a metal Ni core with an NiO shell [14, 71].

2.6 PLA-CO_2/C process

In this subsection, we explain the details of our proposal on the reactions leading to the formation of organic material during PLA of Ni and Fe targets in water. We will denote this process as PLA-CO_2/C to indicate the possible final formation of organic material, even in solid nanostructured form.

For this purpose, it's relevant to introduce first the water splitting process (WS), recently observed during PLA of transition metal targets by Kalus et al.[44, 45]. Due to the catalytic properties of the NPs, the molecules of water "split" into two gases, H_2 and O_2, following the reaction

$$2H_2O \rightarrow 2H_2 + O_2. \tag{2-1}$$

As observed by by Kalus et al. [44, 45], the hydrogen and oxygen gases produced in WS are subsequently transported by the permanent bubbles generated during PLA.

In the few works present in literature reporting WS during PLA of metal targets, or during irradiation of pre-fabricated metal NPs in water [44, 45, 32], the authors do not propose an explication of the observed reaction. Our proposal is to justify the WS on the actuation of electron-hole pairs generated in the metal-oxide semiconductors NPs of iron and nickel, and introduce the CO_2 reduction reaction (CO_2RR) as a second possible reaction happening during the PLA process.

Three main characteristics are required to obtain CO_2RR in water: the presence of protons (H^+) or molecular hydrogen (H_2) and electrons (e^-) able to reach the surface of the catalyst [72], an energy source to balance the variation in the Gibbs free energy [73], and a proper catalyst for the CO_2 activation and intermediate reaction products stabilization [74]. As explained before, the extreme thermodynamic conditions of the environment near the metal target during PLA [75] are responsible for water decomposition with the presence of highly reactive radicals ($\cdot$H, $\cdot$OH), H^+, solvated electrons, and also molecular H_2 [44, 76, 32].

It is not clear what is the fundamental energy source involved in the catalytic reactions during PLA in water, which are most probably triggered by the synergetic effect of Bremsstrahlung radiation produced during plasma recombination [137], thermal energy released by the cavitation bubble collapse and supersonic acoustic waves generated during the irradiation of the resulting NPs [76, 77], and the direct absorption of the laser pulse.

In Figures 2.9(a,b) are represented schematically the WS and one-step CO_2RR induced by the excitation of an electron pair in a semiconductor

nanoparticle. The holes (h^+) of the valence band promote oxidation processes and, in contrast, the excited electrons of the conduction band(e^-) promote reduction reactions. In both WS and one-step CO_2RR, the holes promote the water oxidation by the oxygen evolution reaction(OER):

$$2H_2O + 4h^+ \rightarrow 4H^+ + O_2. \tag{2-2}$$

The excited electrons in the conduction band, are instead used in the hydrogen evolution reaction(HER):

$$2H^+ + 2e^- \rightarrow H_2. \tag{2-3}$$

Considering both the reactions, we note that HER is in competition with the one-step CO_2RR, which classically leads to carbon monoxide (CO) and methane (CH_4) as possible major products.

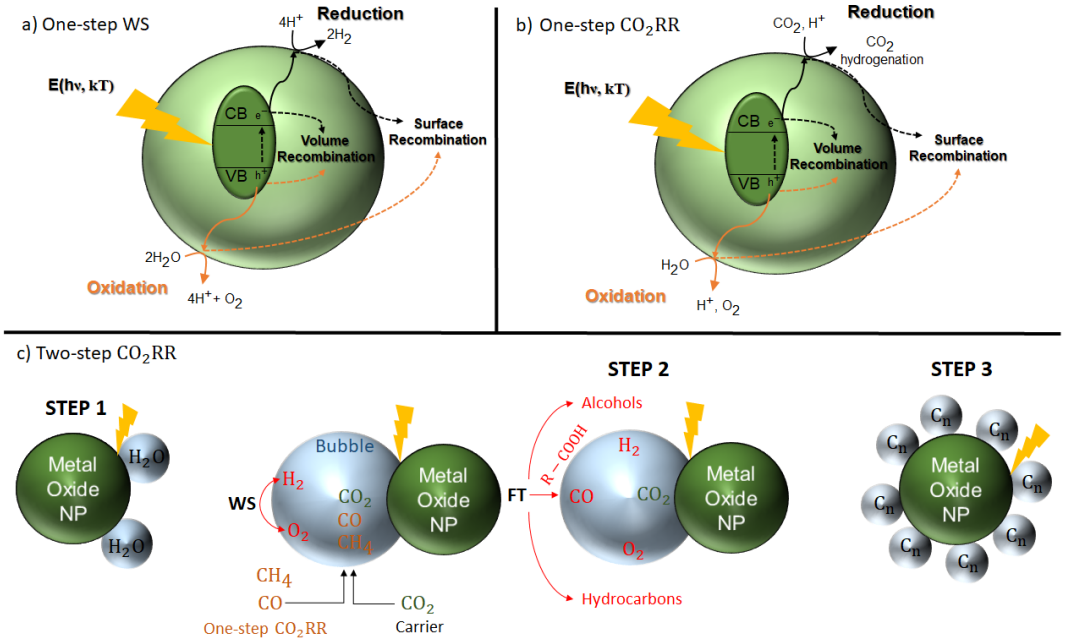

Figure 2.9: Scheme of the proposed PLA-CO_2/C process. (a) Water splitting (WS). (b) One-step CO_2RR. (c) Two-step CO_2RR processes leading to the final formation of solid carbon material. In green are represented the metal oxide nanoparticles, and in blue the permanent bubbles transporting the gases produced during PLA. CB and VB refer to the conduction and valence band of the semiconductor nanoparticle, respectively. Adapted from [5].

With this introduction, we propose a simplified theoretical model of the possible chemical reactions involved during CO_2/C process induced by PLA (PLA-CO_2/C). The proposed mechanism leading to the final formation of the carbon based nanomaterials by PLA-CO_2/C is a complex overlapping of one and two-step CO_2RR, recently proposed as a cascade process to enhance

the Faradaic efficiency in the synthesis of C_2 and C_3 products for industrial processes [78]. In the proposed frame, CO may be produced by both one-step CO_2RR and reverse water-gas shift (RWGS) reaction [79]:

$$nCO_2 + nH_2 \rightleftharpoons nCO + nH_2O. \tag{2-4}$$

While part of CO may eventually complex with the metal surface, we suppose that the other part may be transported by the permanent bubbles, together with the other gases present in the PLA environment, the injected CO_2 and the H_2 and O_2 produced during WS. As reported in Figure 2.8(c), CO may be further reduced to alcohols and hydrocarbons by Fischer-Tropsch (FT) process of CO present in the permanent bubbles[79, 80]:

$$nCO + (2n + 1)H_2 \rightleftharpoons C_nH_{2n+2} + nH_2O, \tag{2-5}$$

$$nCO + (2n)H_2 \rightleftharpoons C_nH_{2n} + nH_2O. \tag{2-6}$$

Together with the previous chemical paths, secondary products of FT process may be methane, alcohols, and solid carbon, the last generated from tranformation of two molecules of CO in one molecule of CO_2 and a carbon atom [81]. It is interesting to note that, in the frame of PLA, other possible paths may lead to the formation of solid carbon material. In fact, as last step in CO_2/C process, we suppose the further reduction of the FT products to C_n building units, which may condensate in solid carbon forms, both around the metal nanoreactors or as isolated carbon nanostructures. The latter proposal, is based on the results of literature reporting the formation of both sp or sp^2 carbon nanostructures by PLA of metal targets in ethanol, methanol [82], toluene [83], hexane [84], or by direct ablation of small hydrocarbons such as acetylene (C_2H_2), ethylene (C_2H_4) or benzene (C_6H_6) [85], representing the C_n building units shown in Figure 2.9(c).

In this panorama, it is reasonable to suggest that intermediate volatile liquid products such as alcohols or hydrocarbons are readily transformed to solid carbon material and that not only volatile oxygen containing species (R-COOH, oxidation products) might form a covalent link with the metal core of the nanoparticle. Nevertheless, we don't exclude oxidation reactions of the intermediate products, and we highlight that the proposed scheme takes in account only the possible path of the reduction reactions, representing a simplified vision of the working principle of the PLA-CO_2/C process.

2.7 Amorphous and graphitic carbon

Considering our proposal about the PLA-CO_2/C reduction reactions happening in the PLA for the reasoning made before, it becomes interesting to focus now on a general review about carbon atoms, hybridization of carbon atoms, and the principal forms of solid carbon.

Carbon is an element present in Group IV of the periodic table and it's one of the elements that can be encountered in different hybridization states, due to their distinctive bonding configurations [5, 10, 86]. In the case of carbon, two electrons of the s-orbital may overlap (hybridize) with two electrons of the p-orbitals to form four valence electrons for bonding with other atoms [10, 86]. The kind of hybridization is classified as sp, sp^2 or sp^3, and can be used to explain the chemical reactivity and the geometry of the molecules [5]. sp^3-hybridization refers to an overlap between one s-orbital and three p-orbitals, where the four electrons are positioned in a tetrahedral form; sp^2-hybridization deals with the overlap of a s-orbital and two p-orbitals, in which three electrons form a trigonal plane and the last is perpendicular to it; as for the sp-hybridization, there is overlap of one s-orbital and one p-orbital, resulting in two unhybridized orbitals orthogonal to the single hybridized orbital [10, 86].

Figure 2.10 emphasize some of the many examples of hybridization states occurring in the carbon molecules. Here in, we note that the particular presence of σ and/or π bonds is linked to the different hybridization states [5, 10, 86]. In general, σ bonds are stronger than π bonds and the last one can only occur in non hybridized orbitals [5, 86]. Both can also be used to classify single, double and triple bonds as well: a single bond is always σ; $\sigma - \pi$ bond pair represents a double bond; and finally, σ,π,π bonds represents a triple bond [86].

Among the allotropes of carbon, graphite is the most common and one of the most stable forms [10, 86]. It consists of layers formed by sp^2 hybridized carbons, where each carbon in the sp^2 site can make bonds with three other atoms, forming a continues honeycomb planar structure [10, 86]. Each carbon layers is weakly bonded to the other by Van der Waals interactions and can be called constitutive "graphene layer" of graphite[10, 86]. Although the planar layers may slide quite easily over each other, the structure of graphite is highly ordered and extremely stable, with an interplanar distance of about 0.33 nm [139].

It is interesting to note that the ordered crystal structure of graphene is a direct consequence of the pure sp^2 hybridized bonds, and that inclusions of sp^3 bonds in the structure, progressively leads to lose the crystalline structure.

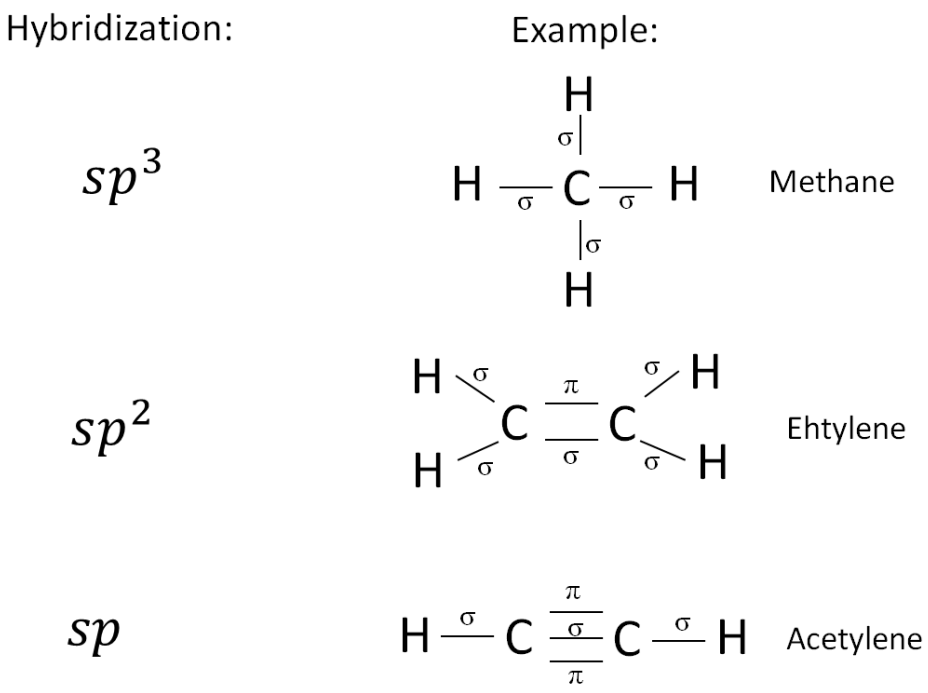

Figure 2.10: Representation of carbon structures and their hybridization states. Adapted from [5].

In this case, the carbon material is generally defined as amorphous and its properties depends on the ratio between the sp^3 and sp^2 hybridized bonds [87, 86, 88]. In this frame, since some sp^2 domains are always present also in amorphous carbon, there is the possibility for the solid to have a short-range crystalline order [87, 86, 88] and a considerable quantity of the sp^3 domains, in which case the material is called "amorphous graphitic carbon" [10, 9, 89].

One of the most used technique to produce solid carbon with different degrees of graphitization is by pyrolisis [10, 9]. In pyrolisis, graphitic materials are generally produced by heating at high temperatures ($\sim$ 3000 K) a polymer or other carbon rich specie. Examples are the highly oriented pyrolitic graphite (HOPG), a synthetic crystalline graphite with high purity and order [10], and graphitic amorphous nanomaterial synthesized in [9] through catalytic graphitization of polymers in contact with Ni and Fe powders.

We finish this brief description of carbon based material, defining as organic matter, matter containing a carbon with oxidation number below 4, other than carboxylic acids, carbon monoxide or carbon dioxide.

2.8 Linking astrochemistry and PLA

From what was discussed in the last sections, it is now possible to understand how astrochemistry is related to our research. Astrochemistry itself deals with the study and understanding of the chemical and physical evolution of the Universe, from simple molecules (such as H_2O, CO, CO_2 and CH_4) to complex ones (carbonaceous materials, silicates and organic compounds), and eventually to those molecules that could be precursors of biological species (such as proteins, amino acids, fats, and sugars). Based on this concept, it is possible to assess the relationships between the experiments on laser ablation of metals immersed in water and phenomena that may occur in space.

Carbon materials in different chemical forms are found on the surface of several minor bodies of the Solar System and in cosmic dust grains in the interstellar medium [21, 90, 91, 92]. In the outer Solar System and in dense clouds of the interstellar medium the surface temperature can be as low as 10 K. This implies that carbonaceous materials in these regions may be covered by the so-called astrophysical ice. The composition of such ices is a matter of great interest within the astrophysical community and is the focus of researches involving laboratory measurements of the IR absorption properties of species of astrochemical interest, as well as observational and theoretical studies of the physical and chemical properties of such astrophysical regions. We present in Table 2.1 the main species found within interstellar medium ices, alongside the relative concentrations, taking the abundance of water ice as 100% [138].

Molecule	CO_2	CO	NH_3	CH_3OH	CH_4	H_2CO
Abundance	10-25	0-40	5-10	3-30	0.3-4	3-7

Table 2.1: Molecules present in astrophysical ices and their abundance relative to water ice [138].

How these species are formed and evolve on these types of bodies is a question still under debate. Among other hypotheses, some researchers first thought that the interactions between small rocky fragments within the solar nebula as well as those between cosmic dust grains in the interstellar medium could be related to the production of these compounds in the process called Fischer-Tropsch(FT) [24, 25], which was previously used to explain a part of the CO_2 reduction processes in section 2.6.

In astrochemistry, this process would determine that metals such as Fe and Ni, the minerals present in the surface of some minor bodies and cosmic dust grains, would serve as catalysts for CO, CO_2 and H_2 in these astrophys-

ical environments to be converted in other types of carbon structures on the surface of these metals [25]. This is not the first time the Fischer-Tropsch (FT) mechanism has been proposed as an interesting solution possibly explaining some of the physical and chemical processes happening in space. Nevertheless, looking in the literature, experimental results used to understand the composition of the Murchision meteorite(a carbonaceous chondrite meteorite) showed that n-alkanes, which are considered products from FT reactions, were probably produced due to contamination on Earth [90, 93]. Because of this, Cronin and Pizzarello concluded that the FT processes could not be considered as primary mechanisms for the formation of organic materials in space [93]. Also for this reason, researchers now think that the FT mechanism is of greater importance mainly for the production of the primary component of the reaction, i.e., metane(CH_4) [24, 25, 94]. This chemical reaction is shown below:

$$CO_2 + 4H_2 \rightleftharpoons CH_4 + 2H_2O. \tag{2-7}$$

Considering what was proposed in section 2.6, our idea agrees with this opinion and also implies that FT is only a part of the mechanism associated to the synthesis of organic material, both in space and in PLA environment.

An important issue we want to highlight is the conceptual frame sustaining the application of LASiS for the laboratory simulation of chemical reactions induced by space weathering. The last term relates to the processes induced on the surface of minor bodies or cosmic dust grains in space, such as their bombardment by micrometeorites, cosmic dust, ions or radiation. In our research, the interest is in the interactions between micrometeorites with the surface of minor bodies(for what concerns processes happening in the Solar System) and with cosmic dust grains (for what concerns processes happening in the interstellar medium). Both situations show similarities with the processes taking place during the PLA experiments. Both the interactions may generate a plasma plume in a water environment, with subsequent synthesis of nanoparticles, as sketched in Figure 2.11. Noteworthy, it was also observed that the interaction between laser pulses and the surface of various minerals, induce morphological effects similar to those induced by the natural micrometeorites bombardment [19]. From the energetic point of view, micrometeorites with 10^{-9}-10^{-8} kg produce energies equivalent to 3-6 mJ [19, 95], which is a similar energy to the ones used in our study with a ns-pulsed laser.

Considering the materials, we selected Fe and Ni metals to simulate the metallic component present on the surface of some minor bodies of the Solar System, as well as in cosmic dust grains in the interstellar medium. Analyzing the elemental composition of meteorites, which are the only samples

we have on Earth coming directly from the Solar System, we realize that in the class of metal-rich carbonaceous chondrites meteorites type C2, such as the Renazzo meteorite, the weight percent of Fe and Ni are estimated as 10.7% and 1.4%, respectively[21]. Moreover, also exist a class of iron meteorites, such as the meteorite Javorje, whose bulk chemical composition reaches values of approximately 92% of Fe and 8% of Ni in weight percentage [22]. In the case of the interstellar medium, besides the carbonaceous component, there is the cosmic dust which consists mostly of silicate core and other metals, such as iron [23], as it was already introduced in section 2.1.

It is finally worth to remember that the cosmic dust and the surface of asteroids may be surrounded by an ice film, which, beyond the water component, is constituted by simple molecules such as CO, CO_2, CH_4, NH_3, and low concentrations of more complex species, not yet detected in astronomical observations, although predicted by astrophysical experiments and models

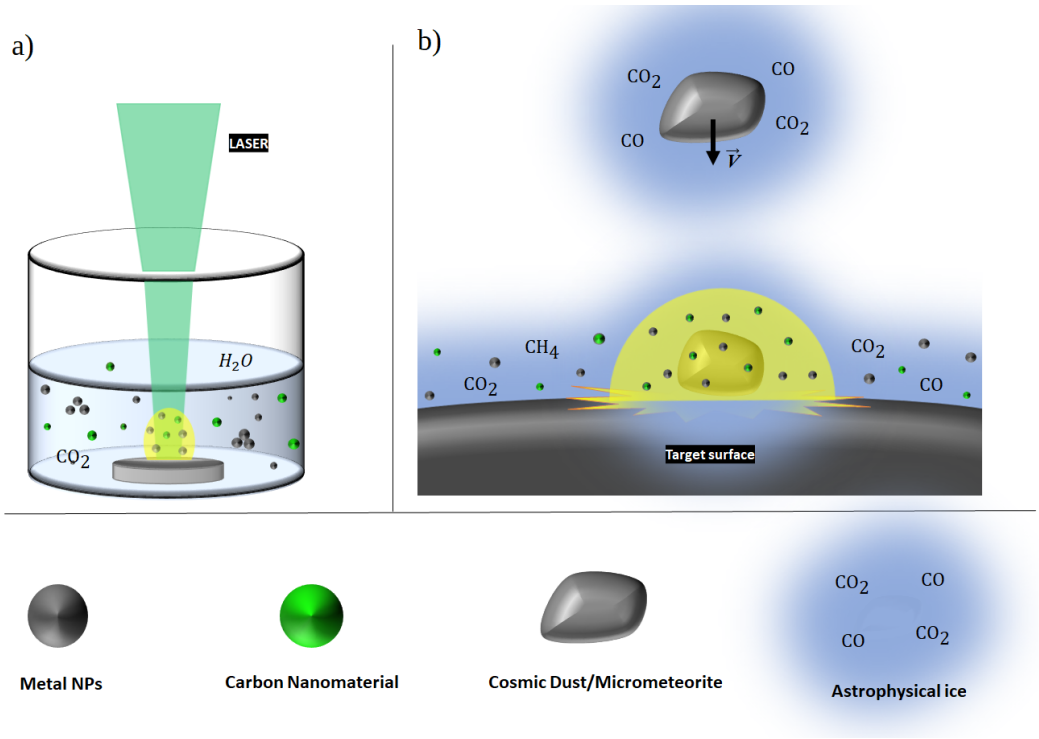

Figure 2.11: Analogies between PLA of Ni and Fe targets in water (a) and space weathering due to the impact between micrometeorite/cosmic dust and an astrophysical target (target surface), which could be either the surface of a minor body of the solar system, or cosmic dust grain (b). The yellow spot represents the plasma plume, and in blue is indicated the astrophysical ice. $\vec{V}$ represents the relative velocity of the species subject to space weathering, and in grey and green are represented the metal-oxide NPs and the nanostructured organic material created after the impact of the objects, simulated by the impact between the laser pulse and the metal target.

[96, 97, 98, 99, 100]. The representation of cosmic dust covered with astrophysical ices can be schematically seen in Figure 2.11(b).

In this scenario, we propose that the Fe and Ni oxide nanoparticles are produced by space weathering, and induce both one-step CO_2RR and two-step CO_2RR reactions, with the final production of organic nanomaterial.

3
Experimental methods

3.1
Introduction

In this chapter, it will be described the characteristics and parameters of the experimental techniques used for the characterization of metal-oxide nanoparticles and the identification of organic material, together with the LASiS experimental setup used for the synthesis.

A small section related to photoluminescence spectroscopy has been put in the supplementary material section.

3.2
Instrumentation

In the following, a list of the used equipments and the corresponding experimental method:

- Q-smart 850 laser source (Quantel, U.S.A.): LASiS
- Spectrophotometer model Lambda 950(Perkin Elmer, U.S.A.): UV-Vis spectroscopy
- Inductively coupled plasma mass spectrometrer(Perkin Elmer, U.S.A.): ICP-MS
- Transmission electron microscope(FEI-TITAN and FEI Tecnai-Spirit): transmission electron microscopy(TEM) and energy-dispersive X-Ray spectroscopy(EDS)
- Transmission electron microscope(JEOL Ltd., Japan) with Gatan Enfinium SE/976 EELS spectrometer and a Centurio Large Area EDS detector(JEOL Ltd., Japan): electron energy-loss spectroscopy(EELS)
- Micro Raman spectrometer model LabRam HR-800(Horiba Jobin Yvon): Raman spectroscopy
- Spectrophotometer Spectra-Two model(Perkin Elmer, U.S.A.): Fourier-transform infrared spectroscopy (FTIR)

– Fluorimeter(Photon Technology International): photoluminescence spectroscopy(more information can be found in the chapter of "Supplementary material")

3.3 Cleaning of glasses and metal targets

During the synthesis of NPs by PLA, it is necessary to be alert to the risk of contamination. Therefore, a rigorous method of cleaning was essential for us to have coherent results. In this sense, the glassware used for PLA synthesis and stocking of dispersive colloidal NPs, as well as the metal targets of PLA should be subject to a rigorous cleaning protocol.

Laboratory glassware

a)The glassware was firstly washed with distilled water; b) The glassware was kept in a recipient with nitric acid diluted in distilled water(10% diluted) for 24 h; c) The glassware was removed from the acid and then, they were rinsed with a great quantity of distilled water; d) The glassware was put in the oven at 60^o C for 30 min; e) Trichloroethylene was put inside the glasses and they were put in an ultrasonic bath for 10 minutes. Afterward, the glasses were washed with distilled water; f) The procedure of the last item was repeated for acetone, ethanol, distilled water and ultra-pure water; g) Finally, the glasses were left in the oven at 60^o C so they could be dried and ready for use in the laser ablation experiment.

Metal targets

As for the metal disks of Ni (99.995 % pure, Kurt J. Lesker Company) and Fe (99.95 % pure, Kurt J. Lesker Company) used as targets: 1) they were immersed in a recipient with trichloroethylene and put in the ultrasonic bath for 10 min; 2) the ultrasonic baths were repeated for acetone, ethanol, distilled water and ultra-pure deionized water; 3) the clean targets were conserved protected in an oven at 40^o C.

3.4 LASiS experimental setup

LASiS was performed using a Q-Smart 850 (Quantel, U.S.A.) laser source (Figure 3.1(a)) available in the *Laboratory of Optical Synthesis and Characterization of Nanomaterials (NanoLaserLab)* of the Department of Physics of PUC-Rio. The laser source is characterized by a pulse duration of 6 ns and a fixed repetition rate of 10 Hz. It can be used with the fundamental frequency ω, equivalent to 1064 nm, or second harmonic 2ω, equivalent to 532 nm. However, in this research, we focused on the second one. Moreover, the ablation time used was 5 h.

The PLA experimental setup is shown in Figure 3.1(b). From the image, it is possible to see that we produced the nanoparticles by double ablation of metals immersed in liquid. As it is expected, our productivity of nanoparticles can increase adapting the system disposal in this way, but also it allows the possibility of doing ablation of two different targets for comparison, or with the different liquid environment.

Firstly, the laser pulse travels from the source to a beam splitter(BS), which separates the laser pulse in equivalent energies (50% each). Subsequently, each laser pulse is reflected by a mirror in the direction of a lens. Finally, the lens converges the laser pulse in the direction of the target that is immersed in a determined volume of water inside a beaker.

The energy of each pulse was measured using a pyroelectric energy sensor (ThorLabs, model ES220C) (Figure 3.1(c)) which works in a wavelength range from $0.185 - 25$ μm and an energy range of 500 μJ-3 J. In our research, we used a total energy between 14-16 mJ, so that each target sample received 7-8 mJ.

The height of the lenses was adjusted in a way so that the target would receive a fluence F of about 6 J/cm^2. The calculus of F of the laser pulse will be shown in the next subsection.

To perform LASiS, we used glass beakers with diameters of 4.2 cm for each PLA synthesis, in which we put 12 mL of ultra-pure water. We finally highlight that LASiS was performed in open air environment, so that the CO_2 concentration at the gas-liquid interface during PLA was about 0.04 % [29].

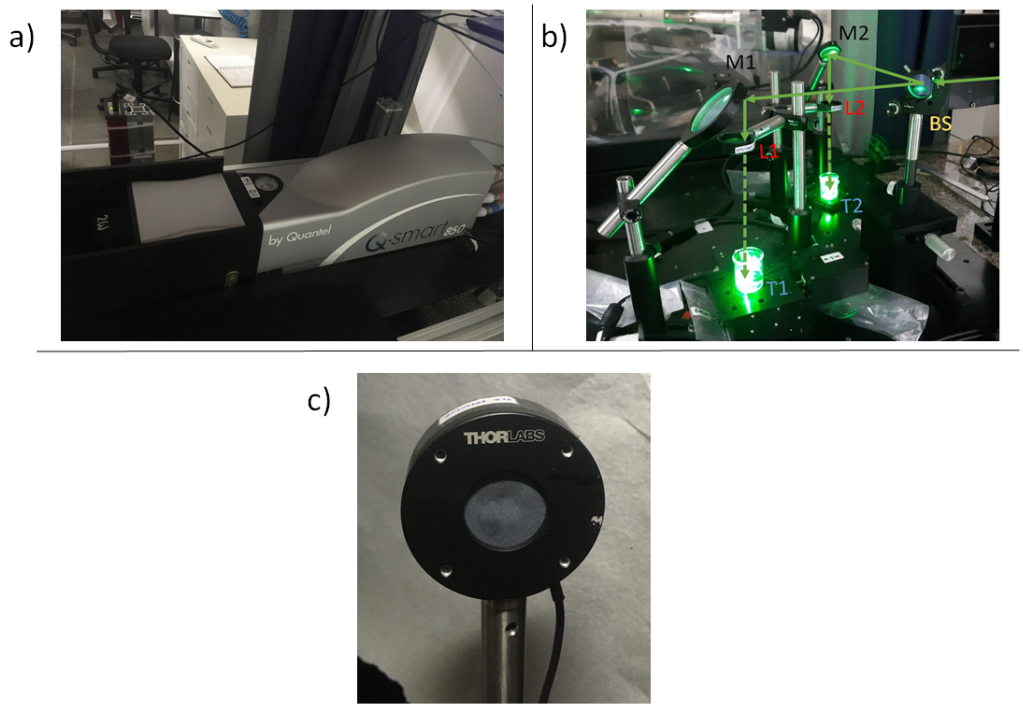

Figure 3.1: (a) Pulsed-laser source Q-smart 850 (Quantel, U.S.A) operated with module for the second harmonic frequency(2ω). (b) PLA experimental setup, in which the laser pulse is coming from the right direction to the left. BS is a beam splitter, M1 and M2 are mirrors, L1 and L2 are lenses and T1 and T2 represent the metal targets immersed in the water. (c) Pyroelectric energy sensor (ThorLabs, model ES220C)

3.4.1
Calculus of the fluence(F) of the Laser Pulse

As described in Section 2.2, the laser fluence F is one of the most important parameters controlling the size distribution and rate production of the nanoparticles synthesized. It is defined as:

$$F = \frac{4E}{\pi {\phi_T}^2}, \tag{3-1}$$

where E is the energy of the laser pulse, and ϕ_T is the diameter of the region of interaction. For the calculation of F we take into account the measured energy of the pulse E, the focal distance of the lens used in the experiment, and the height of the column of water over the target, which has a lensing effect on the propagation of the laser pulse. By using the simple laws of geometrical optics, we make use of the scheme reported in Figure 3.2 for the calculation of F.

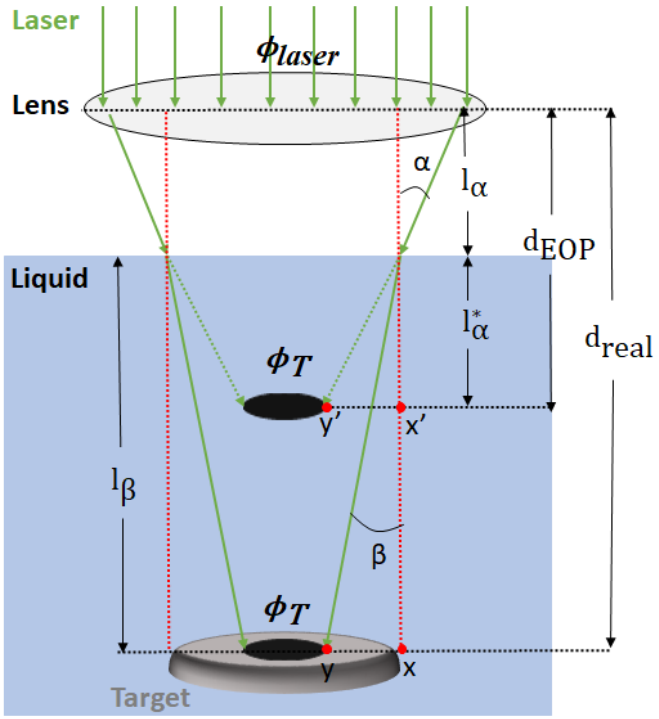

Figure 3.2: Scheme used for the calculation of F using geometrical optics. The laser pulse passes through the convex lens, interacts with the liquid, and finally, reaches the metal target. Adapted from [5].

As it can be seen in Figure 3.2, the laser pulse with a diameter ϕ_{laser} (∼0.7 cm, according to the instrumentation manual) reaches the convex lens and is focused on the target surface after passing through the liquid. At the air-liquid interface, the laser pulse has an angle of incidence α and an angle of refraction β. Considering that we know the value for the focal length f =14.9 cm, we can calculate the angle of incidence α as :

$$\alpha = \tan^{-1}(R_L/f) = \tan^{-1}(0.35/14.9) = 0.0235\ rad. \tag{3-2}$$

With this value, it is possible to calculate the β angle, following the Snell law, considering the index of air, n_{air}=1, and the index of the liquid, n_{liq}=1.3:

$$n_{air} \sin\alpha = n_{liq} \sin\beta, \tag{3-3}$$

$$\sin\beta = (n_{ar}/n_{liq}) \sin\alpha \rightarrow \beta = \sin^{-1}[(\frac{1}{1.3}).\sin(0.0235)] \simeq 0.0177\ rad.$$

We define the diameter of the laser spot on the target immersed in liquid as ϕ_T. **y'** denotes the height in which the image of the laser spot would have the same dimension ϕ_T , considering the propagation of the laser pulse in free air, without the liquid. The position indicated by **y'** , define what we call as **equivalent optical path** in air or d_{EOP}, which is the distance between the point and the center of the lens.

According to Figure 3.2, the distance d_{real} is:

$$d_{real} = l_\alpha + l_\beta, \tag{3-4}$$

where l_α is the distance between the lens and the air/liquid interface and l_β is the height of the liquid.

We observe that the distance between the laser spot in air and the air/liquid interface ($l_\alpha{}^*$) is:

$$l_\alpha{}^* = \frac{tan\beta}{tan\alpha} l_\beta = 0.76 l_\beta. \tag{3-5}$$

Therefore, considering the equations for d_{real} and $l_\alpha{}^*$, we have:

$$d_{EOP} = l_\alpha + l_\alpha{}^* = d_{real} - 0.24 l_\beta. \tag{3-6}$$

To obtain the diameter of the laser pulse on the target, we finally use the equation

$$\phi_T = \phi_{laser} \frac{(d_{EOP} - f)}{f}. \tag{3-7}$$

3.5 Separation methods

As introduced in Chapter 2, the laser ablation synthesis can provide colloidal dispersion of NPs characterized by different sizes and chemical composition [135]. In the attempt to separate magnetic NPs characterized by a different average size and/or different magnetic properties, we applied a magnetization separation procedure, both for Ni and Fe derived NPs .

3.5.1
Separation by magnetization

Firstly, the NP's colloidal dispersion of 12 mL of one of the metal targets was synthesized with the laser parameters described in section 3.4. This pristine colloidal dispersion is defined as a colloidal dispersion of mixed nanoparticles, and denoted as $(NPs)^{mix}$, shown in Figure 3.3(a). Then, we applied for 4 days a 0.3 T magnetic field on the sample, by putting a magnet on the side of the glass containing the $(NPs)^{mix}$, as represented in the Figure 3.4. After 4 days, it could be seen that a part of the nanoparticles was attracted by the magnet and concentrated on its side (Figure 3.3(b)). These NPs are denominated precipitant nanoparticles and indicated as $(NPs)^{pr}$.

The liquid in suspension, separated from the precipitant NPs, interestingly was still characterized by the color of colloidal dispersions, indicating the presence of further NPs, which were not sensitive to the magnet. At this point, the liquid was carefully transferred to another recipient, while the $(NPs)^{pr}$ were still interacting with the magnet. Here, it is important to underline that the removed liquid may consist theoretically of different species, both metal oxide NPs (not attracted by the magnet) and possibly organic nanomaterial.

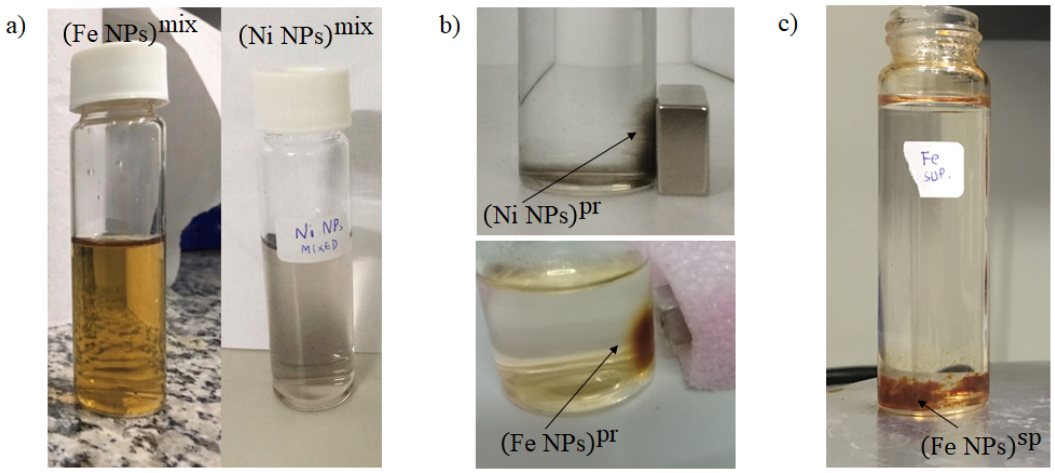

Figure 3.3: (a) Fe NPs and Ni NPs mixed colloidal dispersions. (b) Magnetic separation(both $(Fe\ NPs)^{pr}$ and $(Ni\ NPs)^{pr}$ are marked by an arrow). (c) Supernatant colloidal dispersion of iron NPs after heating for 3 h($(Fe\ NPs)^{sp}$ are marked with an arrow).

In the case of $(NPs)^{pr}$, we redispersed them in ultra-pure water while they were kept interacting with the magnet, using the same quantity that was initially removed. This rinsing process was repeated four times. Afterward, we put the colloidal dispersion in an ultrasound bath for 10 min and, subsequently,

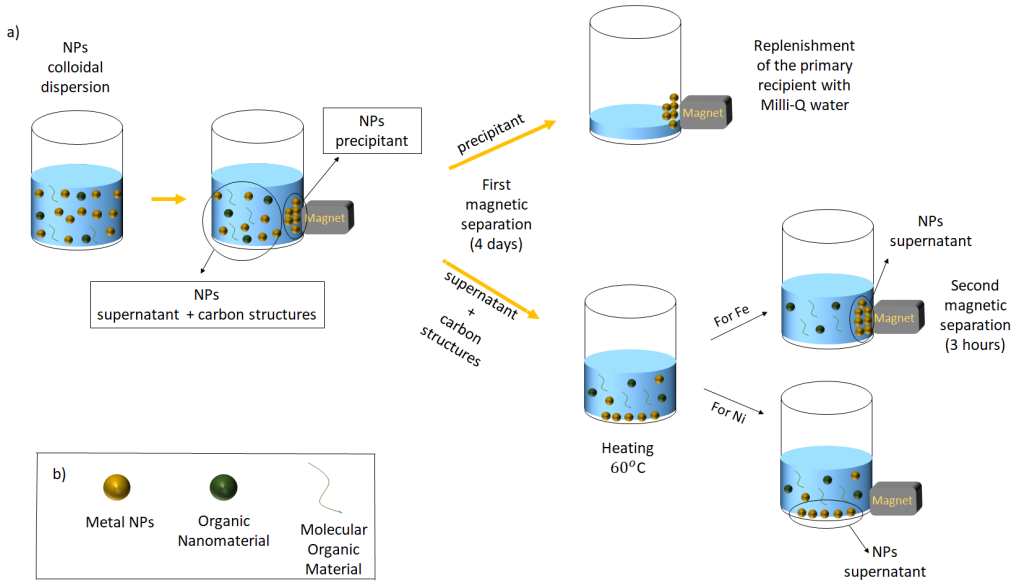

Figure 3.4: (a) Process to separate colloidal dispersions from precipitant and supernatant NPs. (b) Icons with the definition of the structures of the first Figure. Adapted from [5].

we put it again to interact with the magnet for 3 h. Then, we repeated the rinsing only one last time, while the magnet was still attracting the NPs.

Concerning the supernatant colloidal dispersion, we noticed that after about 3 h of thermal treatment in oven at 60^o C, the NPs precipitated at the bottom of the glass container (Figure 3.3(c) and 3.4). One explanation for this could be related to the heating of the liquid generating convection currents, consequently, making the nanoparticles agglomerate and precipitate, or instability due to oxidation reactions. Nevertheless, this action makes the liquid transparent, since the majority of the nanoparticles are expected to be in the bottom. After removing it from the oven, we put the recipient to interact with the magnet again for 2 h. We noticed that the NPs were attracted by the magnet only in the case of iron nanoparticles, while the nickel supernatant (after heating) was not attracted by the magnet. Then, we carefully removed the transparent liquid, eventually containing organic nanomaterial and define the remaining nanoparticles as the supernatant (NPs)^{sp}.

3.5.1.0 Lyophilization

Lyophilization or freeze drying consists of the removal of liquid and formation of powder by sublimation. For this, the liquid, which needs to be frozen, is kept first in the freeze dryer equipment with vacuum which support this transition of states, making it faster. Then, the pressure of the equipment

is lowered and there is transference of heat to the sample so it promotes its sublimation. Finally, the nanoparticles that were in the liquid are the final products and can be removed from the equipment in powder form.

In our research, the liquid samples prepared after the separation by magnetization without water rinsing were frozen in a regular freezer. After, they were put in a freeze dryer FreeZone(Labconco, U.S.A.) from Van der Graaf Laboratory and maintained in vacuum for 4 days. The initial pressure in the equipment was of 0.644 mbar and, in the final day, 0.260 mbar. The temperature of the collector where the frozen samples were kept was -53^o C. At the end of the process, it was produced NPs samples in powder forms. This procedure was made for the Ni NPs samples measured in Raman spectroscopy.

3.6 UV-Vis spectroscopy

UV-Vis spectroscopy was used to measure the extinction spectra of the colloidal solution of nanoparticles produced by PLA in water. This technique is particularly important, since its intensity is linked to the concentration of the metal, and its variation during time can give important informations about the stability of the colloidal system.

Figure 3.5: Spectrophotometer from Perkin–Elmer (USA, model Lambda 950) in the *Optical Spectroscopy Multiuser Laboratory* of the Department of Physics of PUC-Rio.

In Figure 3.5 is represented the spectrophotometer produced by Perkin–Elmer (U.S.A.) in the *Optical Spectroscopy Multiuser Laboratory* of the Department of Physics of PUC-Rio. The spectrophotometer is equipped with deuterium and tungsten halogen lamps and allows to the span of the

wavelength in a range between 175 nm and 3300 nm. In our research, the extinction spectra were measured in a range between 200 nm and 800 nm. To eliminate the contribution of the absorption of water from the final spectrum, it is necessary to perform a blank measurement before the analysis of each sample of colloidal NPs, by the simple acquisition of the absorption spectrum of the ultra-pure water (Milli-Q system).

To prepare the samples for this experiment, we performed only the first magnetic separation described at the beginning of section 3.5.1.

3.7 Inductively coupled mass spectroscopy - ICP-MS

Inductively coupled mass spectroscopy(ICP-MS) was used to identify the differences of metal concentration in each Fe and Ni NPs samples, both in mixed, precipitant and supernatant forms. The samples that were measured in UV-Vis spectroscopy were the same ones used for the measurement of the metal concentration.

The equipment used was a ICP-MS with reaction cells (NexIon 300X and DRC II) from PerkinElmer (USA).

3.8 Fourier-transform infrared spectroscopy(FTIR)

The use of FTIR for the NPs samples may allows to understand both the composition and chemical surface groups on the produced nanomaterial.

Figure 3.6: Spectrophotometer Spectra-Two (Perkin Elmer, U.S.A.) in the *Optical Spectroscopy Multiuser Laboratory* of the Department of Physics of PUC-Rio.

The measurements were performed using the spectrophotometer Spectra-Two (Perkin Elmer, U.S.A.), located in the *Optical Spectroscopy Multiuser Laboratory* of the Department of Physics of PUC-Rio, Figure 3.6. It is char-

acterized by a resolution of 0.5 cm^{-1} in the spectral range of 400-4000 cm^{-1}. It also presents a active diamond surface, useful for the Attenuated Total Reflectance (ATR) modality.

3.8.1 Preparation of the samples for FTIR

With a colloidal dispersion of $(Ni\ NPs)^{mix}$, we made the first separation by magnetization, following the methodology of section 3.5.1. Then, $(Ni\ NPs)^{pr}$ and $(Ni\ NPs)^{sp}$ liquid samples were put in the oven at 43^o C. We wait until all of their liquid had evaporated to form each NPs powder.

It's noted that both $(Ni\ NPs)^{pr}$ and $(Ni\ NPs)^{sp}$ samples separated magnetically were not submitted through a water rinsing process before the heat treatment. So, the transparent liquid, possibly containing organic nanomaterial, would be present in the case of $(Ni\ NPs)^{sp}$.

3.9 Raman spectroscopy

The Raman spectroscopy is a fundamental tool for understanding the chemical nature of the nanoparticles and identifying possible organic products obtained during the synthesis.

Raman spectroscopy was performed in the Department of Informatics of the University of Verona. The Raman spectra were measured by a Micro Raman spectrometer Horiba Jobin Yvon, model LabRam HR-800, equipped with a He-Ne laser(633 nm). The Raman microscope is also equipped with an optical microscope(Olympus, BX41), mounted at a long working distance from the sample with an 80x objective lens, providing a spatial resolution of about 1μm. The scattered light was dispersed using a holographic grating with 600 lines/nm and the maximum radiation flux put in the sample was 10^9 W/m^2.

3.9.1 Preparation of the samples for Raman

After making the first separation method by magnetization described in section 3.5.1 for a pristine colloidal dispersion of Ni NPs, the liquid components of $(Ni\ NPs)^{pr}$ and $(Ni\ NPs)^{sp}$ were frozen and lyophilized, according with section 3.5.1.0. Then, lyophilization of the samples produced NPs powder.

It is important to emphasize that the NPs samples separated magnetically were not submitted through a water rinsing process before the lyophilization, similarly to the case of FTIR. In the same case of FTIR as well, $(Ni\ NPs)^{sp}$ contained the transparent liquid, eventually containing organic material.

3.10 Transmission electron microscopy(TEM), energy-dispersive X-ray spectroscopy(EDS) and electron energy-loss spectroscopy(EELS)

As explained in Chapter 1 of "Introduction", the TEM characterizations were performed by multiple collaborators, such as Prof. Dr. Geronimo Perez and Dr. Braulio Soares Archanjo. TEM images were used to measure the statistical distribution of the sizes of both Fe and Ni NPs, both as precipitant and supernatant.

TEM equipments consist of an illumination system, an objective lens stage, and an imaging system. The illumination system is responsible for the transference of the electrons from the source to the sample by using an electron gun and condenser lenses. As for the objective lens stage, the purpose is to generate the images and the diffraction patterns produced in the interaction between electrons and the sample. Finally, after the productions on the last stage mentioned, the image or the diffraction pattern is magnified and focused by a group of lenses that composes the imaging system. Also, these lenses are responsible for the focus of the image or the diffraction to a viewer screen with the support of CCD or other types of cameras and detectors [132].

In regards to the energy-dispersive X-ray spectroscopy (EDS), it was performed with samples of $(\text{Fe NPs})^{\text{pre}}$, $(\text{Ni NPs})^{\text{pre}}$ and $(\text{Ni NPs})^{\text{sup}}$ in order to detect the carbon element. It is important first to understand that the atom can be seen as composed by the nucleus and a group shells where the electrons can be distributed, following Pauli exclusion principle. In EDS, when an electron beam is targeted on the sample, the electrons in an innershell of the atom present in the sample can be excited and then, ejected from the nucleus. With the holes formed in the inner shell due to this, the electrons of higher shells can jump to this lower states with the emission of X-ray. Finally, this emission of radiation can be measured, which is equivalent to the energy difference of the two shells, consequently, identifying the atom present in the sample.

For the same purpose of EDS, the sample of $(\text{Fe NPs})^{\text{mix}}$, uniquely, was also analyzed by electron-energy loss spectroscopy(EELS). In this spectroscopy, a beam of electrons with defined energies interacts with the sample, after which the electrons are deflected, considering that they experience inelastic collisions. Then, it can be measured the energy loss of those electrons after these collisions, and the value of this energy represents the signature related to chemical bonds of the sample.

The TEM equipment used for the images and the SAED results was a FEI Tecnai-Spirit TEM operated at 120 kV, located in the National Insti-

tute of Metrology, Standardization and Industrial Quality of Rio de Janeiro (INMETRO).

For the EDS experiment, the TEM equipment used was a FEI TITAN operated in the range of 80 kV with a spherical aberration corrector on condenser, equipped with EDS, which is also present in National Institute of Metrology, Standardization and Industrial Quality of Rio de Janeiro (INMETRO).

As for the EELS measurements, they were performed by Prof. Dr. Yutao Xing at Federal Fluminense University (UFF), using a JEM 2100F Field Emission Electron Microscope(JEOL Ltd., Japan) with Gatan Enfinium SE/976 EELS spectrometer and a Centurio Large Area EDS detector(JEOL Ltd., Japan).

3.11 Preparation of the samples for TEM

To produce samples for TEM, EDS and EELS measurements, we used the same method described in section 3.5.1 to obtain each NPs colloidal dispersion component (mixed, precipitant and supernatant), including the water rinsing process. However, we also diluted 15 times all of these liquid samples formed at the end of this procedure. For the dilution, we used 0.1 mL of a colloidal dispersion component of NPs and 1.4 mL of ultra-pure water. Then, the samples were demagnetized with a demagnetizer instrument from Walker LDJ Scientific (U.S.A., model DM-1), because the samples could interfere with TEM equipments that use magnetic lenses. Finally, 20 μL of each sample (mixed, precipitant and supernatant) were put separately in ultrathin carbon film supported by a lacey carbon film on a 300 mesh Au grids (or, briefly, UC-A on holey 300 mesh Au grids). We only used SiO_x grids for the samples of Fe and Ni NPs in EDS with the purpose of detecting carbon structures present in them.

4
Results and discussion

4.1
State of art

In the present chapter, we report the main experimental results obtained during the research, followed by a discussion related to the actual literature. The results are relative to the colloidal dispersion of nanoparticles obtained performing PLA in water on Fe and Ni targets, using the synthesis experimental parameters and separation methods reported in Chapter 3.

We start with the UV-Vis spectroscopy and ICP-MS of the colloidal dispersion of Ni and Fe NPs before (pristine) and after the separation process, highlighting that here and in some other experiments we didn't apply the water rinsing process to the precipitant and supernatant parts. We then show the characterization of the average size of the NPs by TEM and after, we report the chemical characterization by EDS, FTIR, Raman and EELS spectroscopy. We finish the report with the discussion on the impact that the experimental results have in the field of astrochemistry.

We put in evidence that has not been possible to perform some of the cited characterization on both the Ni and Fe derived colloidal dispersion, due to the limited access to the laboratory infrastructure caused by the COVID-19 pandemic. Concerning the ablation of Fe targets, our aim was to complete the investigation performed in the NanoLaserLab reported in [5]. In that work, Raman spectroscopy on the Fe derived nanomaterial, showed the presence of both wustite, magnetite and hematite, together with traces of carbon material (D and G bands). Moreover, in the same work, it was reported the photoluminescence of the transparent supernatant after separation. Part of the present research, was dedicated to reproduce such a photoluminescence (PL) signal. As results, we were not able to observe this emission again, so that our investigation on Fe derived nanomaterial was concentrated on the visualization and detection of the organic carbon nanomaterial by TEM, EDS and EELS.

4.2
UV-Vis spectroscopy and ICP-MS

Since UV-Vis spectroscopy and ICP-MS can be complementary techniques with respect to the concentration of the samples, we place them in the same section.

Firstly, for the analysis of stability, we monitored the UV-Vis spectra of the $(\text{Ni NPs})^{\text{mix}}$ sample along 8 days (192 h). Specifically, in Figure 4.1, are shown the UV-Vis spectra relative to the fresh (as synthesized t = 0h) colloidal dispersion, and the samples aged for 24 h, 72 h, 96 h and 192 h. There is a decrease in the extinction intensity at the wavelength of 300 nm of about 15.6% after 24 h, 49.7% after 72 h, 84.9% after 96 h and 94.5% after 192 h.

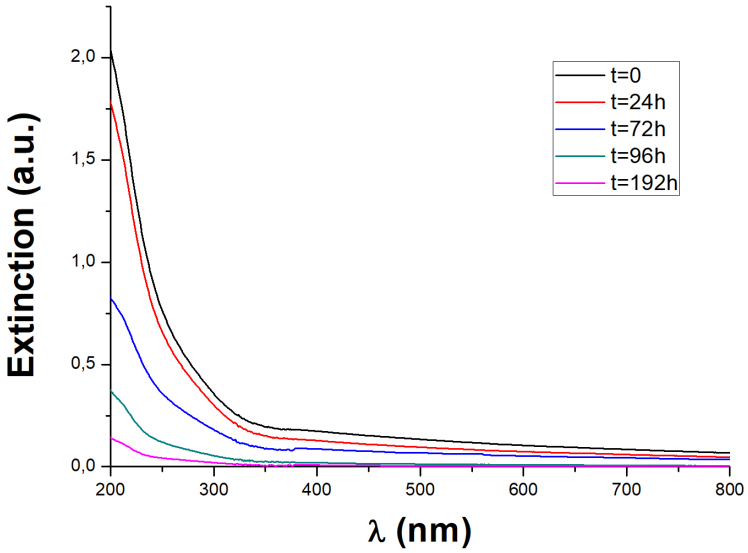

Figure 4.1: Study of the stability of the UV-Vis spectra of the pristine Ni NPs before the separation process $(\text{NiNPs})^{\text{mix}}$. The monitoring was performed along 192 h.

The UV-Vis spectra of both the pristine colloidal dispersion before separation, the $(\text{Ni NPs})^{\text{sp}}$ and the $(\text{Ni NPs})^{\text{pr}}$ are represented in Figure 4.2. From the measurements, we deduce that the $(\text{Ni NPs})^{\text{pr}}$ colloidal dispersion has a higher extinction efficiency than the $(\text{Ni NPs})^{\text{sp}}$.

The results of Ni concentration in each part of the Ni NPs by ICP-MS are presented in Table 4.1.

As for the UV-Vis spectra of $(\text{Fe NPs})^{\text{mix}}$, $(\text{Fe NPs})^{\text{sp}}$ and the $(\text{Fe NPs})^{\text{pr}}$, they are represented in Figure 4.3. Different from the case mentioned before, $(\text{Fe NPs})^{\text{sp}}$ colloidal dispersion has a higher extinction efficiency than the $(\text{Fe NPs})^{\text{pr}}$.

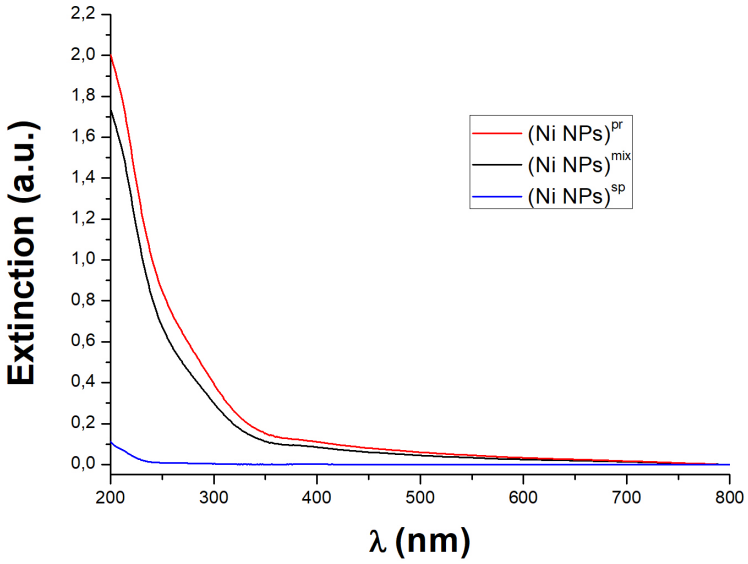

Figure 4.2: Comparison of the UV-Vis spectra of the pristine $(Ni\ NPs)^{mix}$, and $(Ni\ NPs)^{pr}$ and $(Ni\ NPs)^{sp}$ obtained after the separation process(without rinsing with distilled water).

Element Sample	$(Ni\ NPs)^{mix}$	$(Ni\ NPs)^{sp}$	$(Ni\ NPs)^{mix}$	unit
Ni	93 ± 9	21 ± 2	87 ± 9	mg/L

Table 4.1: Concentration(mg/L) of Ni for $(Ni\ NPs)^{mix}$, and $(Ni\ NPs)^{sp}$ and $(Ni\ NPs)^{pr}$ obtained after the separation process. For the errors, we considered the results of three (3) samples.

Finally, the results of concentration of Fe in Fe NPs samples, before and after separation are shown in Table 4.2.

Element Sample	$(Fe\ NPs)^{mix}$	$(Fe\ NPs)^{sp}$	$(Fe\ NPs)^{pr}$	unit
Fe	39 ± 4	37 ± 4	8 ± 1	mg/L

Table 4.2: Concentration(mg/L) of Fe for $(Fe\ NPs)^{mix}$, and $(Fe\ NPs)^{sp}$ and $(Fe\ NPs)^{pr}$ obtained after the separation process. For the errors, we considered the results of three (3) samples.

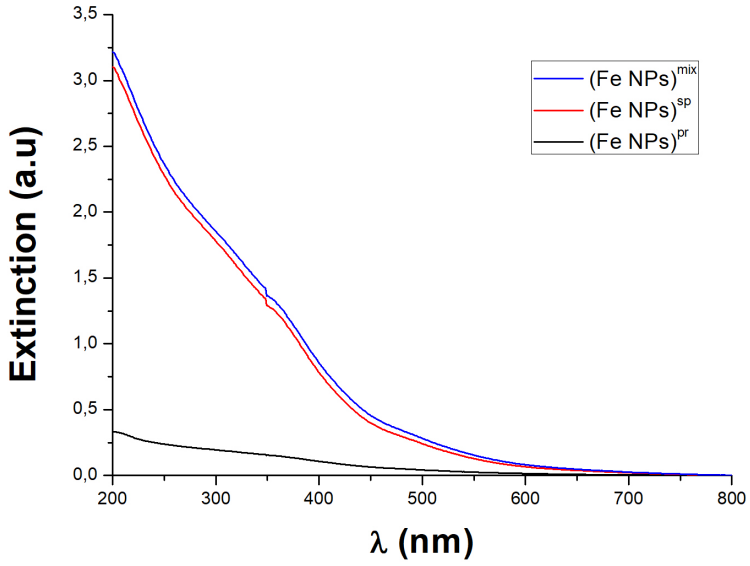

Figure 4.3: Comparison of the UV-Vis spectra of the pristine $(Fe\ NPs)^{mix}$, $(Fe\ NPs)^{pr}$, and $(Fe\ NPs)^{sp}$ obtained after the separation process.

4.2.1
Discussion on UV-Vis spectroscopy and ICP-MS

Coherently with most of the reports about pristine colloidal dispersion of nickel-oxide NPs made by PLA synthesis, a localized surface plasmon resonance (LSPR) band [101] is absent and the extinction presents an absorption band in the UV region.

Considering the stability, at the best of our knowledge, a similar analysis is missing in literature. From our observations, the Ni NPs are mostly agglomerated after 8 days using this methodology, meaning that the majority of NPs are precipitated after this time, probably due to the high reactivity of NiO NPs to redox reactions.

As visible in Figure 4.2 and Table 4.1, the concentration and optical extinction of $(\text{Ni NPs})^{\text{pr}}$ are higher than the $(\text{Ni NPs})^{\text{sp}}$.

Although, considering the errors reported in Table 4.1, the total concentration of the pristine solution matches with the sum of the concentration of the supernatant and precipitant parts, we noticed a peculiar and reproducible anomalous behavior in the UV-Vis spectra. In fact, the intensity extinction of $(\text{Ni NPs})^{\text{pr}}$ is higher than the $(\text{Ni NPs})^{\text{mix}}$. We attribute this anomaly to the fact that ICP-MS analysis were performed 24 hours after the synthesis of the NPs, a time during which the extinction spectra of the pristine solution decreases of about 16% (Figure 4.1). We deduce empirically, that the separation of the NPs in precipitant and supernatant, may enhance the stability of the corresponding colloidal dispersion. But to confirm these hypotheses, a study of stability by UV-Vis spectroscopy of $(\text{Ni NPs})^{\text{pr}}$ and $(\text{Ni NPs})^{\text{sp}}$ should be performed in the future, alongside Zeta-Potential measurements of each Ni NPs component.

As for the iron-oxide NPs, the slope between 200 and 400 nm agrees also with what was presented in previous studies of this products generated in PLA synthesis [5, 67, 68]. Differently from the case of Ni, the $(\text{Fe NPs})^{\text{sp}}$ is more concentrated than the $(\text{Fe Nps})^{\text{pr}}$.

4.3
Morphological Characterization by TEM

This section will focus on the study of the statistical size distribution of the colloidal dispersion of NPs obtained by PLA of both Fe and Ni targets in water, both before and after the separation process with water rinsing. The TEM measurements were performed using different magnification, so that the subsections are divided on the basis of both the nature of the ablated material and the magnification used during the microscopy investigation. A common approach used for the analysis is the fit of the average size distribution by the use of a monomodal log-normal function [102]. The latter can be expressed as:

$$n(\varphi) = \frac{1}{w\varphi\sqrt{2\pi}} e^{\frac{-[ln(\varphi)-ln(\varphi_c)]^2}{2w^2}}. \quad (4\text{-}1)$$

Herein, the parameters w and φ_c are related with the nanoparticle average diameter quantity $< \varphi >$ and standard deviation σ by the relations $< \varphi >= e^{M+\frac{w^2}{2}}$ and $\sigma = (e^{w^2+2M}(e^{w^2}-1))^{\frac{1}{2}}$, in which $M = ln(\varphi_c)$.[102]

In order to measure the distribution of the linear dimension of the NPs, an average spherical shape was assumed. In this case, using the software ImageJ, we did a zoom on the TEM images, and drawed a circle or ellipses representing the contour of each NP. After this, the diameter φ of the NPs was obtained using the equation $A = \pi\varphi^2/4$, where A was calculated by the software. This procedure is sketched in Figure 4.4. In this way, we obtained the histogram representing the statistical size distributions of the Fe and Ni NPs, which were modeled using equation (4-1).

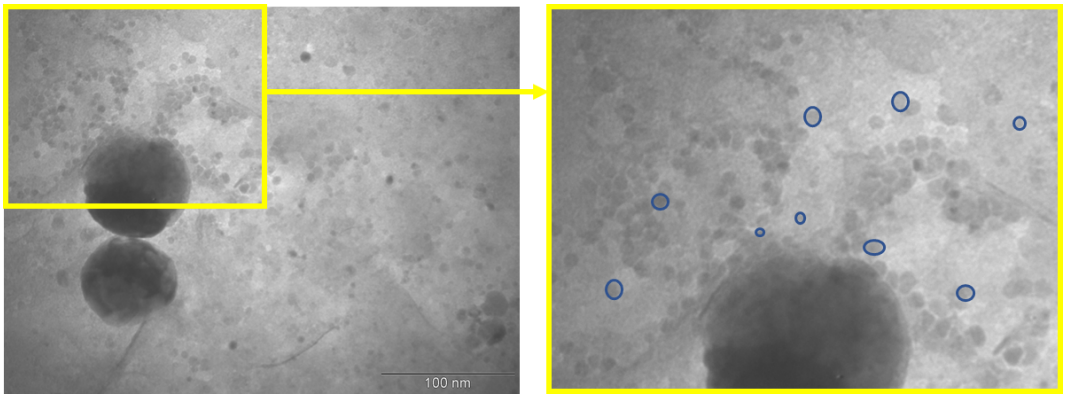

Figure 4.4: Sketch of the procedure used to measure the linear dimension of the NPs by the software ImageJ: (a) TEM image of $(Ni\ NPs)^{mix}$ sample. (b) Zoom of the region of interest in TEM image of the $(Ni\ NPs)^{mix}$ sample, where the blue circles represent the contour of the NPs used to retrieve their diameter, using the approximation of a spherical shape.

We highlight that both in the case of Fe and Ni targets, we observed a

few nanoparticles with average diameter sizes higher than 20 nm. Since their number is so small that does not influence the results obtained during the fit of the statistical size distribution, they weren't counted in the corresponding histograms.

After the report of the TEM images used to measure the statistical size distribution of the NPs, the last part of this section is dedicated to the observation of nanostructures different from spherical metal nanoparticles.

4.3.1
Fe based nanoparticles

Lower magnification (Scale bar:$\geq$ 100 nm)

The TEM images of the NPs and their respective statistical size distribution with a scale bar of 100 nm or more, are shown in Figures 4.5, 4.6 and 4.7, associated to $(\text{Fe NPs})^{\text{pr}}$, $(\text{Fe NPs})^{\text{sp}}$ and $(\text{Fe NPs})^{\text{mix}}$, respectively. The $(\text{Fe NPs})^{\text{pr}}$ ($< \varphi > \approx 6.0$ nm) presents bigger dimension than the $(\text{Fe NPs})^{\text{sp}}$ ($< \varphi > \approx 4.2$ nm). The results are coherent with the images relative to the $(\text{Fe NPs})^{\text{mix}}$, for which we determined $< \varphi > \approx 4.9$ nm.

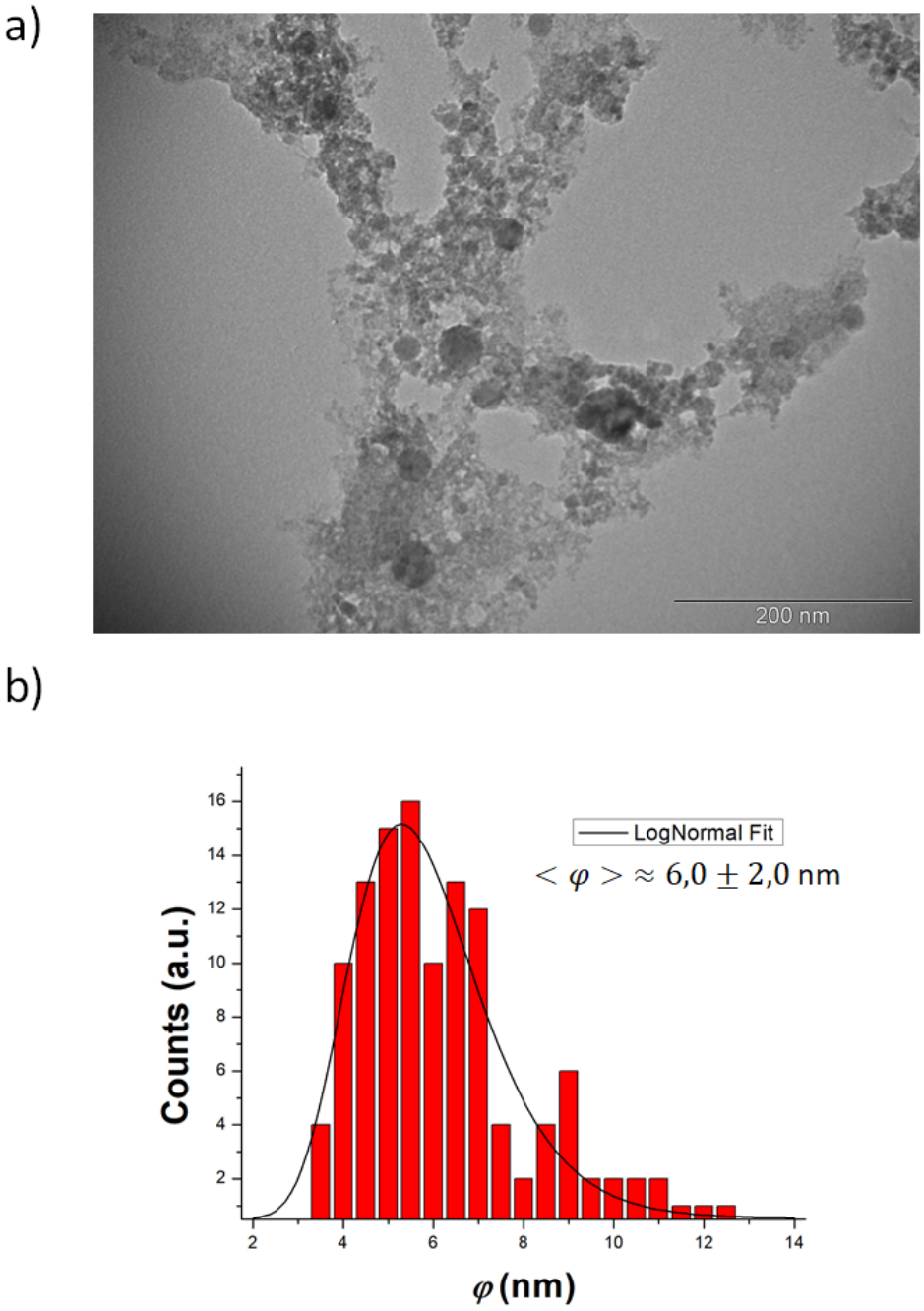

Figure 4.5: (a) TEM image (scale bar of 200 nm) with the histogram (b) of the nanoparticle size of (Fe NPs)^{pr}.

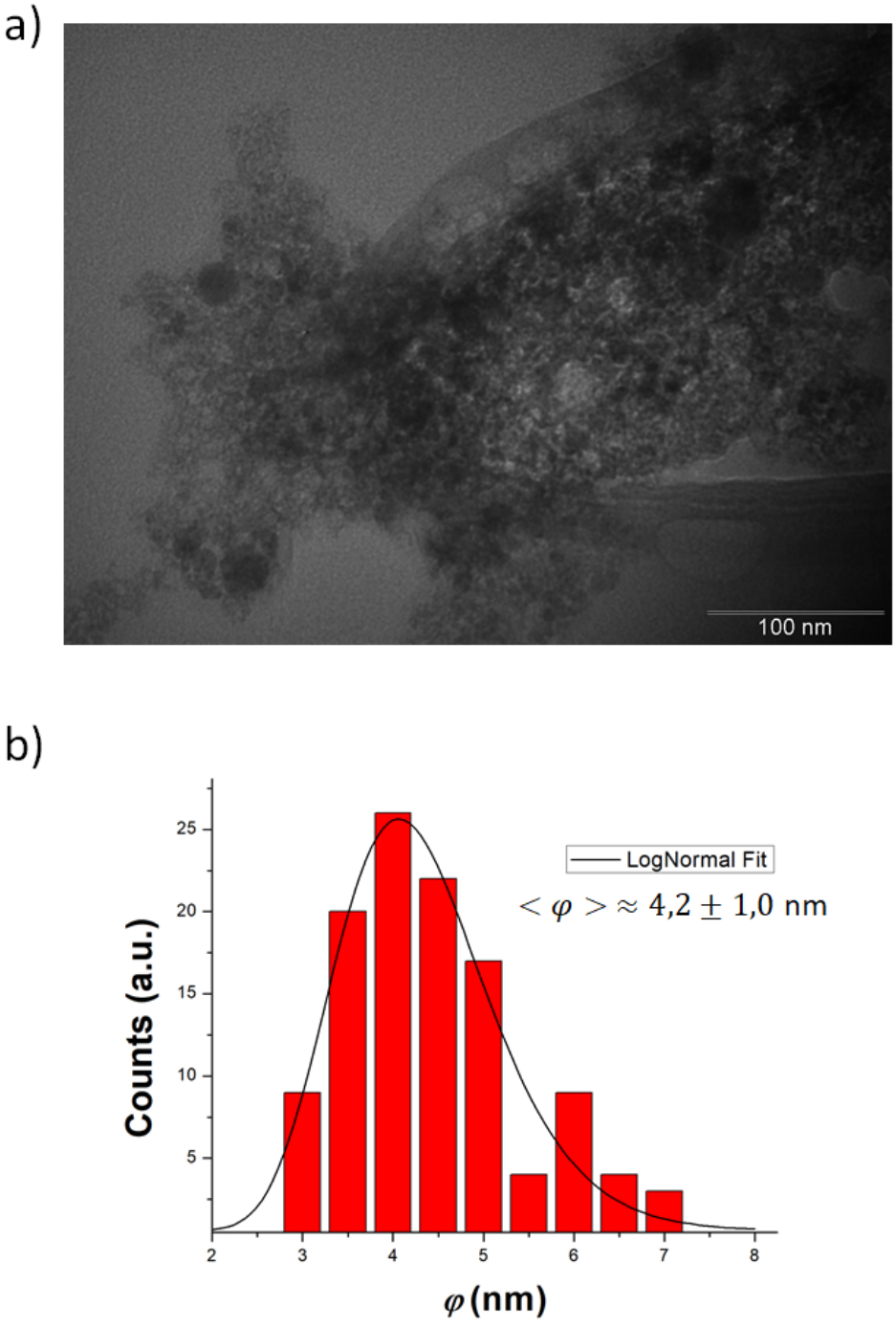

Figure 4.6: (a) TEM image (scale bar of 100 nm) with the histogram (b) of the nanoparticle size of (Fe NPs)^{sp}.

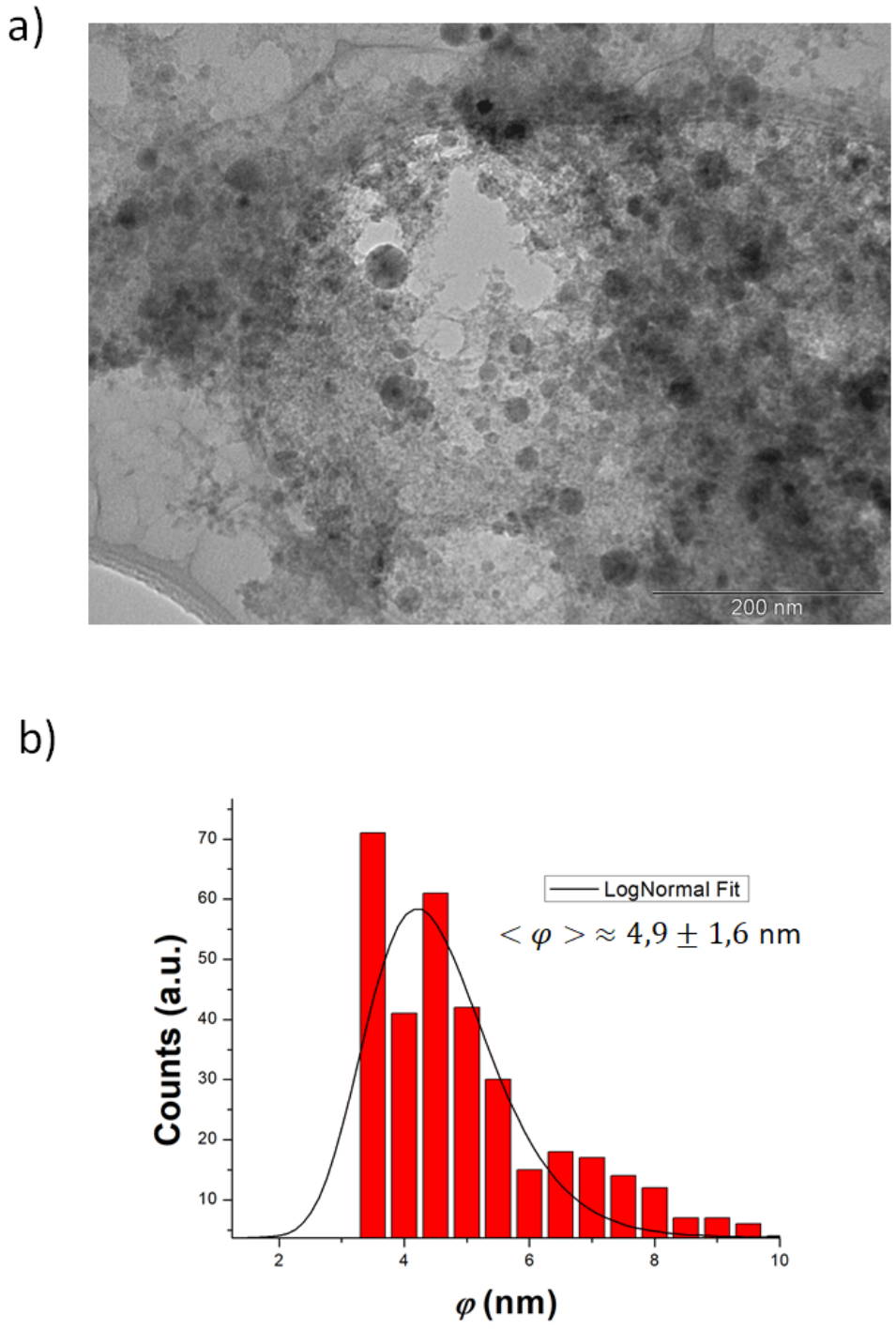

Figure 4.7: (a) TEM image (scale bar of 200 nm) with the histogram (b) of the nanoparticle size of $(\text{Fe NPs})^{\text{mix}}$.

Higher magnification (Scale bar: 50 nm)

Considering the images obtained using a higher magnification (scale bar of 50 nm), they are presented before each corresponding statistical size distribution in Figures 4.11, 4.18 and 4.19, for $(\text{Fe NPs})^{\text{pr}}$, $(\text{Fe NPs})^{\text{sp}}$ and $(\text{Fe NPs})^{\text{mix}}$, respectively. A combination of the results of various images were used in this case to build a unique histogram used for the final log-normal fit.

It's clear that nanoparticles with diameter sizes below 3 nm became more noticeable due to the higher magnification. Yet, the results are coherent with what it was shown at lower magnification: bigger nanoparticles are present in the precipitant ($< \varphi > \approx 2.9$ nm) when compared with the supernatant ($< \varphi > \approx 2.2$ nm). In the latter case, we observe a considerable fraction of NPs having a diameter below 2 nm. The statistical size distribution of $(\text{Fe NPs})^{\text{mix}}$ ($< \varphi > \approx 2.5$ nm) is coherent with the results obtained after the separation process.

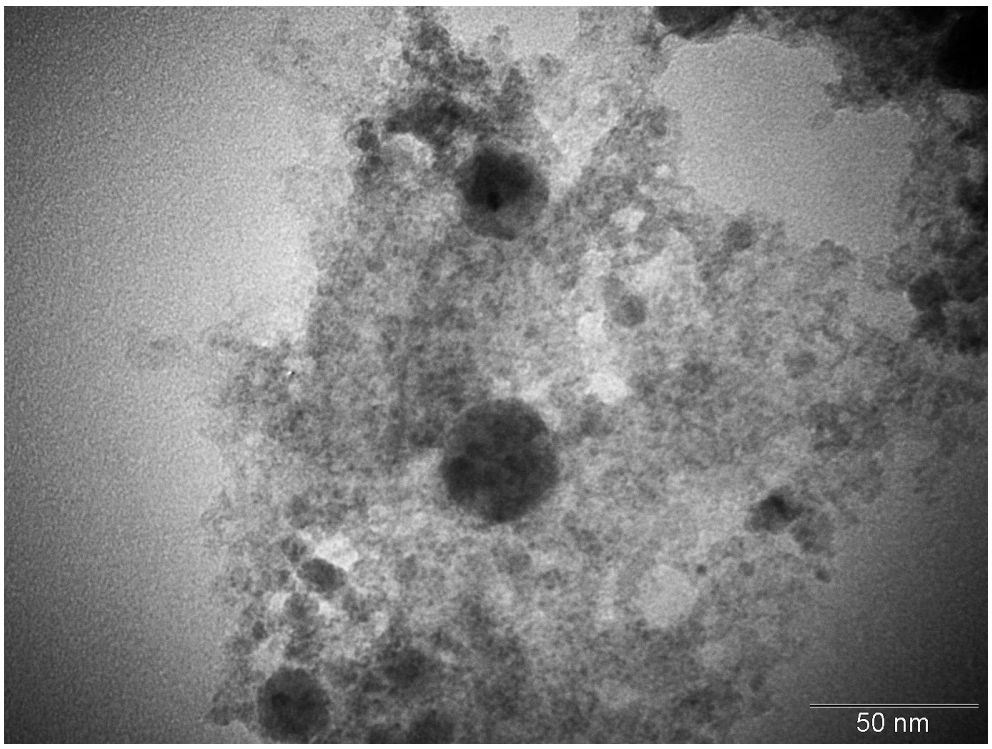

Figure 4.8: TEM image (scale bar of 50 nm) of region 1 of $(\text{Fe NPs})^{\text{pr}}$.

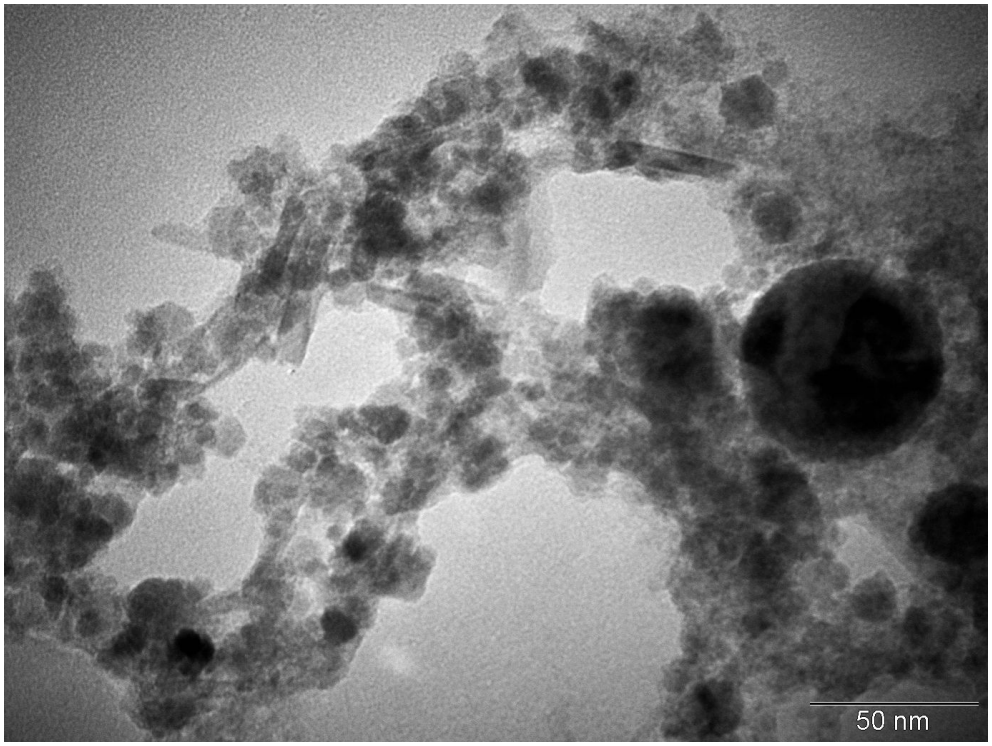

Figure 4.9: TEM image (scale bar of 50 nm) of region 2 of (Fe NPs)^{pr}.

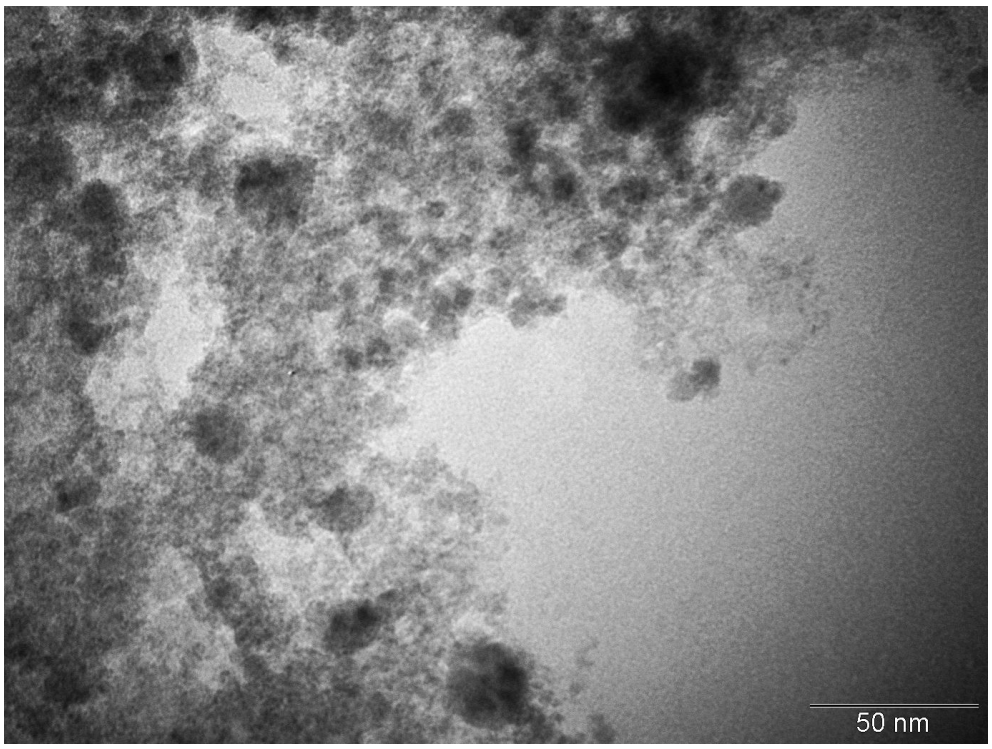

Figure 4.10: TEM image (scale bar of 50 nm) of region 3 of (Fe NPs)^{pr}.

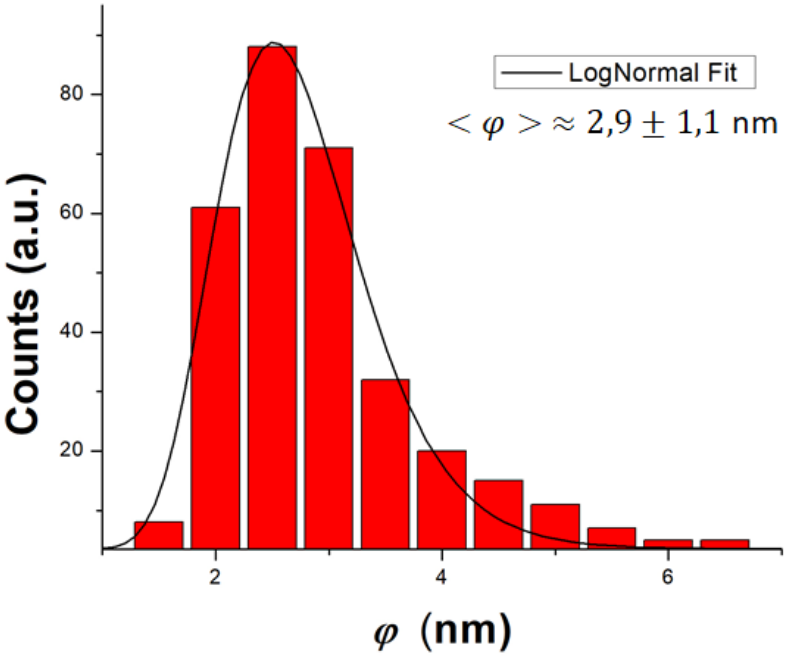

Figure 4.11: Histogram of the nanoparticle size of (Fe NPs)^{pr}, associated to the analysis of regions 1, 2 and 3 of the same component.

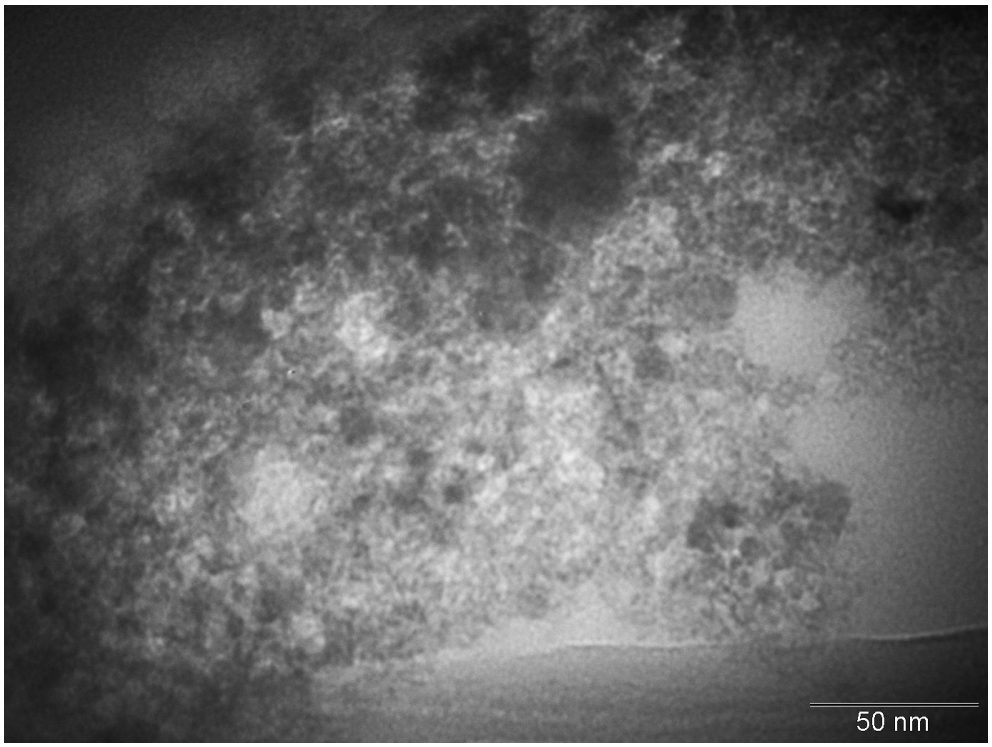

Figure 4.12: TEM image (scale bar of 50 nm) of region 1 of (Fe NPs)^{sp}.

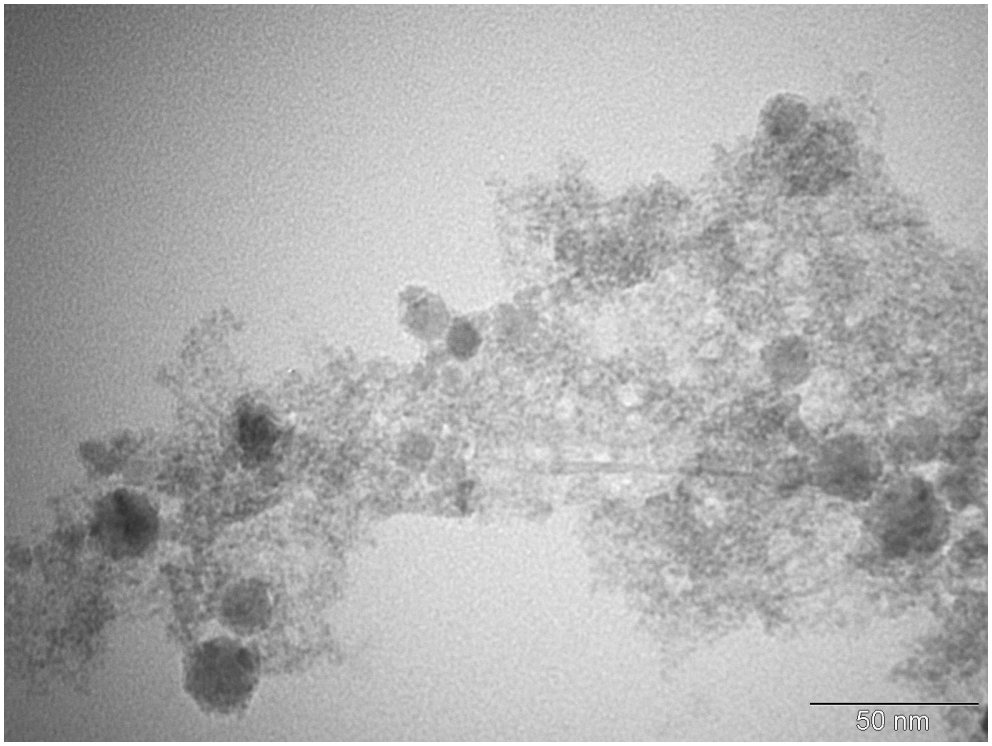

Figure 4.13: TEM image (scale bar of 50 nm) of region 2 of (Fe NPs)^{sp}.

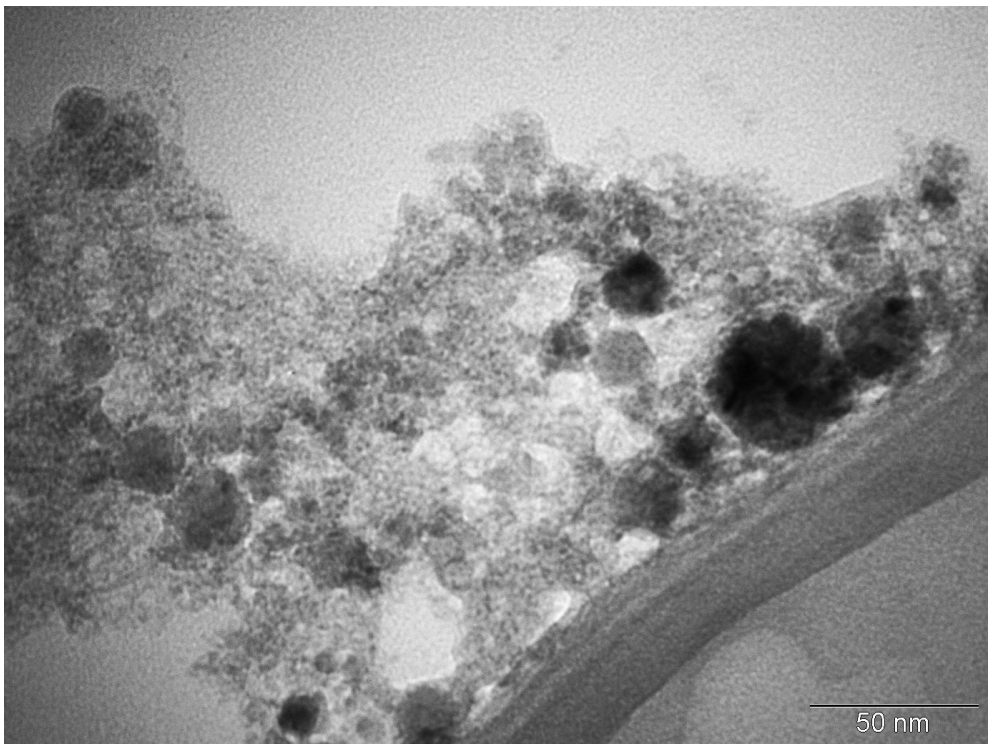

Figure 4.14: TEM image (scale bar of 50 nm) of region 3 of (Fe NPs)^{sp}.

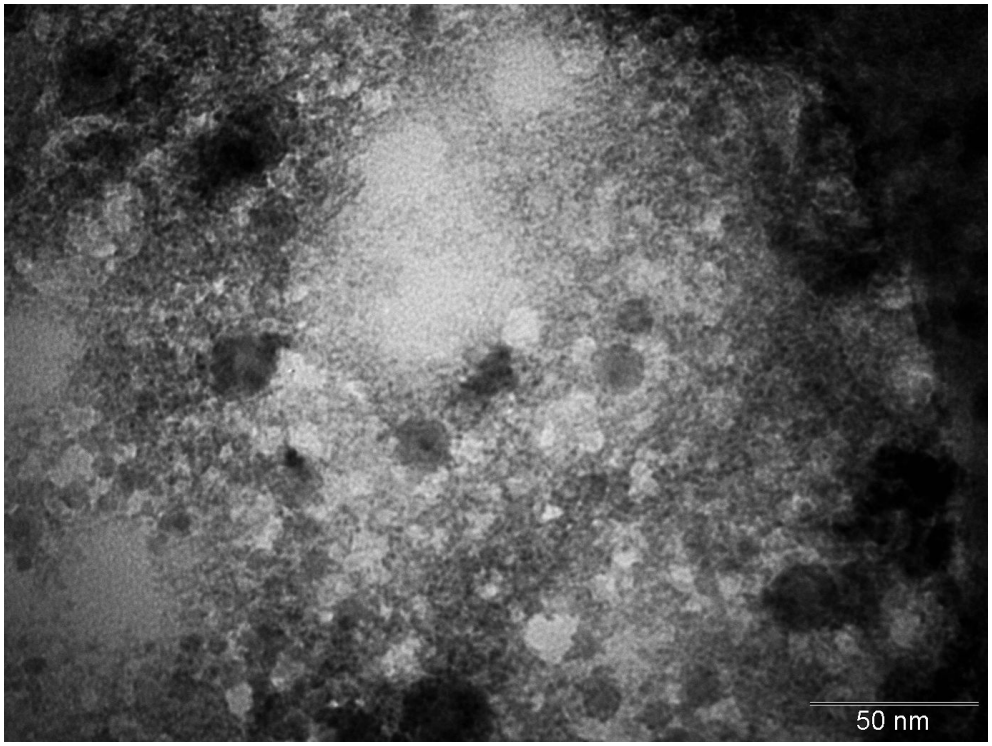

Figure 4.15: TEM image(scale bar of 50 nm) of region 4 of (Fe NPs)^{sp}.

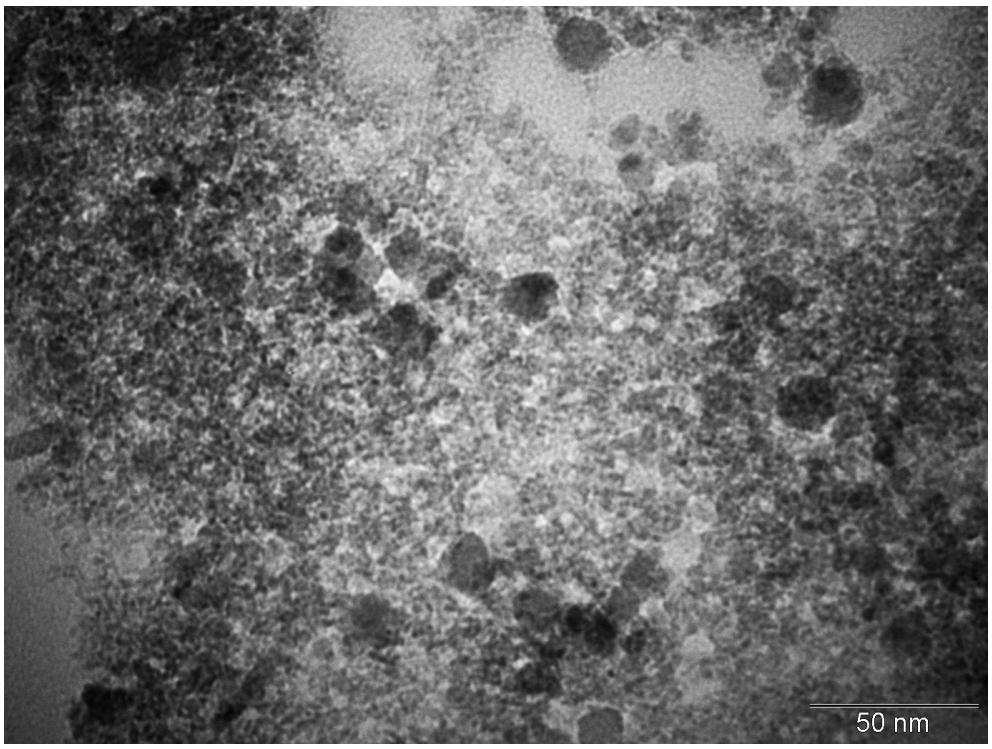

Figure 4.16: TEM image (scale bar of 50 nm) of region 5 of (Fe NPs)^{sp}.

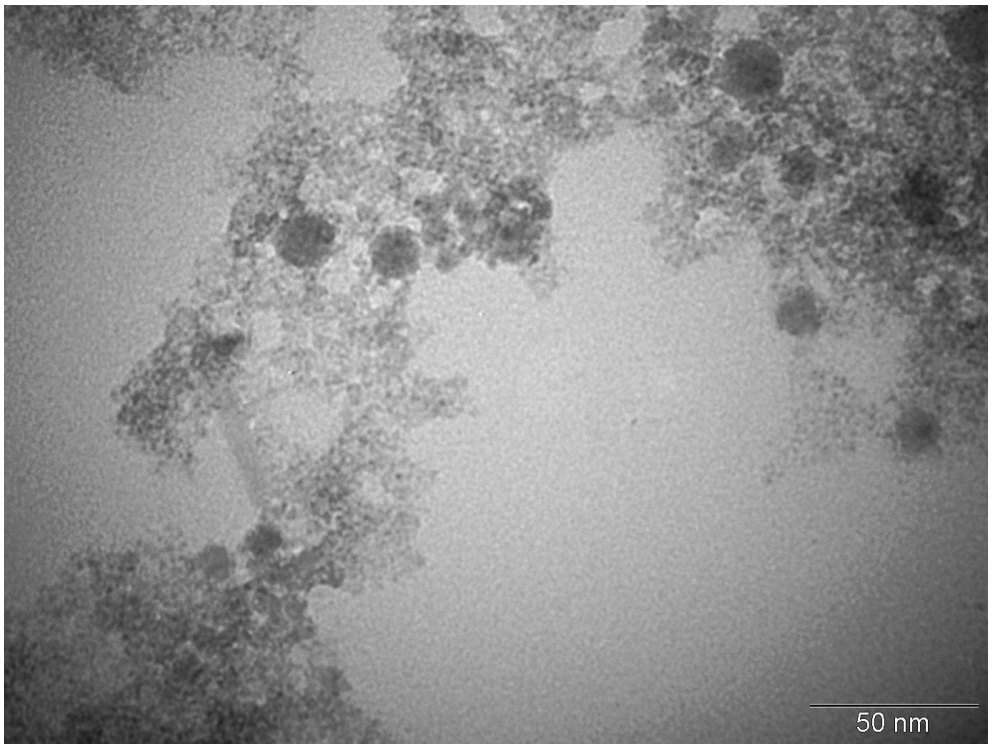

Figure 4.17: TEM image (scale bar of 50 nm) of region 6 of (Fe NPs)^{sp}.

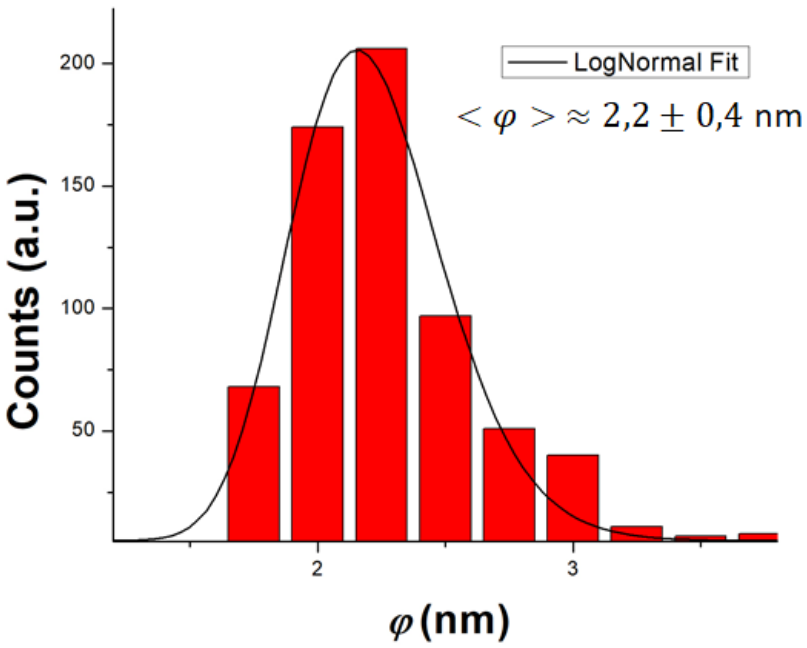

Figure 4.18: Histogram of the nanoparticle size of (Fe NPs)^{sp}, associated to the analysis of regions 1, 2, 3, 4, 5 and 6 of the same component.

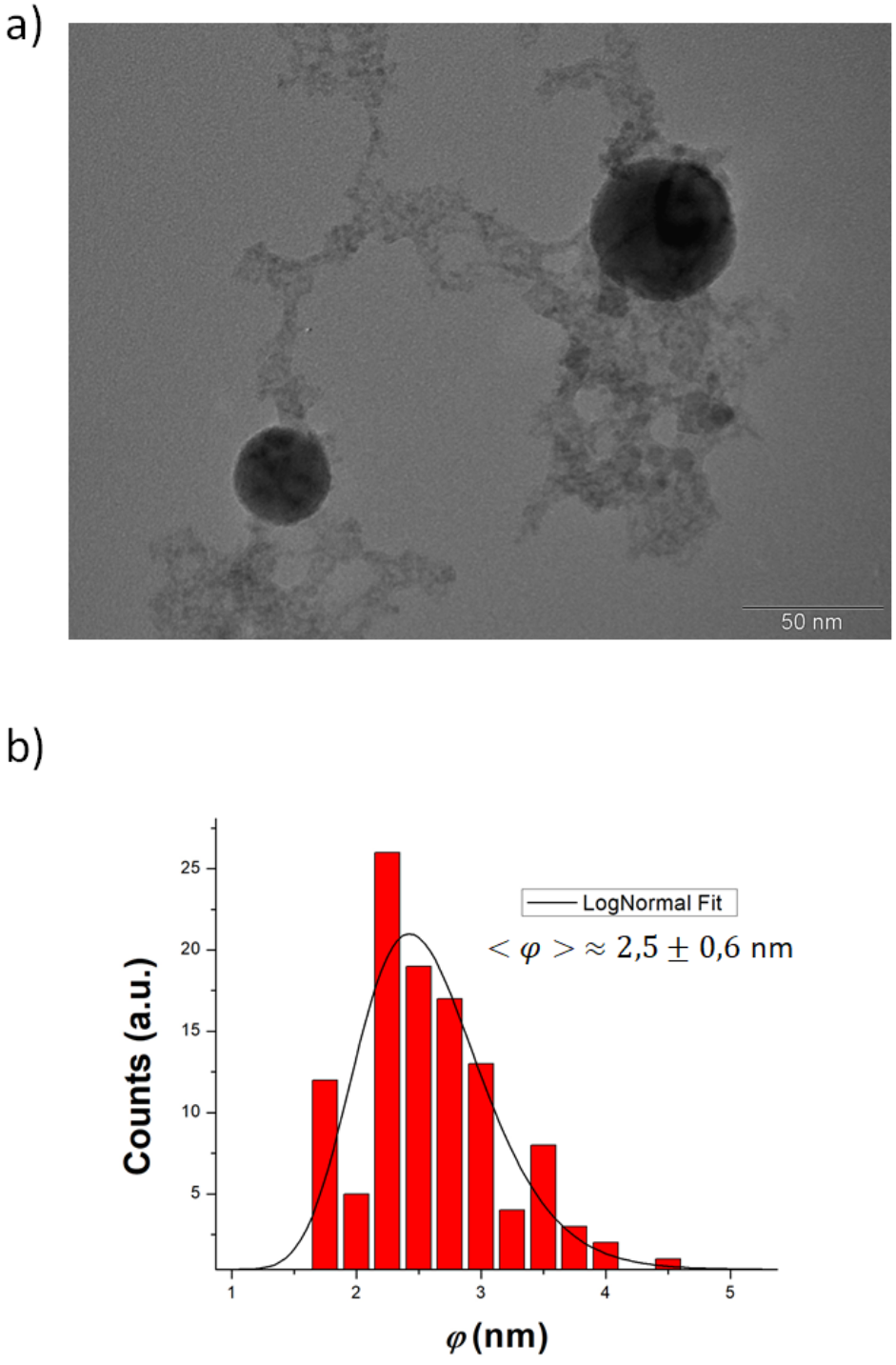

Figure 4.19: (a)TEM image (scale bar of 50 nm) with the histogram (b) of the nanoparticle size of $(\text{Fe NPs})^{\text{mix}}$.

4.3.2
Ni based nanoparticles

Lower magnification (Scale bar: 100 nm)

The TEM images of the Ni NPs with their histograms are presented in Figures 4.20, 4.21 and 4.22. They are associated to $(\text{Ni NPs})^{\text{pr}}$, $(\text{Ni NPs})^{\text{sp}}$ and $(\text{Ni NPs})^{\text{mix}}$, respectively.

In the case of lower magnification(scale bar of 100 nm), $(\text{Ni NPs})^{\text{pr}}$ ($< \varphi > \approx 3.8$ nm) seem to have higher average diameter than the $(\text{Ni NPs})^{\text{sp}}$ ($< \varphi > \approx 3.6$ nm), although the difference is very small.

However, the nanoparticles with diameter of the order of 2 nm are not well visible at low magnification.

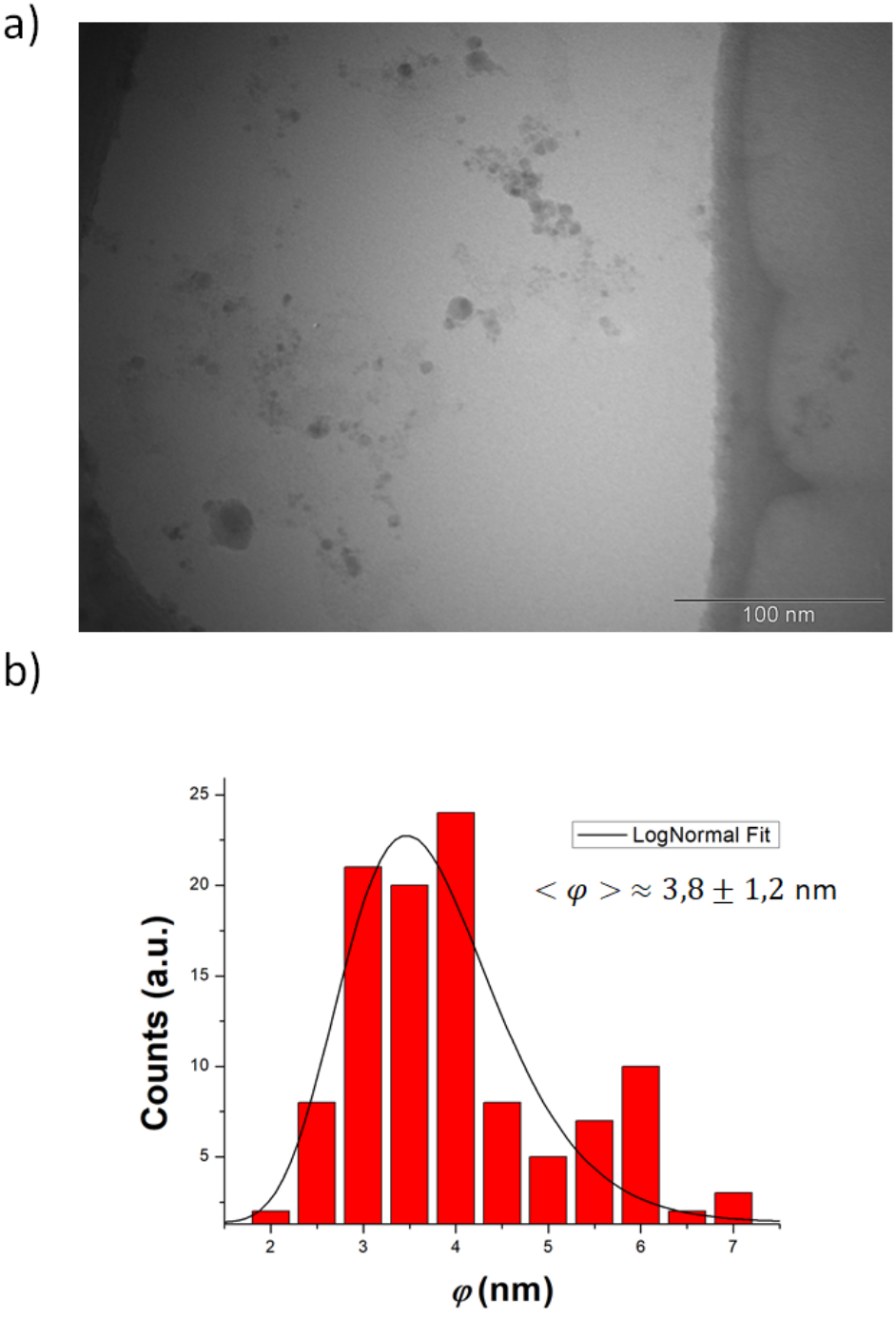

Figure 4.20: (a)TEM image (scale bar of 100 nm) with the histogram(b) of the nanoparticle size of (Ni NPs)^{pr}.

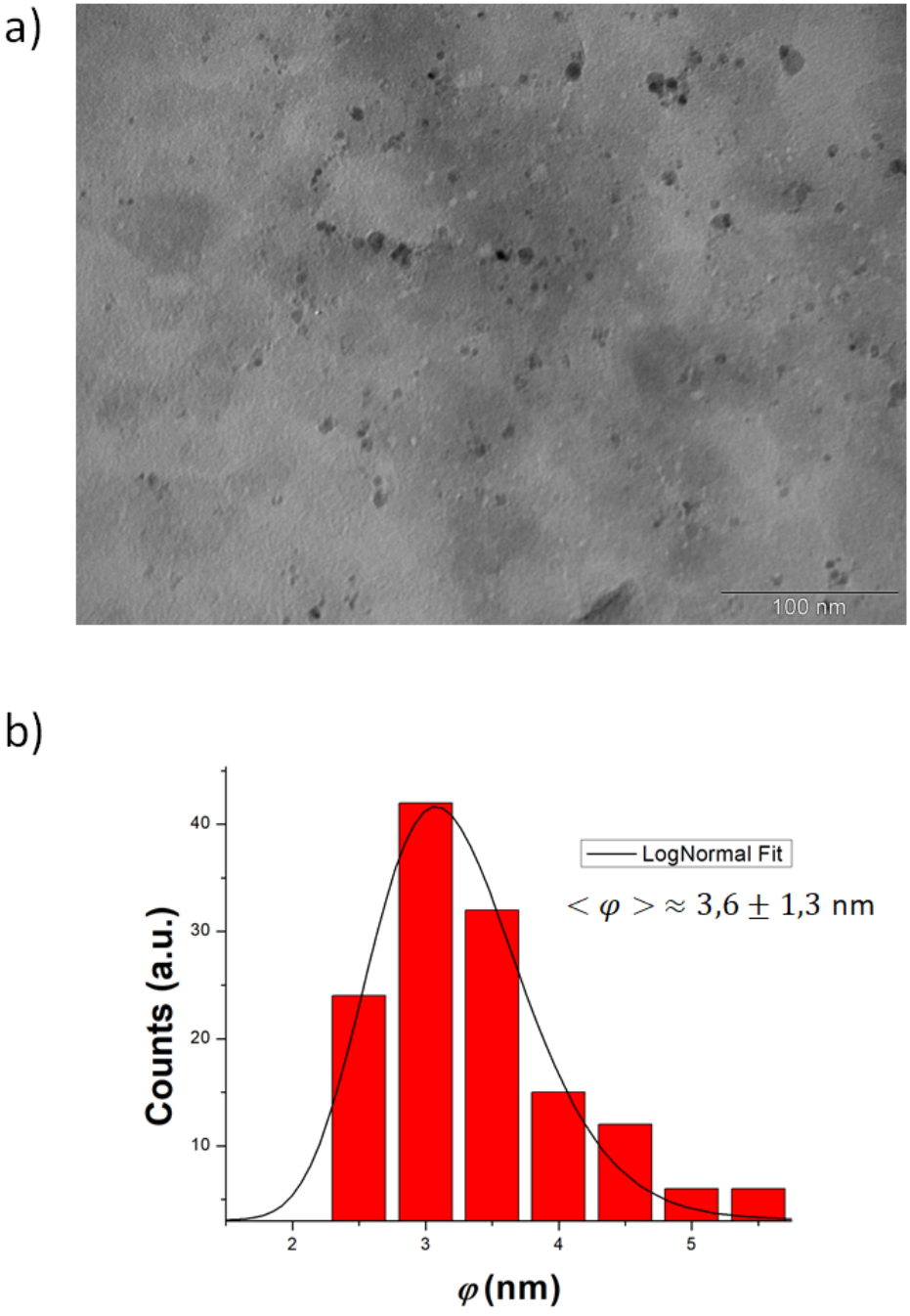

Figure 4.21: (a)TEM image (scale bar of 100 nm) with the histogram (b) of the nanoparticle size of (Ni NPs)^{sp}.

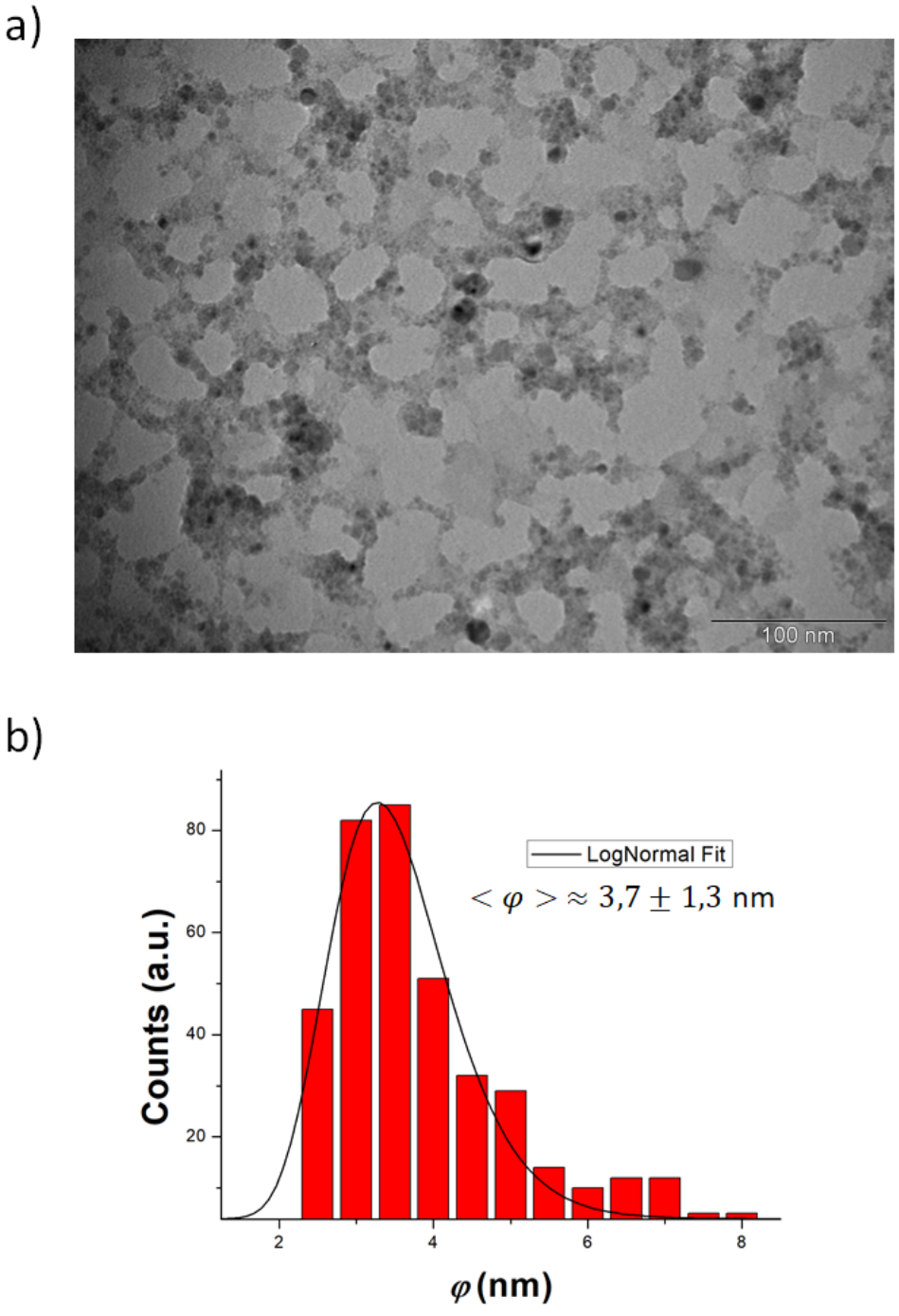

Figure 4.22: (a)TEM image (scale bar of 100 nm) with the histogram (b) of the nanoparticle size of $(\text{Ni NPs})^{\text{mix}}$.

Higher magnification (Scale bar: 50 nm)

Following the same order of components shown in the last section, the TEM images at higher magnification (scale bar of 50 nm) are presented before their respective histogram. The histograms of $(\text{Ni NPs})^{\text{pr}}$, $(\text{Ni NPs})^{\text{sp}}$ and $(\text{Ni NPs})^{\text{mix}}$ are represented in Figures 4.26, 4.32 and 4.33, respectively.

It can be observed, that the average diameter for $(\text{Ni NPs})^{\text{pr}}$ and $(\text{Ni NPs})^{\text{sp}}$ is very similar ($< \varphi > \approx 3.1$ nm). The average diameter of the $(\text{Ni NPs})^{\text{mix}}$ is also in the same range ($< \varphi > \approx 3.2$ nm).

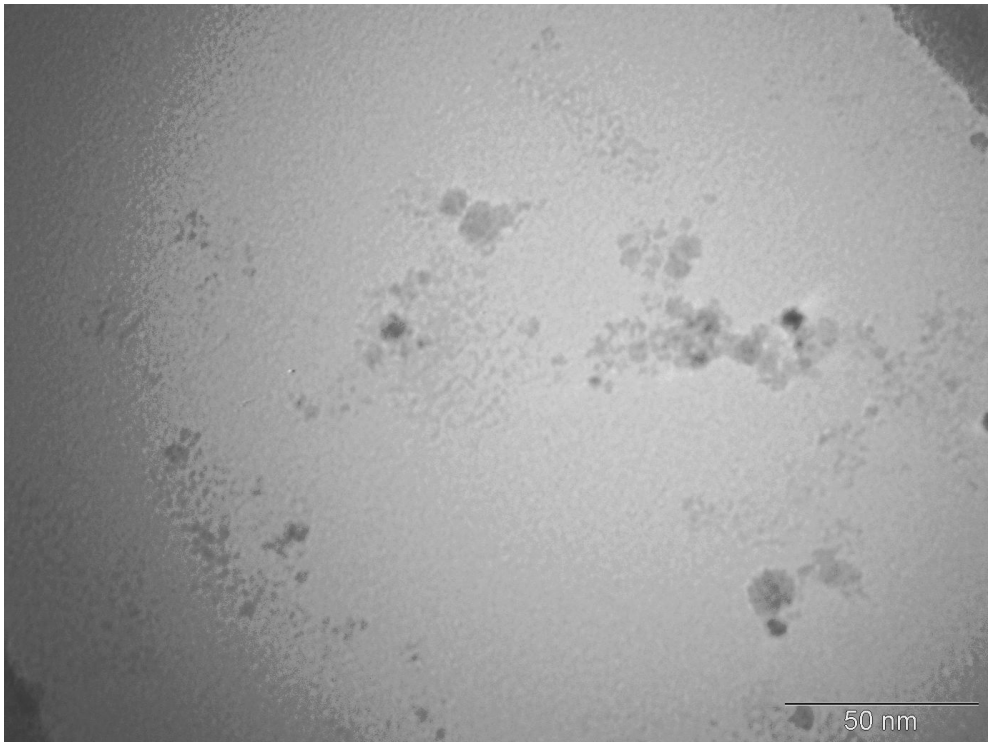

Figure 4.23: TEM image (scale bar of 50 nm) of region 1 of $(\text{Ni NPs})^{\text{pr}}$.

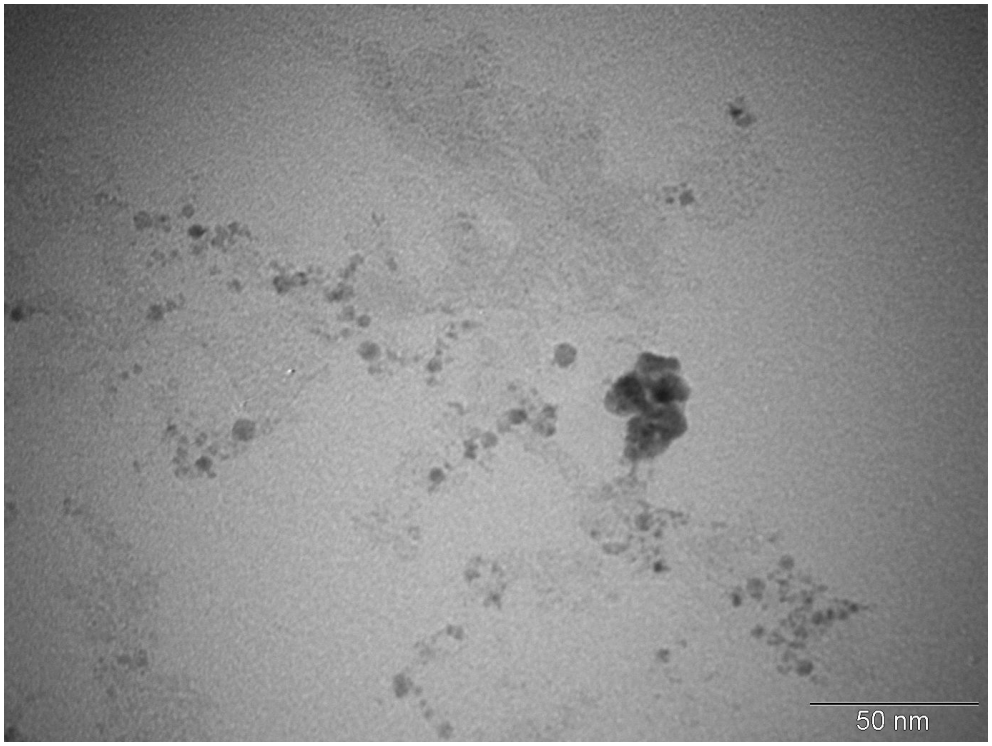

Figure 4.24: TEM image (scale bar of 50 nm) of region 2 of (Ni NPs)^{pr}.

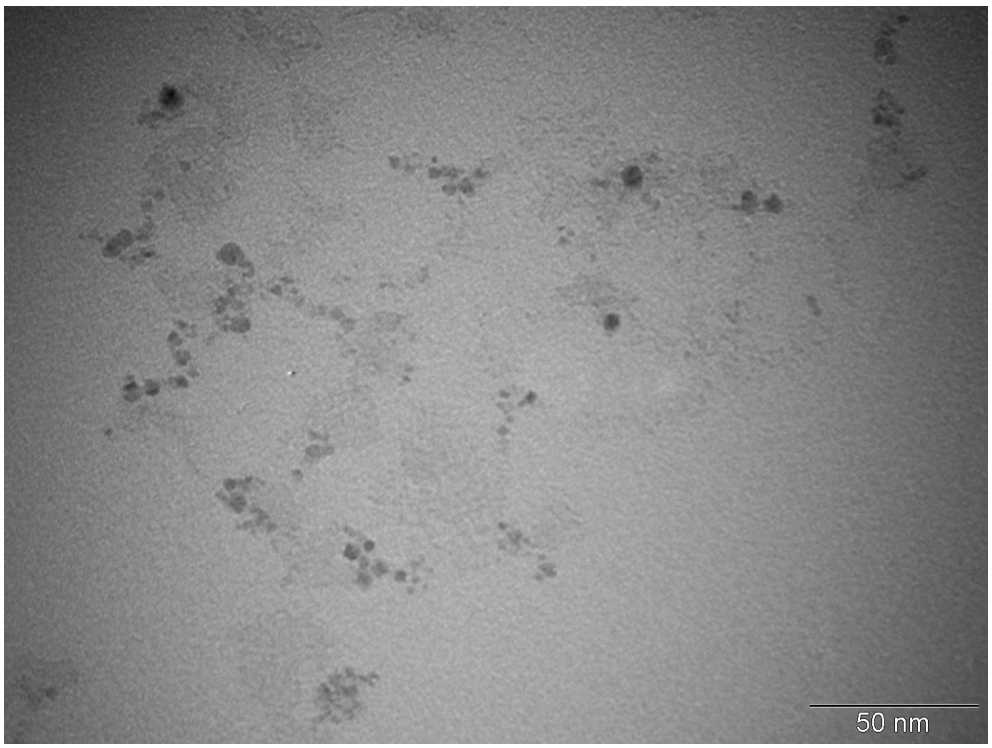

Figure 4.25: TEM image (scale bar of 50 nm) of region 3 of (Ni NPs)^{pr}.

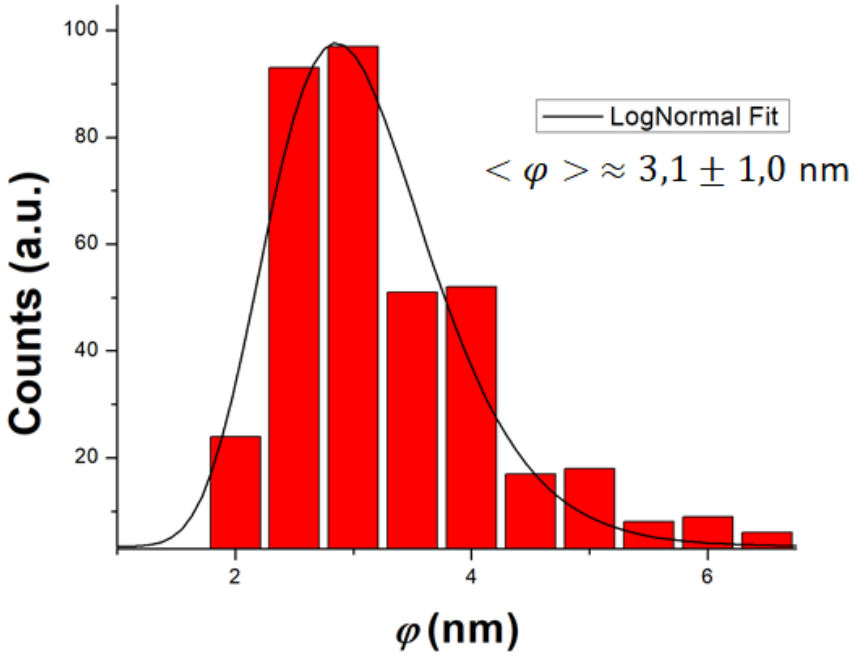

Figure 4.26: Histogram of the nanoparticle sizes of (Ni NPs)^{pr}, associated to the analysis of regions 1, 2 and 3 of the same component.

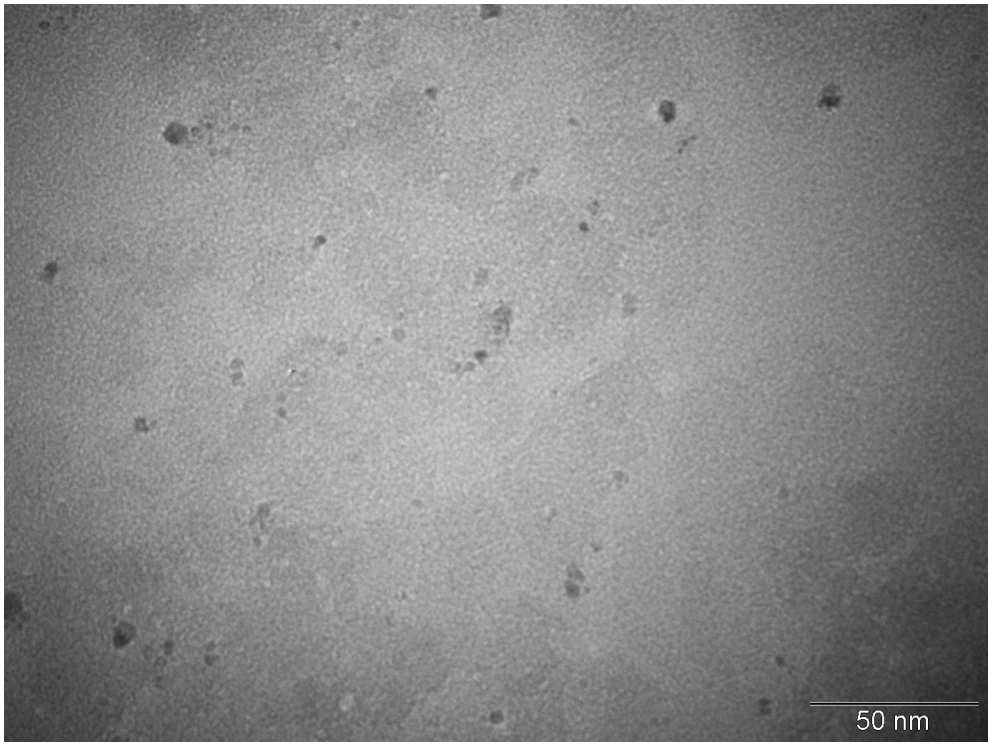

Figure 4.27: TEM image (scale bar of 50 nm) of region 1 of (Ni NPs)^{sp}.

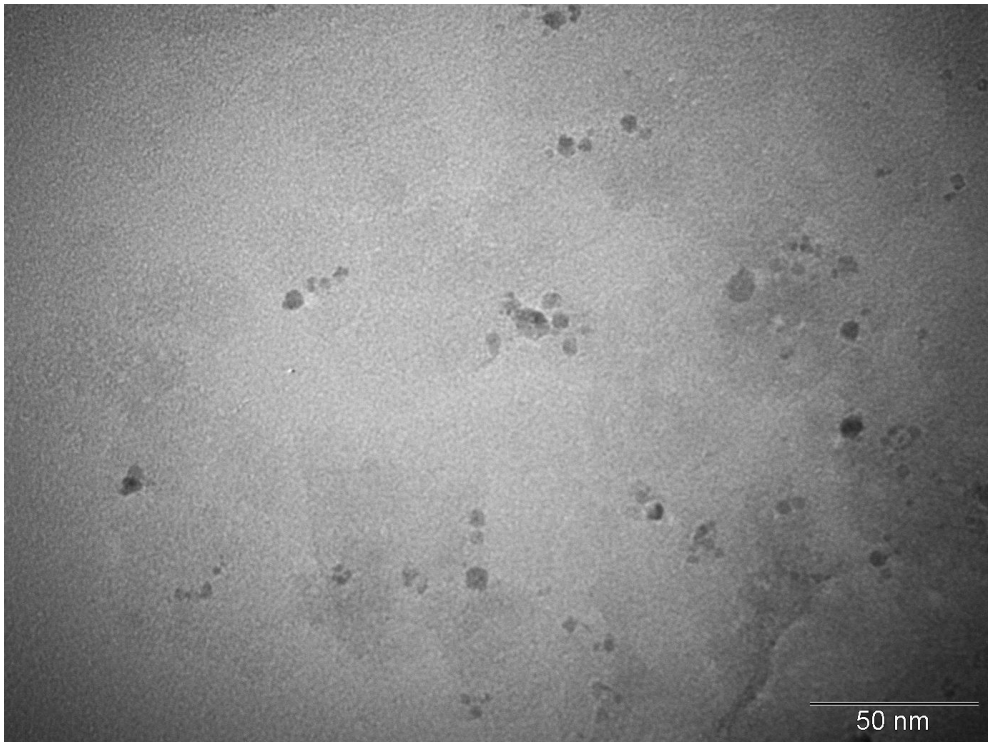

Figure 4.28: TEM image (scale bar of 50 nm) of region 2 of (Ni NPs)^{sp}.

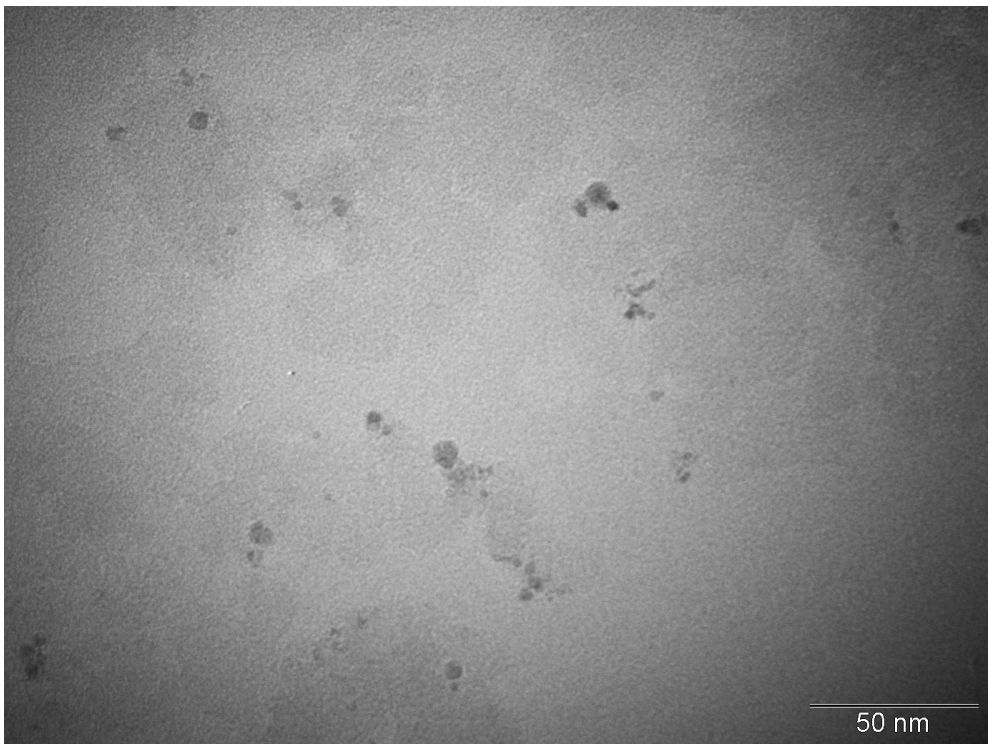

Figure 4.29: TEM image (scale bar of 50 nm) of region 3 of (Ni NPs)^{sp}.

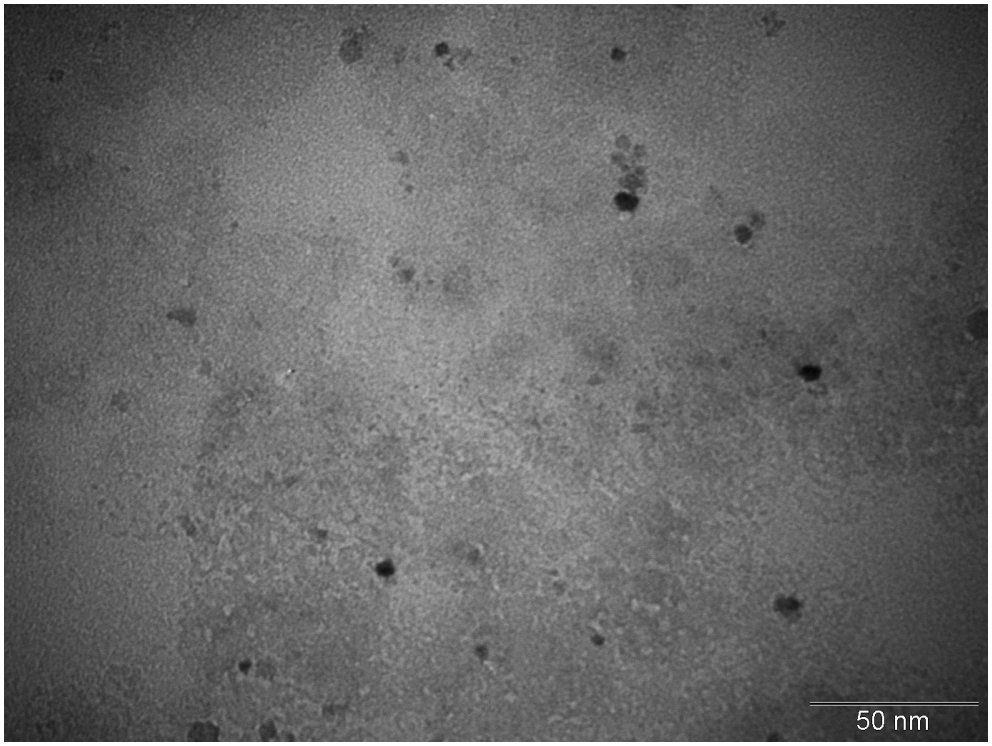

Figure 4.30: TEM image (scale bar of 50 nm) of region 4 of (Ni NPs)^{sp}.

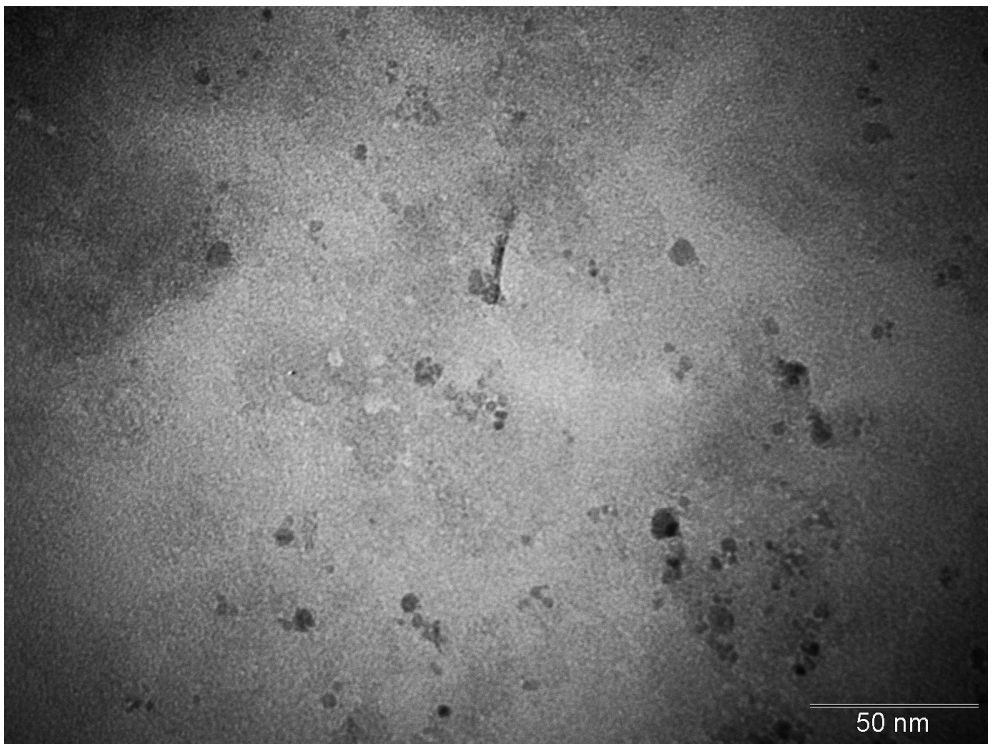

Figure 4.31: TEM image (scale bar of 50 nm) of region 5 of (Ni NPs)^{sp}.

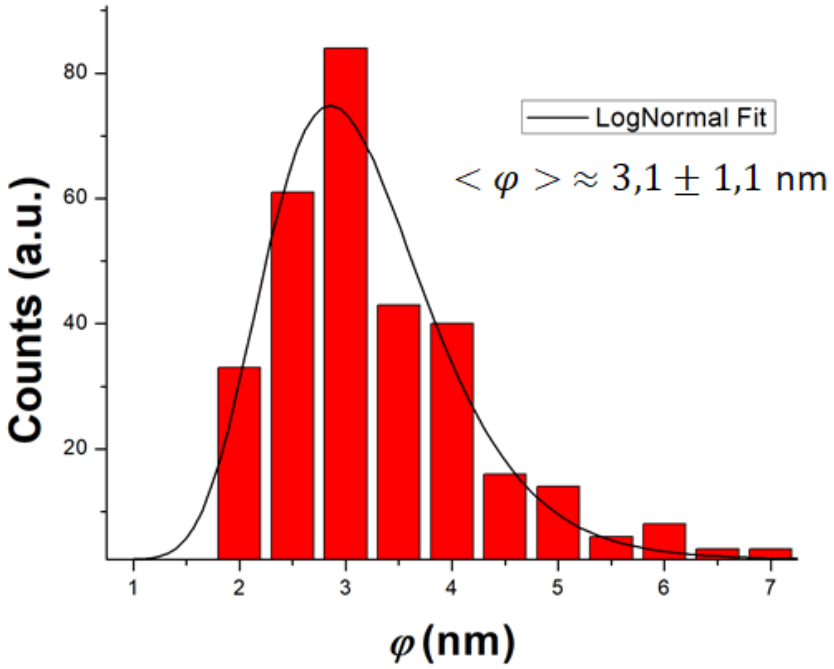

Figure 4.32: Histogram of the nanoparticle sizes of (Ni NPs)^{sp}, associated to the analysis of regions 1, 2, 3, 4 and 5 of the same component.

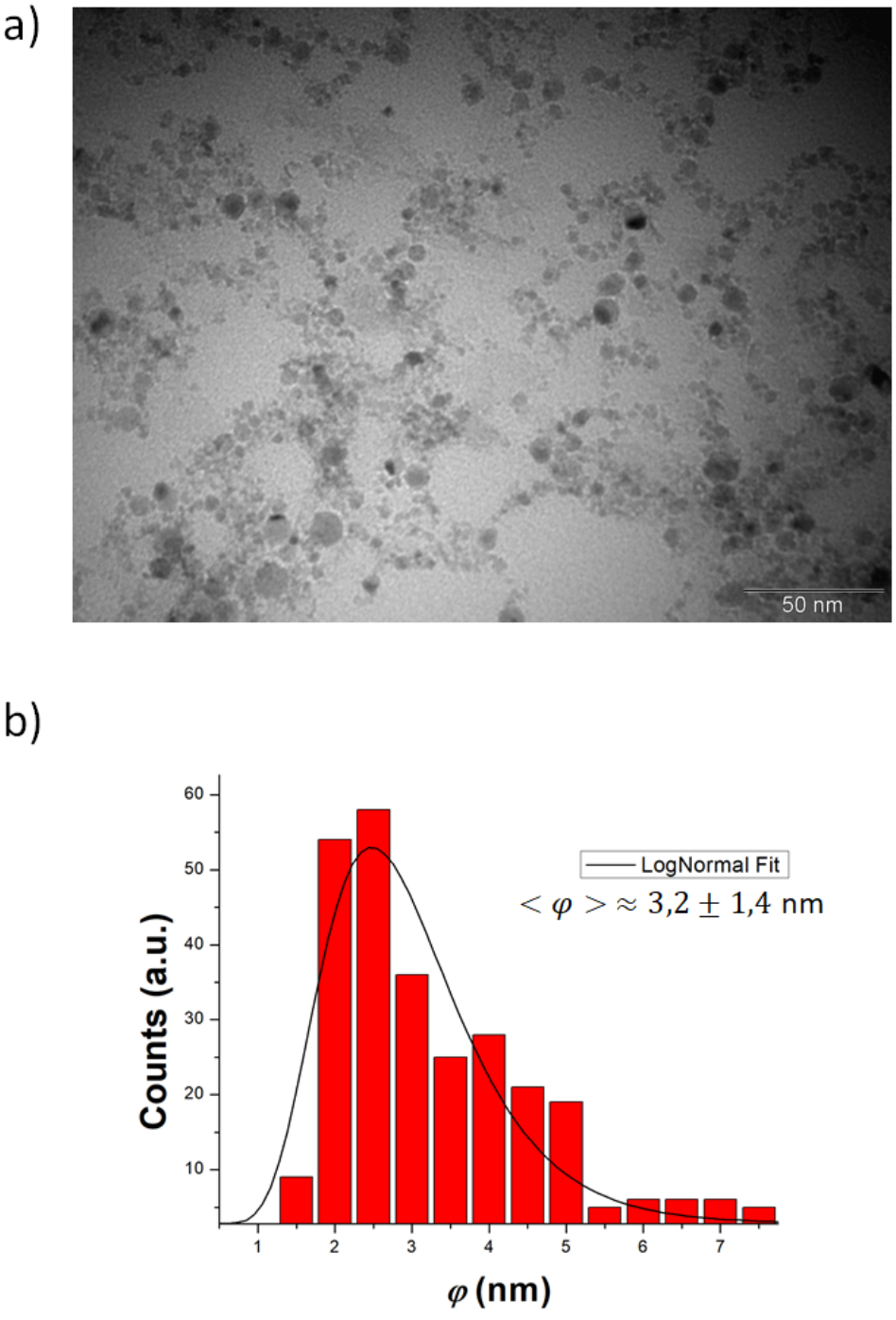

Figure 4.33: (a)TEM image (scale 50 nm) with the histogram (b) of the nanoparticle sizes of $(\text{Ni NPs})^{\text{mix}}$.

4.3.3
Structures different from small spherical nanoparticles

In the "Introduction" Chapter, we highlight that nanostructures with a shape different from spherical NPs were observed in the TEM images of the samples.

For example, in Figure 4.34 is shown an image of what resemble $Ni(HCO_3)_2$ nickel-bicarbonate nanosheets [11], observed in the $(Ni\ NPs)^{sp}$. It is evident the similarity with the structures shown in Figure 2.8 of the theoretical introduction section, concerning the description of nickel oxides and hydroxides.

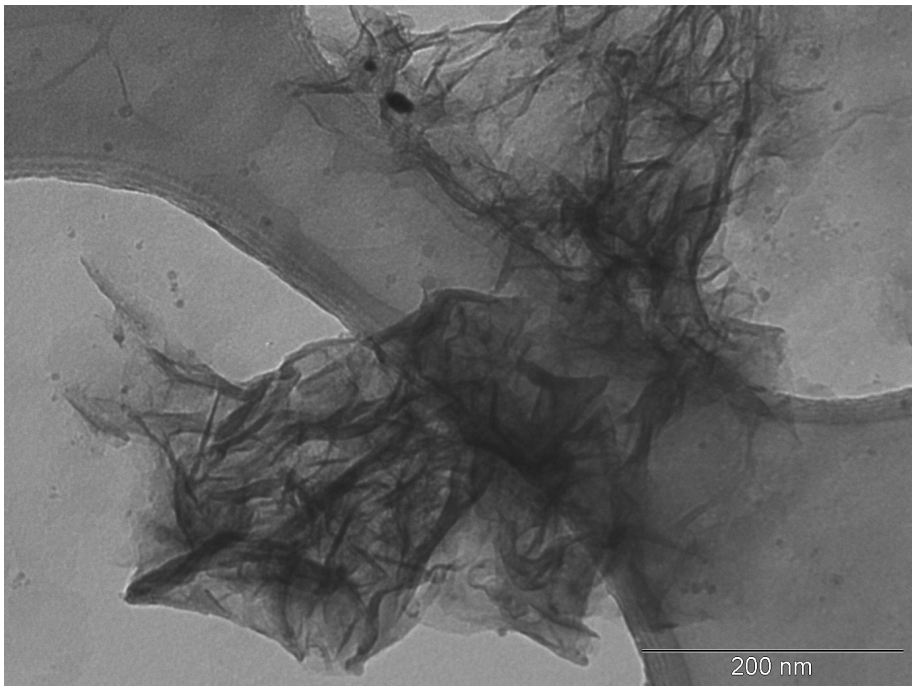

Figure 4.34: Possible $Ni(HCO_3)_2$ nickel-bicarbonate nanosheets present in the $(Ni\ NPs)^{sp}$ sample. The nanostructures are very similar to the ones reported in [11].

Together with these structures, also graphitic sheets were observed in both Ni and Fe derived nanomaterial, such as the one represented in Figure 4.35. However, the same structures were also identified in the TEM images of the Au grids used for TEM before the deposition of the material, as shown in Figure 4.36.

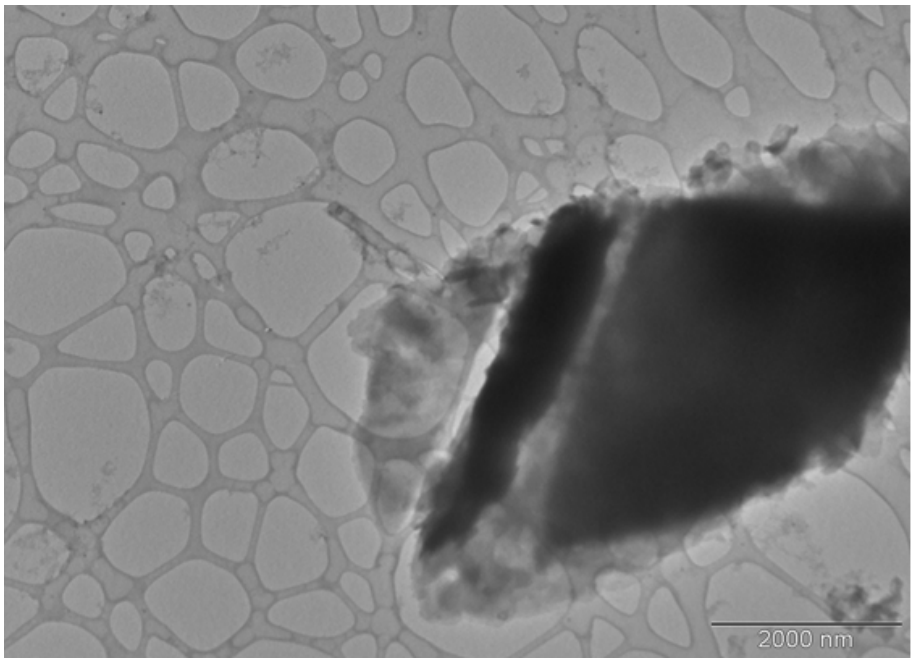

Figure 4.35: TEM image of the graphitic sheet in (Fe NPs)^{sp}.

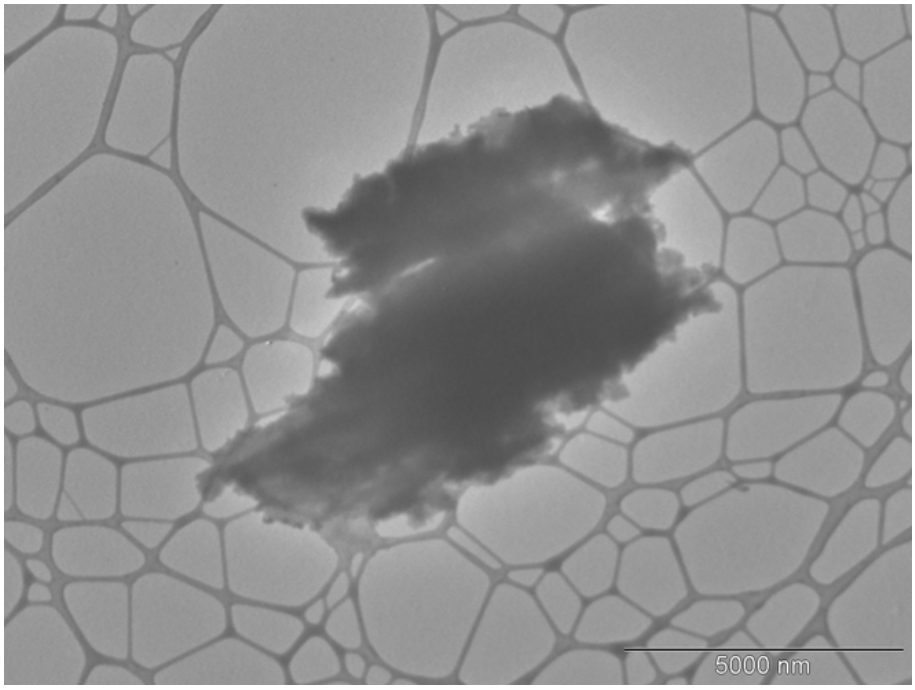

Figure 4.36: TEM image of graphitic sheet in UC-A on holey 300 mesh Au grids before the deposition of a sample.

4.3.4
Discussion about TEM measurements

As it was briefly exposed in Chapter 1, PLA of Fe in deionized water results mostly in the synthesis of NPs with an average size diameter between 7 and 17 nm by the use of first(ω) and second harmonic(2ω) lasers, respectively [13]. In only one article, Iwamoto et al. found smaller Fe NPs in the range of 1 to 5 nm using first harmonic laser pulses, but performing ablation along a time of about 1 h, which is relatively higher when compared to the standards ablation times, which are of the orders of tens of minutes or only some units of minutes [103].

Considering Ni targets, experimental works using 2ω and 3ω frequency laser pulses in deionized water lead to average diameters between 3 and 10 nm, respectively [14, 49].

In comparison to the cited works, the average diameter of NPs obtained during the PLA synthesis using the parameters reported in chapter 3 are relatively smaller.

As introduced in the theoretical section, a common procedure used to control and limit the average size of the NPs synthesized by PLA in liquids is the introduction of proper surfactants and stabilizing agents in the aqueous environment, which limits the recombination time of clusters and atoms during the plasma cooling [3, 103]. This effect was highlighted also in [5], concerning the dimension of colloidal dispersion of iron-oxide NPs produced by PLA of iron targets in water. In that case, the average diameter of the $(\text{Fe NPs})^{\text{pr}}$ and $(\text{Fe NPs})^{\text{sp}}$ was about 11 nm and 6 nm, respectively. The lower values reported in the present research might be associated to the different experimental parameters used during the PLA process, as resumed in Table 4.3.

	Results of [5]	Results of dissertation
F	2.3 J/cm^2	6.0 J/cm^2
Liquid Volume	5 mL	12 mL
t_{PLA}	2 h	5 h
$(\text{Fe NPs})^{\text{pr}}$	11.2 ± 4.9 nm	6.0 ± 2.0 nm
$(\text{Fe NPs})^{\text{sp}}$	6.0 ± 1.6 nm	4.2 ± 1.0 nm

Table 4.3: Comparison of laser fluence(F), liquid volume, ablation duration(t_{PLA}) and average diameters of $(\text{Fe NPs})^{\text{pr}}$ and $(\text{Fe NPs})^{\text{sp}}$ between [5] and this dissertation.

Particularly important is the use of higher values of F and longer ablation times (t_{PLA}). While the dimension of the NPs is generally reported to be

greater with the increase of the fluence of the laser pulse [47, 48], increasing of the ablation time leads to smaller dimensions [14].

Our interpretation points to the increasing concentration of organics ligands or solid carbon on the surface of the NPs and/or in free state in water solution during PLA, as proposed in the scheme reporting the proposed CO_2RR. Similarly to surfactants used during LASiS, the presence of organics ligands would limit the time available for the recombination of metal-clusters, so limiting the final dimensions of the NPs.

4.4
Physical-Chemical Characterization

In this section, we will show and discuss the identification by EDS, Raman spectroscopy, FTIR and EELS of the metal oxides and organic material synthesized during LASiS in water. As explained in Chapter 3, the samples for the EDS measurements were obtained including a water rinsing process, while Raman and FTIR were performed after separation by magnetization without water rinsing. Finally, EELS investigation has been performed on the pristine material before any separation. As consequence, the organic material identified by EDS is adsorbed in the surface of the metal nanoparticles.

We remember here that in the present research FTIR and Raman spectroscopies were only performed on Ni NPs, while EELS only on Fe NPs.

4.4.1
EDS

The EDS measurements were made only for the samples of $(\text{Fe NPs})^{\text{pr}}$, $(\text{Ni NPs})^{\text{pr}}$ and $(\text{Ni NPs})^{\text{sp}}$, considering that the presence of different structures were observed in those samples. In order to detect the carbon element, we used SiO_x grids for this investigation and, in order to avoid the possible degradation of the organic material, the corresponding image was taken in STEM (Scanning Transmission Electron Microscopy) modality, using an electron acceleration voltage of 80 kV.

4.4.1.1
Fe derived nanomaterial

The results of $(\text{Fe NPs})^{\text{pr}}$ are presented in Figure 4.37 in which is evidenced the peaks of C and Fe, besides the peaks related to O, Na, Si. It was measured regions R1,R2 and R3 of the $(\text{Fe NPs})^{\text{pr}}$ in SiO_x grid, as presented in Figure 4.37.

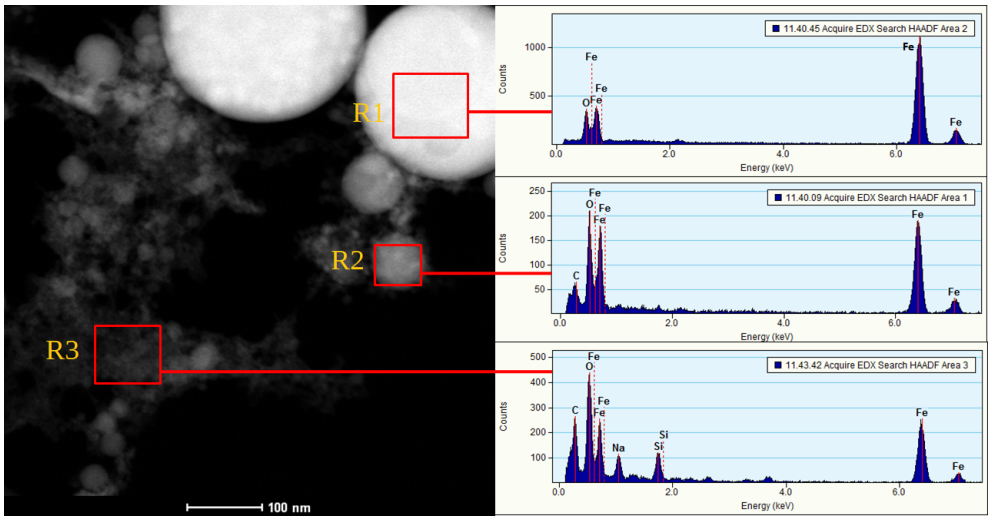

Figure 4.37: STEM image at acceleration voltage of 80 kV with the regions denoted by R1, R2 and R3 analised by EDS (on the left), together with the corresponding EDS spectra of (Fe NPs)^{pr}.

4.4.1.2
Ni based nanoparticles

EDS spectra of (Ni NPs)^{pr} and (Ni NPs)^{sp} are presented in Figures 4.38 and 4.39, respectively. In both the species, in different point of the samples we identified peaks of Ni, C, Si and O. We highlight that for the (Ni NPs)^{sp}, the EDS analysis made in region R1 corresponds to a part of the nanosheet structures observed before in Figure 4.34.

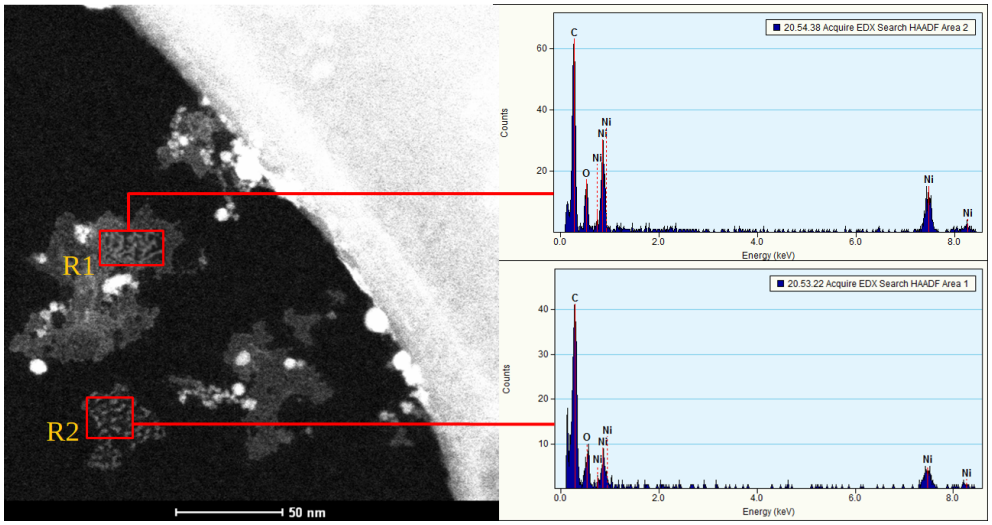

Figure 4.38: STEM image at electron acceleration voltage of 80 kV with regions denoted by R1, R2 and R3 analised by EDS (on the left), together with their corresponding EDS spectra of (Ni NPs)^{pr}.

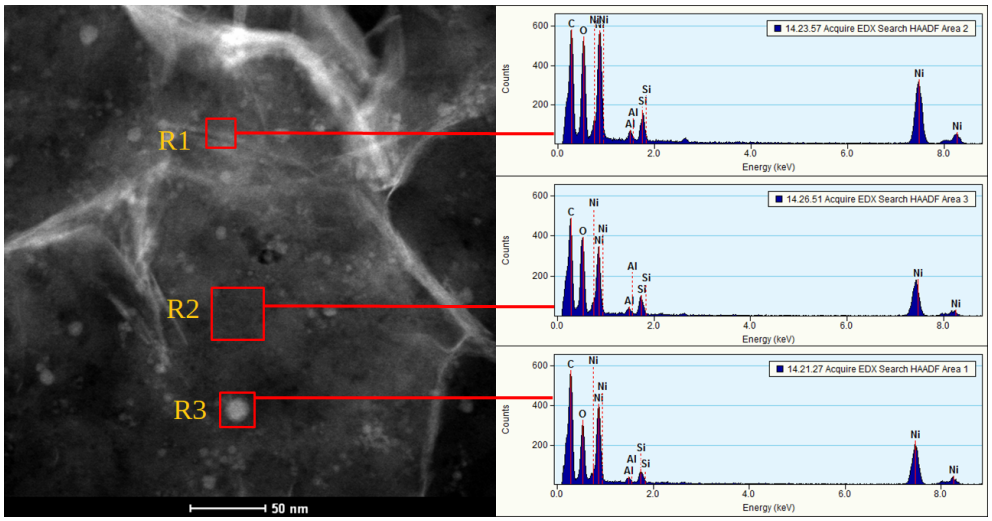

Figure 4.39: STEM image at electron acceleration voltage of 80 kV with the regions denoted by R1, R2 and R3 analised by EDS (on the left), together with the corresponding EDS spectra of (Ni NPs)^{sp}. Specifically, region R1 measured correspond to a part of a similar structure showed in Figure 4.34.

4.4.1.3 Discussion about EDS measurements

The presence of peaks of Fe and O in Figure 4.37, might be attributed to the presence of iron-oxides . Anyway, the O peak, alongside the Si peak, is always present on grids used for this experiment. The important result, is the observation of the carbon peak, which supports the formation of organic material during PLA of Fe target, as reported by Raman measurements in [5]. In that research, Raman investigation detected the presence of classical iron-oxides (magnetite, hematite, wustite), together with carbon based material, in the form of amorphous carbon and siderite $FeCO_3$.

The same exciting results have been observed in the Ni derived nanomaterial, where in both the precipitant and supernatant parts, we detected the presence of the carbon element. Particularly interesting are the results on the supernatant part, which has been analyzed in three different regions, denoted as R1, R2, and R3. While regions 2 an 3 are relative to nanoparticles, the region 1 was centered over the needle like structures. In the last case, the results are hence coherent with the possible formation of $Ni(HCO_3)_2$ nanosheets.

4.4.2 EELS

In Figure 4.40, we report the results of EELS for the (Fe NPs)^{mix}, alongside the image of the region measured. Three main peaks are present. The peak at 702 eV is attributed to Fe linked to O atoms [121, 122], the peak in 535 eV is related to the presence of oxygen, [119, 120], and the last one at 297.5 eV is associated to the presence of carbon [116, 117, 118].

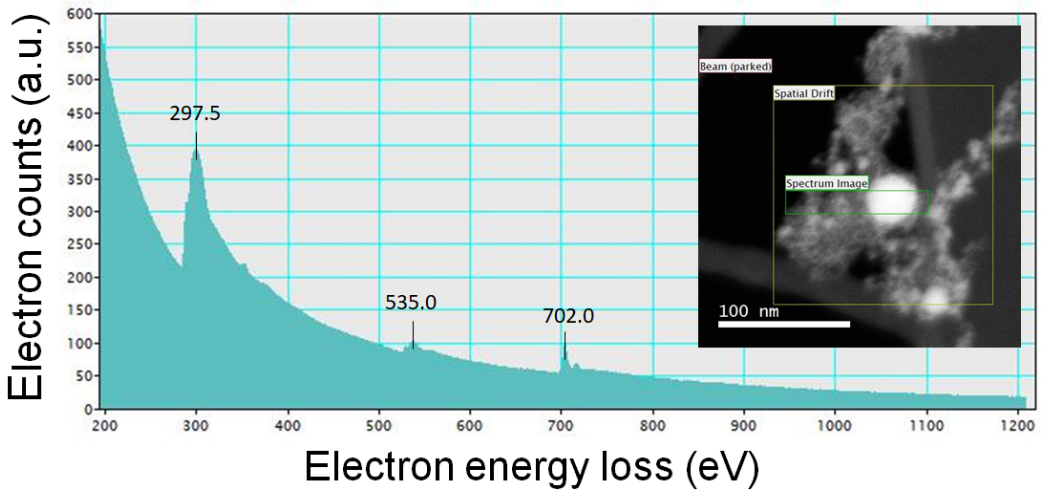

Figure 4.40: EELS spectra of (Fe NPs)^{mix} sample. In the inset, the observed region of the sample.

The results, are coherent with the EDS measurements.

4.4.3
Raman spectroscopy on Ni derived nanomaterial

In Figure 4.41 are reported the typical Raman spectra of the (Ni NPs)^{pr}. The Raman spectra of the (Ni NPs)^{sp} are instead shown in Figures 4.42 and 4.43, since two different set of frequencies were observed in this case. In both cases, the spectra were measured in different points of the same structure showed as inset. The main peaks observed for those spectra are reported in Table 4.4 for (Ni NPs)^{pr} , and Tables 4.5 and 4.6 for (Ni NPs)^{sp}.

The theoretical Raman frequencies associated to the phonons and magnons of the crystalline NiO oxide NPs, are conventionally indicated as TO (one-phonon transversal optical mode), LO (one-phonon longitudinal optical mode), 2TO (two-phonon transversal optical mode), TO+LO (two-phonon transversal+longitudinal optical mode), 2LO (two-phonon longitudinal optical mode) and 2M (two-magnon band), and are listed as reference in Table 4.7 [104]. In Table 4.8, we report instead the theoretical Raman frequencies associated to the phonons of nickel-hydroxide $Ni(OH)_2$ (more specifically, β-$Ni(OH)_2$) [105]. In the latter case, the phonons are indicated as irreducible representations, specifically, translational modes A_{1g}(T) (single degeneracy), E_g(T) (double degeneracy) and E_u, and the rotational mode E_g(R) [105, 106, 107].

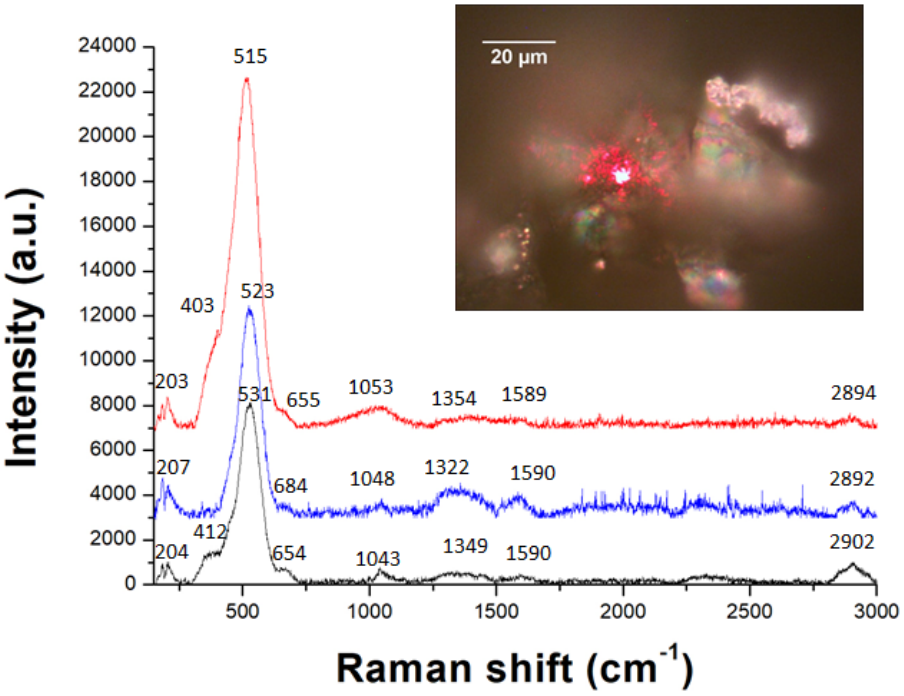

Figure 4.41: Raman spectra of the region of (Ni NPs)^{pr} powder. The spectra were measured in three different points of the same structure. In the inset, the optical microscope image of the structure containing the points R1(red spectrum), R2(blue spectrum) and R3(black spectrum). In the specific case, the red laser spot was exciting at point R1.

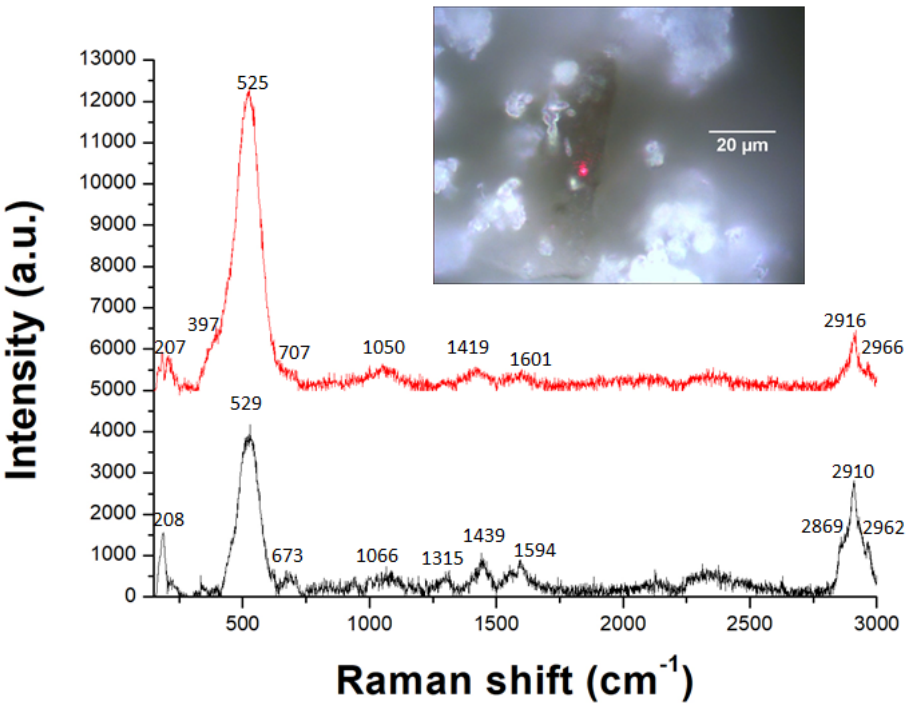

Figure 4.42: Raman spectra of the region of (Ni NPs)^{sp} powder. The spectra were measured in three different points of the same structure. In the inset, the optical microscope image of the structure containing the points R1(red spectrum) and R2(black spectrum). In the specific case, the red laser spot was exciting at point R1.

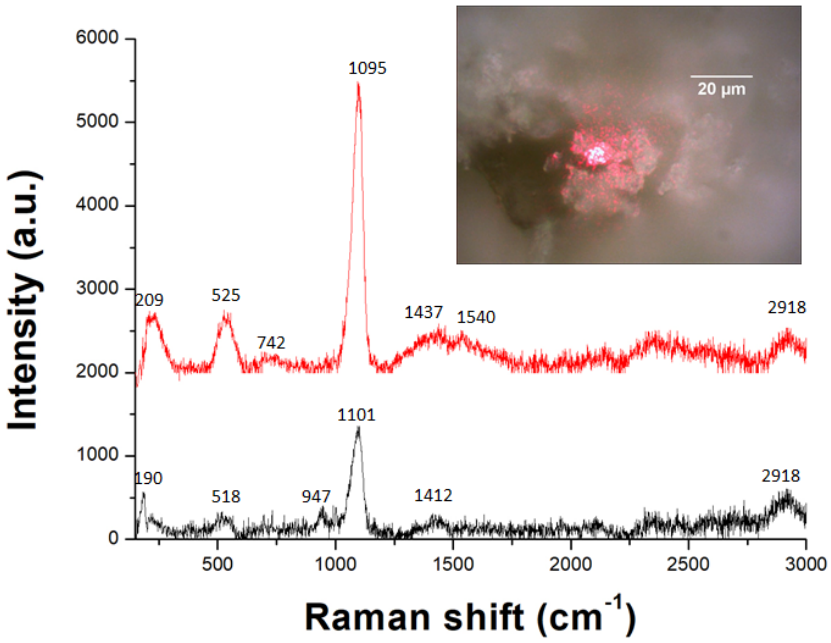

Figure 4.43: Raman spectra of another region of (Ni NPs)^{sp} powder. The spectra were measured in three different points of the same structure. Only the highest intensity peaks of the regions are presented. From different regions measured, the peak around 1100 cm^{-1} shifts from the original position. Also, the higher its intensity, the lower the peak in the range of 500-530 cm^{-1}. In the inset, the optical microscope image of the structure containing the points R3(red spectrum) and R4(black spectrum). In the specific case, the red laser spot was exciting at point R3.

Samples	Raman frequency (cm^{-1})						
$(Ni\ NPs)^{pr}$ R1	403	515	655	1053	1354	1589	2894
$(Ni\ NPs)^{pr}$ R2	474	523	684	1048	1360	1590	2892
$(Ni\ NPs)^{pr}$ R3	412	531	654	1043	1349	1590	2902

Table 4.4: Main Raman frequencies (cm^{-1}) identified in the points R1, R2 and R3 of $(Ni\ NPs)^{pr}$.

Samples	Raman frequency (cm^{-1})							
$(Ni\ NPs)^{sp}$ R1	449	525	707	1050	-	1419	1601	2916
$(Ni\ NPs)^{sp}$ R2	472	529	673	1066	1315	-	1590	2910

Table 4.5: Main Raman frequencies (cm^{-1}) identified in the points R1 and R2 of $(Ni\ NPs)^{sp}$.

Samples	Raman frequency (cm^{-1})							
$(Ni\ NPs)^{sp}$ R3	525	742	-	1095	1437	1540	2357	2918
$(Ni\ NPs)^{sp}$ R4	518	-	947	1101	1412	-	2312	2918

Table 4.6: Main Raman frequencies (cm^{-1}) identified in the points R3 and R4 of $(Ni\ NPs)^{sp}$.

Raman → modes	TO (cm^{-1})	LO (cm^{-1})	2TO (cm^{-1})	TO+LO (cm^{-1})	2LO (cm^{-1})	2M (cm^{-1})
NiO	440	560	740	925	1100	1400

Table 4.7: Raman frequency (cm^{-1}) of the modes associated to the phonons and magnons of NiO as reported in [104].

Raman → modes	A_{1g}(T) (cm^{-1})	E_g(T) (cm^{-1})	E_u(T) (cm^{-1})	E_g(R) (cm^{-1})
$Ni(OH)_2$	315	450	517	880

Table 4.8: Raman frequency (cm^{-1}) of the modes associated to the phonons of $Ni(OH)_2$ as reported in [105].

Concerning the Raman spectra of the $(Ni\ NPs)^{sp}$ and $(Ni\ NPs)^{pr}$ species, reported in Figures 4.41 to 4.43, the band in the region of 500-530 is characteristic of Ni-O stretching, which indicates the presence of nickel oxide NiO and/or nickel hydroxide $Ni(OH)_2$ [70]. Usually, for $Ni(OH)_2$, there are another

bands in the spectrum in positions 315 and 450 cm^{-1} [70, 105, 106, 107]. Although the peaks in the range of 400-450 cm^{-1} found in some of our spectra could be related to the phonon E_g(T) of $Ni(OH)_2$, we cannot identify the A_{1g}(T) mode. Anyway, it is worth noting that FTIR spectroscopy is better suited than Raman investigations in order to discriminate between nickel oxides and hydroxides[70]. As mentioned also by Gellini et al.[70], the presence of both oxide and hydroxide species is expected by PLA of Ni target in water. In the same research, the authors propose in fact that molecular oxygen O_2 dissolved in water might interact with both Ni^{+2} and H_2O molecules, forming the hydroxide compound[70]. Then, the nickel-oxide NiO would be produced after a dehydration process of $Ni(OH)_2$.

As explained previously, generally the bands with weak intensity showed in the range of 600-1000 cm^{-1} , are interpreted in terms of NiO phonons, but it is worth noting that mostly the experimental frequencies differ considering different authors [109, 110, 104]. Due to this, it's possible to interpret our experimental peaks in the range 400-480 cm^{-1} as TO, 500-530 cm^{-1} as LO, and in the range 600-700 cm^{-1} as 2TO. The band that we observe around 900-1000 cm^{-1} cannot be associated to the TO+LO mode, since the experimental full width half maximum (FWHM) is about 100 cm^{-1}, to be compared with a typical FWHM of the TO+LO of about 200 cm^{-1}. [140, 110]. Finally, we cannot exclude the presence of a small 2M peak close to 1400 cm^{-1}, which might be covered by the other bands observed in the range between 1350-1600 cm^{-1} . We associate all the other bands present in the Raman spectra to the presence of carbon based organic material.

Specifically, in the case of the $(Ni\ NPs)^{pr}$, some of the spectra show a weak band centered around 1050 cm^{-1}, two small bands of the same intensity centered around 1350 cm^{-1} and 1590 cm^{-1}, and a broad band centered around 2900 cm^{-1}. We associate the first one to the presence of HCO_3^- [108], and the last one to the C-H stretching vibrations of organic material produced during the PLA. The remaining two bands are associated to the presence of amorphous graphitic carbon [9, 10], where sp^2 domains exist in an amorphous sp^3 carbon matrix, as explained in subsection 2.7.

A similar behavior is observed for the $(Ni\ NPs)^{sp}$, with the particular that some of the spectra are dominated by a sharp and intense line between 1080-1100 cm^{-1} (Figure 4.43, Table 4.6), which it might be attributed to regions of the samples with a higher content of CO_3^{-2}[108]. Again, another possible interpretation is based on the great similarity between the $Ni(HCO_3)_2$ nanosheets synthesized by X. Zhang et al. [11], and the sheets like nanostructures reported for the $(Ni\ NPs)^{sp}$ in Figure 4.34, which were briefly discussed in section 4.3.

S. Dai et al. [66], reported a Raman spectrum dominated by an intense line around 1115 cm^{-1} for $Ni(HCO_3)_2$ nanoparticles, so that it is possible that the high intensity bands reported in Figure 4.43 for the supernatant part are associated to the nickel-bicarbonate nature of the synthesized nanosheets.

4.4.4
FTIR spectroscopy on Ni derived nanomaterial

The FTIR spectra of (Ni NPs)^{pr} and (Ni NPs)^{sp} are shown in Figure 4.44, while Table 4.4.4 are reported the experimental frequencies of interest.

The spectra seems to indicate that the functional groups on the surface of the NPs, are similar in the case of precipitant and supernatant parts. The bands in the range of 420-618 can be associated to the phonons A_{1g} of β-$Ni(OH)_2$[64, 63]. Concerning the bands centered at 3381 cm^{-1} and 1635 cm^{-1}, they are associated to the stretching $\nu(H_2O)$ and bending $\delta(H_2O)$ of adsorbed or intercalated water molecules, while the sharp resonance at 3641 cm^{-1} is characteristic of the free OH stretching vibration in brucite like-structures [111, 112], and represents a fingerprint of β-$Ni(OH)_2$ hydroxide phase [111].

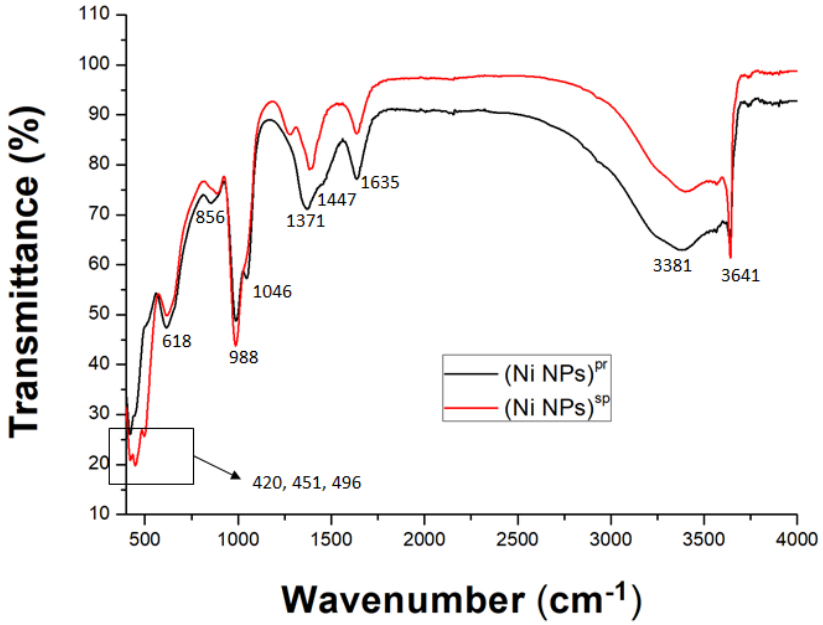

Figure 4.44: FTIR spectra of (Ni NPs)^{pr} and (Ni NPs)^{sp} powder. The wavenumber of the highest intensity peaks are presented.

The bands around 856 and 1447 cm^{-1}, which have higher relative intensity in the precipitant part, are coherent with the possible presence of intercalated carbonate ions [113, 65], which is only possible in the presence of α-$Ni(OH)_2$ hydroxide phase [63]. Although the bands at 988 and 1046 cm^{-1} would be coherent with the presence of nitrogen intercalated α-$Ni(OH)_2$ hydroxide, the bands should be accompanied by the highest intensity absorption around 1300 cm^{-1} [63], so that we exclude this interpretation. We associate the peaks around 1046 and 1371 cm^{-1} to the ν(C-OH) vibration and ν(O-H) bending of epoxide or hydroxyl groups [114, 115], and the bands at 988 cm^{-1} to the

ν(C-O-C) vibration of epoxy group on the surface of the amorphous graphitic carbon detected by Raman spectroscopy [115]. In this frame, the band at 1635 cm^{-1} might also be a stretching of C=C of aromatic ring of the amorphous graphitic carbon [136].

Samples	FTIR frequency (cm^{-1})							
$(Ni\ NPs)^{pr}$	419	615	856	1046	-	1371	3381	3638
$(Ni\ NPs)^{sp}$	451	618	889	-	1280	1384	3403	3641

Table 4.9: Main FTIR frequencies (cm^{-1}) identified in $(Ni\ NPs)^{pr}$ and $(Ni\ NPs)^{sp}$.

4.5 Astrochemical implications

In both the Introduction and Theoretical Chapters, we discussed how the laser ablation of Fe or Ni targets immersed in water can be used to simulate some space wheatering processes, such as the impacts of micrometeorites on the surface of minor bodies of the outer Solar System, or interactions between cosmic dust grains covered by astrophysical ice.

In this, different and interesting information comes from the experimental results previously discussed in this Dissertation. In the astrophysical frame, we will not differentiate the results on Fe from the ones of Ni, since both the elements are present in the astrophysical objects of interest involved in the space weathering processes. The presence of carbonates and bicarbonates in the metal-oxide nanostructures, highlights that CO_2 is indeed involved in the nanoparticles synthesis process. Considering the PLA-CO_2RR scheme reported in Figure 2.9, carbonates and bicarbonates are essentially the starting point of the chains of molecules we expect to detect, since they represent the natural form of CO_2 in water environment. Complementary, the amorphous graphitic carbon observed by Raman spectroscopy represents the final point of the chain, where the hydrocarbons and alcohols are eventually converted to solid carbon.

We suggest two possible interpretations for the lack of detection of intermediate products: 1) the concentration is too low to be detected by Raman or FTIR spectroscopy, 2) they are readily converted to solid carbon by a unique pulse or eventually through the interaction of the subsequent laser-pulses along the PLA process in water. In fact, it is important to highlight that along the 5 hours of PLA in water, the sample is irradiated with about 3×10^{12} laser-pulses, and there is the possibility that the species in the liquid environment (gases, water, organics products, nanoparticles) may interact with more than one-pulse.

In this sense, we will have to further investigate how the PLA process with the specific experimental parameters used in this work compares to the space weathering effects in space, in terms of the astrophysical collisional rates and timescales in different space environments. This specific study, involving not only experimental data but also observational and theoretical data, will be the focus of one of the publications which will come out from this Dissertation.

According to the astrochemistry literature, hydrocarbons are present in the surface of carbonaceous chondrite meteorites, alongside carboxylic acids, as shown in Table 4.10.

Besides this, carbonates are also present in them. They are in the form of minerals of Ca, Mg and Fe , such as calcite($CaCO_3$), dolomite($CaMg(CO_3)_2$)

Chemical compound	Concentration (ppm)
Aliphatic hydrocarbons	>35
Aromatic hydrocarbons	15-28
Carboxylic acids	>300

Table 4.10: Organic material concentration (ppm) in carbonaceous chondrite meteorites. Based on [92].

Group	Graphite
IA	common
IB	common
IC	dc
IIIE	dc

Table 4.11: Graphite content in iron meteorites groups. "dc" means "decomposed by carbide". Based on [125].

and breunnerite($(Mg,Fe)CO_3$). Moreover, also traces of nickel-carbonate have been encountered in iron meteorites [141]. Remembering the first results of the *NanoLaserLab* on the PLA of Fe target in water demonstrated the presence of $FeCO_3$ (siderite) [5], we can conclude that the production of both iron and nickel carbonates in space can be well simulated by our proposed PLA approach, and that nanoparticles formation may have a great importance for the physico-chemical evolution of the astrophysical species and molecules of interest.

Moreover, in the class of iron meteorites are present carbon structures mostly composed of graphite (Table 4.11) and literature reports that amorphous carbon can be present in the core of cosmic dust [23, 126]. Some of this graphite structures can be formed by decomposition of the carbides, structures made of metal and carbon (such as Fe_3C and $(Fe,Ni)_{23}C_6$) [125].

The detection of graphitic amorphous carbon as product of PLA of both Ni e Fe targets, is hence the second important experimental result to be linked with the astrochemical investigation. The possibility of the creation of solid carbon is particularly important for understanding the evolution of the carbon component of cosmic dust [20]. In fact, different from the more resistant silicates, the carbonaceous dust grains can be more easily destroyed by UV radiation, cosmic rays and shocking waves generated by nearby supernovae, although they are are still observed in the interstellar medium. This means that some not yet fully understood re-formation mechanism takes place in this space environment, able to explain the survival of carbon cosmic dust and its consequent detection in astronomical observations [20]. As far as we know, only

few experimental works have tried to investigate this aspect and only recently we are starting to get an idea about the chemical-physical processes involved in the regeneration of the carbonaceous dust grains [20]. In this context, the PLA-CO_2/C process can be considered as one of these first experimental steps shedding light on the processes of formation and evolution of carbon cosmic dust in space.

Finally, we want to highlight that even the PLA induced water splitting process, described in Section 2.6, has its importance in the astrochemistry frame. In fact, the models commonly used to describe the formation of H_2 within astrophysical ices (covering cosmic dust grains or the surface of minor bodies), don't take in account this unique process [123], which most probably has a great relevance for the sequential formation of organic material via the CO_2RR reported in Figure 2.9.

5
Conclusions

5.1
Nanomaterials synthesized by PLA-CO_2/C process on Fe and Ni targets

All the objectives relative to the synthesis and characterization of the nanomaterials by LASiS in water environment were fulfilled. The results were interpreted in the frame of the PLA-CO_2/C process described in details in section 2.7. The process is realized through the particular thermodynamic conditions of the PLA environment, which trigger the catalytic properties of Ni and Fe oxide nanoparticles. Different iron oxides were detected in our previous investigation, and nickel-oxide and/or hydroxide were detected by Raman spectroscopy in the present research. FTIR spectroscopy confirms the presence of β-$Ni(OH)_2$ hydroxides, although Raman measurements point to the inclusion of carbonate and bicarbonate species. This hypothesis is sustained by TEM and EDS measurements, which suggest the presence of traces of $Ni(HCO_3)_2$ nanosheets. Organic material is detected by Raman spectroscopy also in the form of graphitic amorphous carbon and CH stretching, in both Fe and Ni derived nanomaterial. Following our model, we propose that the solid carbon structures might be produced after condensation of C_n-units formed by reductions of FT reaction products.

We connect the presence of organic material to the particular average dimension of the NPs obtained by both Ni and Fe targets, which is considerably smaller than reported in previous works [13, 14, 49]. This is possibly related to the long ablation time used in the experiments, which allows the organic material to be synthesized in significant concentration, and used as stabilizing agent, limiting the recombination time of the metal nanoclusters, reducing the final size.

The experimental results obtained along the research, definitively confirm that CO_2 has an active and important role in the physical-chemical properties of the synthesized nanomaterial, and are definitively of great interest in the field of LASiS synthesis.

5.2 Final remarks about astrochemistry

As discussed in detail in section 2.7, PLA is an excellent tool for the experimental simulation of some space weathering processes, i.e., micrometeorite impacts. The metal targets(Fe and Ni) and the deionized water, offer a resemblance of the surface of some minor bodies of the Solar System and cosmic dust grains of interstellar medium, both covered with astrophysical ice. The interactions between these minor bodies and micrometeorites, as well as the interaction between the cosmic dust grains in the interstellar medium, can both be seen and compared to the laser ablation process, so that the production of nanomaterial after the impact is expected. When the astrophysical body suffering space weathering contains Fe and Ni, we expect that both WS, one-step CO_2RR and two-step CO_2RR reactions may happen, similarly to the case of the PLA-CO_2/C reactor.

The experimental conditions used in the present research, in which each sample was synthesized using an average number of laser-pulses of 3×10^{12}, are able to reproduce different carbon based structures of astronomical interest, such as $Fe(CO_3)$, $Ni(HCO_3)_2$, and amorphous graphitic carbon. The carbonates links the experimental results to the composition of part of the iron meteorites, while the solid carbon resembles more closely the cosmic dust grains.

Moreover, considering that the carbonaceous have low resistance against destructive phenomena occurring in in space (such as UV radiation and cosmic rays), and yet they are observed by astronomical observations [20], their "reformation" may be related, to some extent, to the interaction of silicate cosmic dust covered with H_2O, CO and CO_2 rich ices. This assumption connects again with the fact that the silicate cosmic dusts can have Fe in their composition and the astrophysical ice is around it, besides the correlation with these elements and our results. Additinal experimental work should be made to further investigate this hypothesis.

5.3 Future work and perspectives

The results concerning the identification and characterization of the produced nanomaterials, still need to be complemented by other experimental characterizations. X-Ray diffraction (DRX) will be fundamental to confirm our interpretation of Raman and FTIR results, revealing the kind of oxides and hydroxides present in the colloidal solutions. It will be particularly interesting to verify the presence of α-type nickel hydroxides, with the eventual inclusion of carbonate or bicarbonate. Also X-Ray photoelectron spectroscopy will help

for this purpose, and will allow the precise identification of the oxidation state of the metal in the nanoparticles.

While DRX will be performed in the National Institute of Metrology, Standardization and Industrial Quality of Rio de Janeiro (INMETRO), for XPS measurement we will take advantage of an international collaboration with the group of Prof. Stephan Barcikowski, Prof. Torsten Schmidt, and Prof. Sven Reichenberger of the Department of Chemistry from the University of Duisburg-Essen (Germany). They also will try to measure by in-situ gas-chromatography the CO and CH_4 gases produced during the PLA of the metals in pure water, at different CO_2 concentrations.

We finally want to highlight, that the presented research represent a proof-of-concept (POC) of the PLA-CO_2/C process, which has to be conducted in different experimental conditions to obtain the best results in term of the concentration of the produced organic material. In fact, in a near future, the experiments will be repeated controlling the relative pressure of CO_2 and CO at the gas-liquid interface of the PLA environment. We expect that, by increasing the CO_2 concentration from 0.04% to value of the order of about 5%, we should have a significant increment in the mass production of organic material. Even more interestingly, in the future we pretend to perform PLA of Fe and Ni targets in water using a gas atmosphere even more similar to the one characteristic of the astrophysical ices [127, 128, 129, 130], and repeating some of the experiments here presented by employing more energetic pulses to simulate the space weathering process (F = 40 J/cm^2) to be able to extend the investigation of micrometeorite impacts in space towards a different range of physico-chemical processes.

A
Supplementary material

A.1
Theory of Raman scattering

As the molecules of a sample interacts with electromagnetic radiation, it may provoke the displacement of the atoms from their equilibrium position, described as vibrations. The vibration response can be used as interesting tool to identify the nature of the molecules under investigation.

Mathematically, we can propose first in a classical approach that this excitation is expressed as a induced dipole reaction after photon interaction. The induced dipole, called as $\vec{P}$, will be then directly proportional to the electric field of the radiation ($\vec{E} = \vec{E_o}\cos(w_1 t)$), with a important term that relates to the the "electronic polarizability", α [131]. Then, we can obtain the expression of the induced dipole to identify the vibrations related to the photon interaction. The equation for the induced dipole is shown as follows:

$$\vec{P} = \alpha\vec{E} = \alpha\vec{E_o}\cos(w_1 t). \tag{A-1}$$

The α term, however, can be expanded in a more meaningful way, where it is expressed not only by a constant term, but also a fluctuation term(which depends of harmonic approximations for normal modes of vibration, Q_k, that are independent of each other):

$$\alpha = \alpha_o + \sum_k \frac{\partial\alpha}{\partial Q_k} Q_k + ... \tag{A-2}$$

Where:

$$Q_k = Q_{ko} cos(w_k + \delta_k). \tag{A-3}$$

And with the combination of those forms to the expression of induced dipole:

$$\vec{P} = \alpha_o\vec{E_o}\cos(w_1 t) + \sum_k \frac{\partial\alpha}{\partial Q_k} Q_{ko}\vec{E_o} cos(w_k + \delta_k)\cos(w_1 t) + ... \tag{A-4}$$

Yet, we still can use a trigonometric relation:

$$cos(\theta)cos(\phi) = cos(\theta - \phi) + cos(\theta + \phi). \tag{A-5}$$

To obtain the important formula as follows:

$$\vec{P} = \alpha_o \vec{E_o} \cos(w_1 t) + \sum_k \frac{\partial \alpha}{\partial Q_k} Q_{ko} \vec{E_o} [\cos((w_1 - w_k)t + \delta_k) + \cos((w_1 + w_k)t + \delta_k)] ... \tag{A-6}$$

Or in a more comprised way:

$$\vec{P} = \vec{P}(w_1) + \vec{P}(w_1 - w_k) + \vec{P}(w_1 + w_k). \tag{A-7}$$

The first term of the induced dipole formula is referred as the Raileigh 's term and the other ones as Raman Stokes and Raman Anti-Stokes terms, respectively. The Rayleigh scattering is referred to the scattering in which the frequency of emission of the molecule is the same as the one related to the incident beam propagated to the sample, also defined as a elastic scattering. In the case for the Raman scatterings, however, the frequencies of the incident beam and the emission of the molecule are different, which in turns defines both Stokes and Anti-Stokes as inelastic scatterings. The frequency of the vibrations of the molecules due to the interactions with the beam will give a characteristic spectrum, which is the fingerprint of the molecules under analysis. [131]

A.2
Photoluminescence(PL) spectroscopy

The transparent liquids obtained after another separation method which will be described in the section further were investigated by photoluminescence spectroscopy to identify the presence of luminescent organic material produced by PLA of Fe in water. The separation method used for it is described in the next subsection.

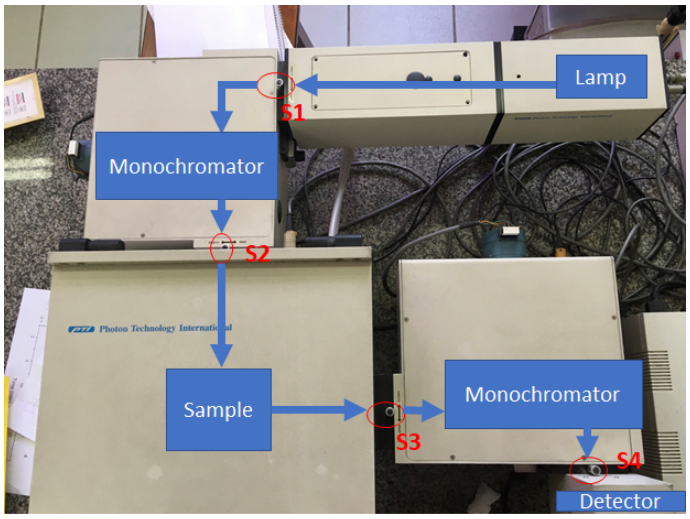

Figure A.1: Fluorimeter system from Photon Technology International, model QM-1, in the *Optical Spectroscopy Multiuser Laboratory* of Department of Physics of PUC-Rio. It is also shown the path of the light from the source to the sample until it reaches the detector. S1, S2, S3 and S4 are slits with lengths of 4 μm.

The fluorimeter used in the research, from the Photon Technology International (model QM-1), is in the *Optical Spectroscopy Multiuser Laboratory* of the Department of Physics of PUC-Rio and is shown in Figure A.1. The equipment consists of a source(Xenon lamp) emitting electromagnetic radiation, which passes through a first slit, a grating monochromator and comes to the liquid sample after passing through a second slit. The sample is then excited and the emitted electromagnetic radiation passes through a third slit. This light finally comes to another grating monochromator, passes through a fourth slit and reaches a photomultiplier detector system that can detect the electromagnetic radiation in a wavelength range between 185 nm and 680 nm. For this experiment, the slits serve as controllers of the intensity of light and they were used at 4 μm.

In our research, we excited the sample at a wavelength in the range of $300 - 330$ nm to produce an emission spectrum. We decided to excite in

this region, because a liquid with luminescent carbon structures can produce emission spectrum closed to 410 nm [5].

A.2.1 Separation method for PL spectroscopy

This section seeks to present how the samples measured by this experiment were made. The idea of it consists in a separation of the metal-oxide nanoparticles from the transparent liquid, so we could measured a PL spectrum of the last one. However, we weren't able to reproduce the plot present in [5] obtained by a similar separation method for Fe NPs sample.

A.2.1.1 Separation by heating and centrifugation

For the separation of the metal nanoparticles and dispersed organic products, we choose to apply the separation method which consists of heating and centrifuging.

Firstly, we prepared 24 mL of $(NPs)^{mix}$ colloidal dispersion made by PLA with the parameters described in chapter 3, section 3.4. This is equivalent to 2x PLA synthesis by our parameters or, in the case of the double laser ablation, only one.

Following the production of this sample, we put the liquid nanomaterial in the oven at 50^o C and we waited until it concentrated 10 times, which it's equivalent to a quantity of 2.4 mL.

Finally, after the concentration, we put the liquid in the centrifuge at 13000 rpm for 1 h so that the metals nanoparticles could precipitate. At the end of the centrifugation, it was noticed that a transparent liquid which could have dispersed organic material was above the metal NPs in the recipient. Then, we carefully put the transparent liquid in another recipient so that it could be measured.

Bibliography

[1] PATIL, P. P.; PHASE, D. M.; KULKARNI, S. A.; GHAISAS, S. V.; KULKARNI, S. K.; KANETKAR, S. M.; OGALE, S. B. ; BHIDE, V. G.. **Pulsed-laser–induced reactive quenching at liquid-solid interface: Aqueous oxidation of iron**. Phys. Rev. Lett., 58:238–241, Jan 1987.

[2] BARCIKOWSKI, S.; COMPAGNINI, G.. **Advanced nanoparticle generation and excitation by lasers in liquids**. Phys. Chem. Chem. Phys., 15:3022–3026, 2013.

[3] AMENDOLA, V.; MENEGHETTI, M.. **What controls the composition and the structure of nanomaterials generated by laser ablation in liquid solution?** Phys. Chem. Chem. Phys., 15:3027–3046, 2013.

[4] AMENDOLA, V.; MENEGHETTI, M.. **Laser ablation synthesis in solution and size manipulation of noble metal nanoparticles**. Phys. Chem. Chem. Phys., 11:3805–3821, 2009.

[5] TAHIR. **A new paradigm on the pulsed laser ablation of transition metal targets in water: synthesis of carbon sp-sp2 hybridized nanomaterial by CO_2/C reduction**. PhD thesis, Rio de Janeiro, Brasil, 2020.

[6] WANG, H.; TZENG, Y.-K.; JI, Y.; LI, Y.; LI, J.; ZHENG, X.; YANG, A.; LIU, Y.; GONG, Y.; CAI, L.; LI, Y.; ZHANG, X.; CHEN, W.; LIU, B.; LU, H.; MELOSH, N.; SHEN, Z.-X.; CHAN, K.; TAN, T. ; CUI, Y.. **Synergistic enhancement of electrocatalytic CO_2 reduction to C_2 oxygenates at nitrogen-doped nanodiamonds/Cu interface**. Nature Nanotechnology, 15:1–7, 02 2020.

[7] WANG, X.; LI, S.; YU, H.; YU, J. ; LIU, S.. **Ag_2O as a New Visible-Light Photocatalyst: Self-Stability and High Photocatalytic Activity**. Chemistry – A European Journal, 17(28):7777–7780, 2011.

[8] STEINFELD, A.; SANDERS, S. ; PALUMBO, R.. **Design aspects of solar thermochemical engineering—a case study: Two-step**

water-splitting cycle using the Fe_3O_4/FeO redox system. Solar Energy, 65(1):43–53, 1999.

[9] HEROLD, F.; PROSCH, S.; OEFNER, N.; BRUNNENGRÄBER, K.; LEUBNER, O.; HERMANS, Y.; HOFMANN, K.; DROCHNER, A.; HOFMANN, J. P.; QI, W. ; OTHERS. **Nanoscale Hybrid Amorphous/Graphitic Carbon as Key Towards Next-Generation Carbon-Based Oxidative Dehydrogenation Catalysts**. Angewandte Chemie International Edition, 60(11):5898–5906, 2021.

[10] FREDRIKSSON, H.. **Nanostructures of Graphite and Amorphous Carbon-Fabrication and Properties**. Chalmers Tekniska Hogskola (Sweden), 2009.

[11] ZANG, X.; DAI, Z.; GUO, J.; DONG, Q.; YANG, J.; HUANG, W. ; DONG, X.. **Controllable synthesis of triangular $Ni(HCO_3)_2$ nanosheets for supercapacitor**. Nano Research, 9(5):1358–1365, 2016.

[12] BEN HU, HUA GUO, P. Z.; SHI, Z.-L.. **Characteristics of SARS-CoV-2 and COVID-19**. Nat Rev Microbiol 19, p. 141–154, 2021.

[13] VAHABZADEH, E.; TORKAMANY, M.. **Iron oxide nanocrystals synthesis by laser ablation in water: Effect of laser wavelength**. Journal of Cluster Science, 25(4):959–968, 2014.

[14] MAHFOUZ, R.; CADETE SANTOS AIRES, F.; BRENIER, A.; JACQUIER, B. ; BERTOLINI, J.. **Synthesis and physico-chemical characteristics of nanosized particles produced by laser ablation of a nickel target in water**. Applied Surface Science, 254(16):5181 – 5190, 2008.

[15] PRABU, S. L.; SURIYAPRAKASH, T. N. K. ; THIRUMURUGAN, R.. **Medicated nanoparticle for gene delivery**. In: ADVANCED TECHNOLOGY FOR DELIVERING THERAPEUTICS. IntechOpen, 2017.

[16] MENDES, R.; FERNANDES, A. R. ; BAPTISTA, P. V.. **Gold Nanoparticle Approach to the Selective Delivery of Gene Silencing in Cancer—The Case for Combined Delivery?** Genes, 8(3), 2017.

[17] SASAKI, S.; NAKAMURA, K.; HAMABE, Y.; KURAHASHI, E. ; HIROI, T.. **Production of iron nanoparticles by laser irradiation in a simulation of lunar-like space weathering**. Nature, 410(6828):555–557, 2001.

[18] BRUNETTO, R.; ROMANO, F.; BLANCO, A.; FONTI, S.; MARTINO, M.; OROFINO, V. ; VERRIENTI, C.. **Space weathering of silicates simulated by nanosecond pulse uv excimer laser**. Icarus, 180(2):546–554, 2006.

[19] ET AL., F. D.. **"micrometeorite bombardment simulated by ns-pulsed laser ablation: morphological characterization of the impact craters"**. Icarus., 2020.

[20] FULVIO, D.; GÓBI, S.; JÄGER, C.; KERESZTURI, Á. ; HENNING, T.. **Laboratory experiments on the low-temperature formation of carbonaceous grains in the ISM**. The Astrophysical Journal Supplement Series, 233(1):14, 2017.

[21] OLEARY, B.; GAFFEY, M. J.; ROSS, D. J. ; SALKELD, R.. **Retrieval of asteroidal materials**. Space Resources and Space Settlements, p. 173–189, 1979.

[22] MILER, M.; GOSAR, M.. **Mineral and chemical composition of the new iron meteorite Javorje from Slovenia**. Meteoritics & Planetary Science, 46(12):1939–1946, 2011.

[23] IRWIN, J. A.. **Astrophysics: decoding the cosmos**. John Wiley & Sons, 2021.

[24] KRESS, M. E.; TIELENS, A. G. G. M.. **The role of Fischer-Tropsch catalysis in solar nebula chemistry**. Meteoritics & Planetary Science, 36(1):75–91, 2001.

[25] SEKINE, Y.; SUGITA, S.; SHIDO, T.; YAMAMOTO, T.; IWASAWA, Y.; KADONO, T. ; MATSUI, T.. **An experimental study on Fischer-Tropsch catalysis: Implications for impact phenomena and nebular chemistry**. Meteoritics & Planetary Science, 41(5):715–729, 2006.

[26] HAACK, H.; MCCOY, T. J.. **Iron and stony-iron meteorites**. Meteorites, Comets and Planets (ed. AM Davis) Vol. 1 Treatise on Geochemistry, 2003.

[27] VLADOIU, I.; STAFE, M.; NEGUTU, C. ; POPESCU, I.. **Influence of the pulse number and fluence of a nanosecond laser on the ablation rate of metals, semiconductors and dielectrics**. The European Physical Journal Applied Physics, 47(3):30702, 2009.

[28] KIM, M.; OSONE, S.; KIM, T.; HIGASHI, H. ; SETO, T.. **Synthesis of Nanoparticles by Laser Ablation: A Review**. KONA Powder and Particle Journal, advpub, 2017.

[29] SHOWSTACK, R.. **Carbon dioxide tops 400 ppm at Mauna Loa, Hawaii**, 2013.

[30] ALMEIDA, J. M. P.; ALMEIDA, G. F. B.; BONI, L. ; MENDONÇA, C. R.. **Nonlinear Optical Properties and Femtosecond Laser Micromachining of Special Glasses**. Journal of the Brazilian Chemical Society, 26:2418 – 2429, 12 2015.

[31] AL-HADDAD, R. M.; IBRAHIM, I. M. ; KHALID, A. H.. **The study of the nonlinear optical properties of copper nanopartical prepared by pulse laser ablation PLA**. 2014.

[32] SIMAKIN, A. V.; ASTASHEV, M. E.; BAIMLER, I. V.; UVAROV, O. V.; VORONOV, V. V.; VEDUNOVA, M. V.; SEVOST'YANOV, M. A.; BELOSLUDTSEV, K. N. ; GUDKOV, S. V.. **The effect of gold nanoparticle concentration and laser fluence on the laser-induced water decomposition**. The Journal of Physical Chemistry B, 123(8):1869–1880, 2019.

[33] POMMERET, S.; GOBERT, F.; MOSTAFAVI, M.; LAMPRE, I. ; MIALOCQ, J.-C.. **Femtochemistry of the hydrated electron at decimolar concentration**. The Journal of Physical Chemistry A, 105(51):11400–11406, 2001.

[34] FENG, Q.; MOLONEY, J. V.; NEWELL, A. C.; WRIGHT, E. M.; COOK, K.; KENNEDY, P. K.; HAMMER, D.; ROCKWELL, B. ; THOMPSON, C.. **Theory and simulation on the threshold of water breakdown induced by focused ultrashort laser pulses**. IEEE journal of quantum electronics, 33(2):127–137, 1997.

[35] VOGEL, A.; NOACK, J.; NAHEN, K.; THEISEN, D.; BUSCH, S.; PARLITZ, U.; HAMMER, D.; NOOJIN, G.; ROCKWELL, B. ; BIRNGRUBER, R.. **Energy balance of optical breakdown in water at nanosecond to femtosecond time scales.** Applied Physics B: Lasers & Optics, 68(2), 1999.

[36] MOMMA, C.; CHICHKOV, B. N.; NOLTE, S.; VON ALVENSLEBEN, F.; TÜNNERMANN, A.; WELLING, H. ; WELLEGEHAUSEN, B.. **Short-**

pulse laser ablation of solid targets. Optics Communications, 129(1):134 – 142, 1996.

[37] VANALAKAR, S.; AGAWANE, G.; SHIN, S.; SURYAWANSHI, M.; GURAV, K.; JEON, K.; PATIL, P.; JEONG, C.; KIM, J. ; KIM, J.. **A review on pulsed laser deposited CZTS thin films for solar cell applications**. Journal of Alloys and Compounds, 619:109–121, 2015.

[38] MIOTELLO, A.; KELLY, R.. **Laser-induced phase explosion: new physical problems when a condensed phase approaches the thermodynamic critical temperature**. Applied Physics A: Materials Science & Processing, 69(7):67–73, Jan. 1999.

[39] SANO, Y.; MUKAI, N.; OKAZAKI, K. ; OBATA, M.. **Residual stress improvement in metal surface by underwater laser irradiation**. Nuclear Instruments and Methods in Physics Research Section B: Beam Interactions with Materials and Atoms, 121(1):432 – 436, 1997. Materials Synthesis and Modification by Ion and/or Laser Beams.

[40] TACCOGNA, F.. **Nucleation and growth of nanoparticles in a plasma by laser ablation in liquid**. Journal of Plasma Physics, 81(5):495810509, 2015.

[41] ITINA, T. E.. **On Nanoparticle Formation by Laser Ablation in Liquids**. The Journal of Physical Chemistry C, 115(12):5044–5048, 2011.

[42] DE GIACOMO, A.; DELL'AGLIO, M.; DE PASCALE, O. ; CAPITELLI, M.. **From single pulse to double pulse ns-Laser Induced Breakdown Spectroscopy under water: Elemental analysis of aqueous solutions and submerged solid samples**. Spectrochimica Acta Part B: Atomic Spectroscopy, 62(8):721 – 738, 2007.

[43] WAGENER, P.; IBRAHIMKUTTY, S.; MENZEL, A.; PLECH, A. ; BARCIKOWSKI, S.. **Dynamics of silver nanoparticle formation and agglomeration inside the cavitation bubble after pulsed laser ablation in liquid**. Physical Chemistry Chemical Physics, 15(9):3068–3074, 2013.

[44] KALUS, M.-R.; LANYUMBA, R.; LORENZO-PARODI, N.; JOCHMANN, M. A.; KERPEN, K.; HAGEMANN, U.; SCHMIDT, T. C.; BARCIKOWSKI, S. ; GÖKCE, B.. **Determining the role of redox-active materials during laser-induced water decomposition**. Phys. Chem. Chem. Phys., 21:18636–18651, 2019.

[45] KALUS, M.-R.; REIMER, V.; BARCIKOWSKI, S. ; GÖKCE, B.. **Discrimination of effects leading to gas formation during pulsed laser ablation in liquids**. Applied Surface Science, 465:1096–1102, 2019.

[46] KIM, J.; REDDY, D. A.; MA, R. ; KIM, T. K.. **The influence of laser wavelength and fluence on palladium nanoparticles produced by pulsed laser ablation in deionized water**. Solid state sciences, 37:96–102, 2014.

[47] LASEMI, N.; BOMATI MIGUEL, O.; LAHOZ, R.; LENNIKOV, V. V.; PACHER, U.; RENTENBERGER, C. ; KAUTEK, W.. **Laser-Assisted Synthesis of Colloidal FeW_xO_y and Fe/Fe_xO_y Nanoparticles in Water and Ethanol**. ChemPhysChem, 19(11):1414–1419, 2018.

[48] LASEMI, N.; PACHER, U.; RENTENBERGER, C.; BOMATÍ-MIGUEL, O. ; KAUTEK, W.. **Laser-assisted synthesis of colloidal Ni/NiO_x core/shell nanoparticles in water and alcoholic solvents**. ChemPhysChem, 18(9):1118–1124, 2017.

[49] MUSAEV, O.; YAN, J.; DUSEVICH, V.; WROBEL, J. ; KRUGER, M.. **Ni nanoparticles fabricated by laser ablation in water**. Applied Physics A, 116(2):735–739, 2014.

[50] TOMITA, Y.; TSUBOTA, M. ; AN-NAKA, N.. **Energy evaluation of cavitation bubble generation and shock wave emission by laser focusing in liquid nitrogen**. Journal of Applied Physics, 93(5):3039–3048, 2003.

[51] DE BONIS, A.; LOVAGLIO, T.; GALASSO, A.; SANTAGATA, A. ; TEGHIL, R.. **Iron and iron oxide nanoparticles obtained by ultra-short laser ablation in liquid**. Applied Surface Science, 353:433–438, 2015.

[52] NAIL, B. A.; FIELDS, J. M.; ZHAO, J.; WANG, J.; GREANEY, M. J.; BRUTCHEY, R. L. ; OSTERLOH, F. E.. **Nickel Oxide Particles Catalyze Photochemical Hydrogen Evolution from Water—Nanoscaling Promotes P-Type Character and Minority Carrier Extraction**. ACS Nano, 9(5):5135–5142, 2015. PMID: 25872576.

[53] GLEESON, B.; HADAVI, S. ; YOUNG, D.. **Isothermal transformation behavior of thermally-grown wüstite**. Materials at High Temperatures, 17:311–319, 05 2000.

[54] GIANNAKIS, S.; LIU, S.; CARRATALÀ, A.; RTIMI, S.; TALEBI AMIRI, M.; BENSIMON, M. ; PULGARIN, C.. **Iron oxide-mediated semiconductor photocatalysis vs. heterogeneous photo-Fenton treatment of viruses in wastewater. Impact of the oxide particle size.** Journal of Hazardous Materials, 339:223 – 231, 2017.

[55] LI, J.; CHU, D.. **4 - Energy band engineering of metal oxide for enhanced visible light absorption**. In: Lin, Z.; Ye, M. ; Wang, M., editors, MULTIFUNCTIONAL PHOTOCATALYTIC MATERIALS FOR ENERGY, Woodhead Publishing in Materials, p. 49–78. Woodhead Publishing, 2018.

[56] BABAY, S.; MHIRI, T. ; TOUMI, M.. **Synthesis, structural and spectroscopic characterizations of maghemite γ-Fe_2O_3 prepared by one-step coprecipitation route**. Journal of Molecular Structure, 1085:286 – 293, 2015.

[57] LITTER, M. I.; BLESA, M. A.. **Photodissolution of iron oxides. IV. A comparative study on the photodissolution of hematite, magnetite, and maghemite in EDTA media**. Canadian Journal of Chemistry, 70(9):2502–2510, 1992.

[58] LIU, H.; DI VALENTIN, C.. **Band gap in magnetite above Verwey temperature induced by symmetry breaking**. The Journal of Physical Chemistry C, 121(46):25736–25742, 2017.

[59] HOSNY, N. M.. **Synthesis, characterization and optical band gap of NiO nanoparticles derived from anthranilic acid precursors via a thermal decomposition route**. Polyhedron, 30(3):470 – 476, 2011.

[60] CHEN, S.; TAKATA, T. ; DOMEN, K.. **Particulate photocatalysts for overall water splitting**. Nature Reviews Materials, 2:natrevmats201750, 08 2017.

[61] KAYANI, Z.; RIAZ, S.; NASEEM, S. ; ZIA, R.. **Synthesis and characterization of Ni_2O_3 Thin Films**. 08 2016.

[62] SUZUKI, H.; OGURA, N.; KANEKO, T. ; KATO, T.. **Highly Stable Persistent Photoconductivity with Suspended Graphene Nanoribbons**. Scientific Reports, 8, 12 2018.

[63] HALL, D. S.; LOCKWOOD, D. J.; BOCK, C. ; MACDOUGALL, B. R.. **Nickel hydroxides and related materials: a review of their structures, synthesis and properties**. Proceedings of the Royal Society A: Mathematical, Physical and Engineering Sciences, 471(2174):20140792, 2015.

[64] HALL, D. S.; LOCKWOOD, D. J.; POIRIER, S.; BOCK, C. ; MACDOUGALL, B. R.. **Raman and infrared spectroscopy of α and β phases of thin nickel hydroxide films electrochemically formed on nickel**. The Journal of Physical Chemistry A, 116(25):6771–6784, 2012.

[65] LIU, Z.; MA, R.; OSADA, M.; TAKADA, K. ; SASAKI, T.. **Selective and controlled synthesis of α-and β-cobalt hydroxides in highly developed hexagonal platelets**. Journal of the American Chemical Society, 127(40):13869–13874, 2005.

[66] DAI, S.; ZHANG, Z.; XU, J.; SHEN, W.; ZHANG, Q.; YANG, X.; XU, T.; DANG, D.; HU, H.; ZHAO, B. ; OTHERS. **In situ Raman study of nickel bicarbonate for high-performance energy storage device**. Nano Energy, 64:103919, 2019.

[67] AMENDOLA, V.; RIELLO, P.; POLIZZI, S.; FIAMENI, S.; INNOCENTI, C.; SANGREGORIO, C. ; MENEGHETTI, M.. **Magnetic iron oxide nanoparticles with tunable size and free surface obtained via a "green" approach based on laser irradiation in water**. J. Mater. Chem., 21:18665–18673, 2011.

[68] AMENDOLA, V.; MENEGHETTI, M.; GRANOZZI, G.; AGNOLI, S.; POLIZZI, S.; RIELLO, P.; BOSCAINI, A.; ANSELMI, C.; FRACASSO, G.; COLOMBATTI, M.; INNOCENTI, C.; GATTESCHI, D. ; SANGREGORIO, C.. **Top-down synthesis of multifunctional iron oxide nanoparticles for macrophage labelling and manipulation**. J. Mater. Chem., 21:3803–3813, 2011.

[69] AMENDOLA, V.; AMANS, I. D.; ISHIKAWA, Y.; KOSHIZAKI, N.; SCIRÈ, S.; COMPAGNINI, G.; REICHENBERGER, S. ; BARCIKOWSKI, I. S.. **Room-Temperature Laser Synthesis in Liquid of Oxide, Metal-Oxide Core-Shells, and Doped Oxide Nanoparticles**. Chemistry (Weinheim an der Bergstrasse, Germany), 26(42):9206, 2020.

[70] GELLINI, C.; DEEPAK, F. L.; MUNIZ-MIRANDA, M.; CAPORALI, S.; MUNIZ-MIRANDA, F.; PEDONE, A.; INNOCENTI, C. ; SANGREGORIO,

C.. **Magneto-plasmonic colloidal nanoparticles obtained by laser ablation of nickel and silver targets in water**. The Journal of Physical Chemistry C, 121(6):3597–3606, 2017.

[71] LIU, B.; HU, Z.; CHE, Y.; CHEN, Y. ; PAN, X.. **Nanoparticle generation in ultrafast pulsed laser ablation of nickel**. Applied Physics Letters, 90(4):044103, 2007.

[72] WU, J.; HUANG, Y.; YE, W. ; LI, Y.. **CO_2 reduction: from the electrochemical to photochemical approach**. Advanced Science, 4(11):1700194, 2017.

[73] THAUER, R. K.; JUNGERMANN, K. ; DECKER, K.. **Energy conservation in chemotrophic anaerobic bacteria**. Bacteriological reviews, 41(1):100–180, 1977.

[74] MISTRY, H.; RESKE, R.; ZENG, Z.; ZHAO, Z.-J.; GREELEY, J.; STRASSER, P. ; CUENYA, B. R.. **Exceptional size-dependent activity enhancement in the electroreduction of CO_2 over Au nanoparticles**. Journal of the American Chemical Society, 136(47):16473–16476, 2014.

[75] AMENDOLA, V.; MENEGHETTI, M.. **Laser ablation synthesis in solution and size manipulation of noble metal nanoparticles**. Physical chemistry chemical physics, 11(20):3805–3821, 2009.

[76] KALUS, M.-R.; BÄRSCH, N.; STREUBEL, R.; GÖKCE, E.; BARCIKOWSKI, S. ; GÖKCE, B.. **How persistent microbubbles shield nanoparticle productivity in laser synthesis of colloids–quantification of their volume, dwell dynamics, and gas composition**. Physical Chemistry Chemical Physics, 19(10):7112–7123, 2017.

[77] BARMINA, E.; GUDKOV, S.; SIMAKIN, A. ; SHAFEEV, G.. **Stable products of laser-induced breakdown of aqueous colloidal solutions of nanoparticles**. arXiv preprint arXiv:1707.02357, 2017.

[78] CUELLAR, N. R.; SCHERER, C.; KAÇKAR, B.; EISENREICH, W.; HUBER, C.; WIESNER-FLEISCHER, K.; FLEISCHER, M. ; HINRICHSEN, O.. **Two-step electrochemical reduction of CO_2 towards multi-carbon products at high current densities**. Journal of CO2 Utilization, 36:263–275, 2020.

[79] DRAB, D. M.; WILLAUER, H. D.; OLSEN, M. T.; ANANTH, R.; MUSHRUSH, G. W.; BALDWIN, J. W.; HARDY, D. R. ; WILLIAMS, F. W..

Hydrocarbon synthesis from carbon dioxide and hydrogen: A two-step process. Energy & fuels, 27(11):6348–6354, 2013.

[80] ROY, S.; CHEREVOTAN, A. ; PETER, S. C.. **Thermochemical CO_2 hydrogenation to single carbon products: scientific and technological challenges**. ACS Energy Letters, 3(8):1938–1966, 2018.

[81] HANNULA, I.; KAISALO, N. ; SIMELL, P.. **Preparation of Synthesis Gas from CO_2 for Fischer–Tropsch Synthesis—Comparison of Alternative Process Configurations**. C, 6(3):55, 2020.

[82] PAN, B.; XIAO, J.; LI, J.; LIU, P.; WANG, C. ; YANG, G.. **Carbyne with finite length: The one-dimensional sp carbon**. Science Advances, 1(9), 2015.

[83] YU, H.; LI, X.; ZENG, X. ; LU, Y.. **Preparation of carbon dots by non-focusing pulsed laser irradiation in toluene**. Chemical Communications, 52(4):819–822, 2015.

[84] LEE, S. H.; JUNG, H. J.; LEE, S. J.; THEERTHAGIRI, J.; KIM, T. H. ; CHOI, M. Y.. **Selective synthesis of Au and graphitic carbon-encapsulated Au (Au@ GC) nanoparticles by pulsed laser ablation in solvents: Catalytic Au and acid-resistant Au@ GC nanoparticles**. Applied Surface Science, 506:145006, 2020.

[85] LLAMAS-JANSA, I.; JÄGER, C.; MUTSCHKE, H. ; HENNING, T.. **Far-ultraviolet to near-infrared optical properties of carbon nanoparticles produced by pulsed-laser pyrolysis of hydrocarbons and their relation with structural variations**. Carbon, 45(7):1542–1557, 2007.

[86] ROBERTSON, J.. **Amorphous carbon**. Advances in physics, 35(4):317–374, 1986.

[87] MCNAUGHT, A. D.; WILKINSON, A. ; OTHERS. **Compendium of chemical terminology**, volumen 1669. Blackwell Science Oxford, 1997.

[88] ROBERTSON, J.; O'REILLY, E.. **Electronic and atomic structure of amorphous carbon**. Physical Review B, 35(6):2946, 1987.

[89] EMAMIAN, S.; HUSSAIN, P.; AWANG, M.; ARUMUGAM, T.; YUSOF, F.; SAHEED, M. ; MOHAMED, N.. **Comparison of carbon-based nanomaterials characteristics on H13 tool steel: Vergleich der Eigenschaften Kohlenstoff-basierter Nanomaterialien auf**

H13 Werkzeugstahl. Materialwissenschaft und Werkstofftechnik, 48(3-4):198–204, 2017.

[90] KRESS, M. E.; MCKAY, C. P.. **Formation of methane in comet impacts: implications for Earth, Mars, and Titan**. Icarus, 168(2):475 – 483, 2004.

[91] CHEN, X.; LI, A. ; ZHANG, K.. **On Graphene in the Interstellar Medium**. The Astrophysical Journal, 850(1):104, 2017.

[92] PIZZARELLO, S.; COOPER, G. ; FLYNN, G.. **The nature and distribution of the organic material in carbonaceous chondrites and interplanetary dust particles**. Meteorites and the early solar system II, 1:625–651, 2006.

[93] CRONIN, J. R.; PIZZARELLO, S.. **Aliphatic hydrocarbons of the Murchison meteorite**. Geochimica et Cosmochimica Acta, 54(10):2859–2868, 1990.

[94] SEKINE, Y.; SUGITA, S.; KADONO, T. ; MATSUI, T.. **Methane production by large iron meteorite impacts on early Earth**. Journal of Geophysical Research: Planets, 108(E7), 2003.

[95] ZOLENSKY, M.; BLAND, P.; BROWN, P. ; HALLIDAY, I.. **Flux of extraterrestrial materials**. Meteorites and the early solar system II, 943:869–888, 2006.

[96] OBERG, K. I.. **Photochemistry and astrochemistry: Photochemical pathways to interstellar complex organic molecules**. Chemical reviews, 116(17):9631–9663, 2016.

[97] HERBST, E.. **The synthesis of large interstellar molecules**. International Reviews in Physical Chemistry, 36(2):287–331, 2017.

[98] SANDFORD, S. A.; NUEVO, M.; BERA, P. P. ; LEE, T. J.. **Prebiotic astrochemistry and the formation of molecules of astrobiological interest in interstellar clouds and protostellar disks**. Chemical reviews, 120(11):4616–4659, 2020.

[99] GIBB, E. L.; WHITTET, D. C. B.; BOOGERT, A. C. A. ; TIELENS, A. G. G. M.. **Interstellar Ice: The Infrared Space Observatory Legacy**. The Astrophysical Journal Supplement Series, 151(1):35–73, mar 2004.

[100] MCGUIRE, B. A.. **2018 census of interstellar, circumstellar, extragalactic, protoplanetary disk, and exoplanetary molecules**. The Astrophysical Journal Supplement Series, 239(2):17, 2018.

[101] CHAN, G. H.; ZHAO, J.; SCHATZ, G. C. ; VAN DUYNE, R. P.. **Localized surface plasmon resonance spectroscopy of triangular aluminum nanoparticles**. The Journal of Physical Chemistry C, 112(36):13958–13963, 2008.

[102] ZAMAN, Q.; SOUZA, J.; PANDOLI, O.; COSTA, K. Q.; DMITRIEV, V.; FULVIO, D.; CREMONA, M.; AUCELIO, R. Q.; FONTES, G. ; DEL ROSSO, T.. **Two-color surface plasmon resonance nanosizer for gold nanoparticles**. Optics express, 27(3):3200–3216, 2019.

[103] IWAMOTO, T.; ISHIGAKI, T.. **Fabrication of iron oxide nanoparticles using laser ablation in liquids**. In: JOURNAL OF PHYSICS: CONFERENCE SERIES, volumen 441, p. 012034. IOP Publishing, 2013.

[104] CAZZANELLI, E.; KUZMIN, A.; MARIOTTO, G. ; MIRONOVA-ULMANE, N.. **Study of vibrational and magnetic excitations in NicMg1-cO solid solutions by Raman spectroscopy**. Journal of Physics: Condensed Matter, 15(12):2045, 2003.

[105] MURLI, C.; SHARMA, S. M.; KULSHRESHTHA, S. ; SIKKA, S.. **High-pressure behavior of β-Ni(OH)$_2$—a Raman scattering study**. Physica B: Condensed Matter, 307(1-4):111–116, 2001.

[106] HERMET, P.; GOURRIER, L.; BANTIGNIES, J.-L.; RAVOT, D.; MICHEL, T.; DEABATE, S.; BOULET, P. ; HENN, F.. **Dielectric, magnetic, and phonon properties of nickel hydroxide**. Physical Review B, 84(23):235211, 2011.

[107] TUSCHEL, D.. **Practical group theory and raman spectroscopy, part i: Normal vibrational modes**. Spectroscopy, 29(2):14, 2014.

[108] GEISLER, T.; DOHMEN, L.; LENTING, C. ; FRITZSCHE, M. B.. **Real-time in situ observations of reaction and transport phenomena during silicate glass corrosion by fluid-cell Raman spectroscopy**. Nature materials, 18(4):342–348, 2019.

[109] LEONTYEVA, D.; LEONTYEV, I.; AVRAMENKO, M.; YUZYUK, Y. I.; KUKUSHKINA, Y. A. ; SMIRNOVA, N.. **Electrochemical dispergation as a simple and effective technique toward preparation of**

NiO based nanocomposite for supercapacitor application. Electrochimica Acta, 114:356–362, 2013.

[110] MIRONOVA-ULMANE, N.; KUZMIN, A.; STEINS, I.; GRABIS, J.; SILDOS, I. ; PÄRS, M.. **Raman scattering in nanosized nickel oxide NiO**. In: JOURNAL OF PHYSICS: CONFERENCE SERIES, volumen 93, p. 012039. IOP Publishing, 2007.

[111] MA, W.; WANG, L.; XUE, J. ; CUI, H.. **A bottom-up strategy for exfoliation-free synthesis of soluble α-Ni(OH)$_2$ monolayer nanosheets on a large scale**. RSC advances, 6(88):85367–85373, 2016.

[112] DUBAL, D.; FULARI, V. ; LOKHANDE, C.. **Effect of morphology on supercapacitive properties of chemically grown β-Ni(OH)$_2$ thin films**. Microporous and Mesoporous Materials, 151:511–516, 2012.

[113] CAI, G.-B.; CHEN, S.-F.; LIU, L.; JIANG, J.; YAO, H.-B.; XU, A.-W. ; YU, S.-H.. **1, 3-Diamino-2-hydroxypropane-N, N, N´, N´-tetraacetic acid stabilized amorphous calcium carbonate: nucleation, transformation and crystal growth**. CrystEngComm, 12(1):234–241, 2010.

[114] EBAJO, V. D.; SANTOS, C. R. L.; ALEA, G. V.; LIN, Y. A. ; CHEN, C.-H.. **Regenerable acidity of graphene oxide in promoting multicomponent organic synthesis**. Scientific reports, 9(1):1–12, 2019.

[115] TITELMAN, G.; GELMAN, V.; BRON, S.; KHALFIN, R.; COHEN, Y. ; BIANCO-PELED, H.. **Characteristics and microstructure of aqueous colloidal dispersions of graphite oxide**. Carbon, 43(3):641–649, 2005.

[116] KIELY, C. J.. **Electron microscopy and analysis 1999: proceedings of the Institute of Physics Electron Microscopy and Analysis Group conference, University of Sheffield, 24-27 August 1999**, volumen 161. CRC Press, 1999.

[117] NITIPUTRI, K.; RAMASSE, Q. M.; AUTEFAGE, H.; MCGILVERY, C. M.; BOONRUNGSIMAN, S.; EVANS, N. D.; STEVENS, M. M. ; PORTER, A. E.. **Nanoanalytical electron microscopy reveals a sequential mineralization process involving carbonate-containing amorphous precursors**. ACS nano, 10(7):6826–6835, 2016.

[118] PAL, R.; BOURGEOIS, L.; WEYLAND, M.; SIKDER, A. K.; SAITO, K.; FUNSTON, A. M. ; BELLARE, J. R.. **Chemical fingerprinting of**

polyvinyl acetate and polycarbonate using electron energy-loss spectroscopy. Polymer Chemistry, 11(34):5484–5492, 2020.

[119] GRUNES, L.; LEAPMAN, R.; WILKER, C.; HOFFMANN, R. ; KUNZ, A.. **Oxygen K near-edge fine structure: An electron-energy-loss investigation with comparisons to new theory for selected 3 d Transition-metal oxides**. Physical Review B, 25(12):7157, 1982.

[120] RUI, X.; WALTER, J.; LEIGHTON, C. ; KLIE, R.. **Atomic-resolution study of oxygen vacancy ordering in Lao. 5Sro. 5CoO_3-s thin films on $SrTiO_3$ during in situ cooling experiments.** Microscopy and Microanalysis, 24(S1):84–85, 2018.

[121] ALMEIDA, T. P.; KASAMA, T.; MUXWORTHY, A. R.; WILLIAMS, W.; NAGY, L.; HANSEN, T. W.; BROWN, P. D. ; DUNIN-BORKOWSKI, R. E.. **Visualized effect of oxidation on magnetic recording fidelity in pseudo-single-domain magnetite particles**. Nature Communications, 5(1):1–6, 2014.

[122] CHEN, S.-Y.; GLOTER, A.; ZOBELLI, A.; WANG, L.; CHEN, C.-H. ; COLLIEX, C.. **Electron energy loss spectroscopy and ab initio investigation of iron oxide nanomaterials grown by a hydrothermal process**. Physical Review B, 79(10):104103, 2009.

[123] VIDALI, G.. **Cosmic low temperature physics: Making molecules on stardust**. Journal of Low Temperature Physics, 170(1):1–30, 2013.

[125] SCOTT, E. R. D.; WASSON, J. T.. **Classification and properties of iron meteorites**. Reviews of Geophysics, 13(4):527–546, 1975.

[126] CABEDO, V.; LLORCA, J.; TRIGO-RODRÍGUEZ, J. M. ; RIMOLA, A.. **Study of Fischer-Tropsch Type reactions on chondritic meteorites**. arXiv preprint arXiv:2105.08498, 2021.

[127] CAMPINS, H.; HARGROVE, K.; PINILLA-ALONSO, N.; HOWELL, E. S.; KELLEY, M. S.; LICANDRO, J.; MOTHÉ-DINIZ, T.; FERNÁNDEZ, Y. ; ZIFFER, J.. **Water ice and organics on the surface of the asteroid 24 Themis**. Nature, 464(7293):1320–1321, 2010.

[128] MERLIN, F.; QUIRICO, E.; BARUCCI, M. ; DE BERGH, C.. **Methanol ice on the surface of minor bodies in the solar system**. Astronomy & Astrophysics, 544:A20, 2012.

[129] DANGER, G.; FRESNEAU, A.; ABOU MRAD, N.; DE MARCELLUS, P.; ORTHOUS-DAUNAY, F.-R.; DUVERNAY, F.; VUITTON, V.; D'HENDECOURT, L. L. S.; THISSEN, R. ; CHIAVASSA, T.. **Insight into the molecular composition of laboratory organic residues produced from interstellar/pre-cometary ice analogues using very high resolution mass spectrometry**. Geochimica et Cosmochimica Acta, 189:184–196, 2016.

[130] JIMÉNEZ-ESCOBAR, A.; CARO, G. M.. **Sulfur depletion in dense clouds and circumstellar regions-I. H_2S ice abundance and UV-photochemical reactions in the H_2O-matrix**. Astronomy & Astrophysics, 536:A91, 2011.

[131] LONG, D. A.. **Introductory Raman Spectroscopy. John R. Ferraro, Kazuo Nakamoto and Chris W. Brown. Academic Press, Amsterdam, Second Edition, 2003. xiii + 434**. Journal of Raman Spectroscopy, 36(10):1012–1012, 2005.

[132] WILLIAMS, D.; CARTER, C.. **Transmission Electron Microscopy: A Textbook for Materials Science**, volumen III. 06 2009.

[133] MUTO, H.; MIYAJIMA, K. ; MAFUNE, F.. **Mechanism of laser-induced size reduction of gold nanoparticles as studied by single and double laser pulse excitation**. The Journal of Physical Chemistry C, 112(15):5810–5815, 2008.

[134] GIAMMANCO, F.; GIORGETTI, E.; MARSILI, P. ; GIUSTI, A.. **Experimental and theoretical analysis of photofragmentation of Au nanoparticles by picosecond laser radiation**. The Journal of Physical Chemistry C, 114(8):3354–3363, 2010.

[135] TOMKO, J.; NADDEO, J. J.; JIMENEZ, R.; TAN, Y.; STEINER, M.; FITZ-GERALD, J. M.; BUBB, D. M. ; O'MALLEY, S. M.. **Size and polydispersity trends found in gold nanoparticles synthesized by laser ablation in liquids**. Physical Chemistry Chemical Physics, 17(25):16327–16333, 2015.

[136] GAUTHIER, M. A.; STANGEL, I.; ELLIS, T. H. ; ZHU, X.. **A new method for quantifying the intensity of the C= C band of dimethacrylate dental monomers in their FTIR and Raman spectra**. Biomaterials, 26(33):6440–6448, 2005.

[137] DE GIACOMO, A.; DELL'AGLIO, M.; SANTAGATA, A.; GAUDIUSO, R.; DE PASCALE, O.; WAGENER, P.; MESSINA, G.; COMPAGNINI, G. ; BARCIKOWSKI, S.. **Cavitation dynamics of laser ablation of bulk and wire-shaped metals in water during nanoparticles production**. Physical Chemistry Chemical Physics, 15(9):3083–3092, 2013.

[138] PALUMBO, M.; BARATTA, G.; FULVIO, D.; GAROZZO, M.; GOMIS, O.; LETO, G.; SPINELLA, F. ; STRAZZULLA, G.. **Ion irradiation of astrophysical ices**. In: JOURNAL OF PHYSICS: CONFERENCE SERIES, volumen 101, p. 012002. IOP Publishing, 2008.

[139] PARTHASARATHY, G.; SREEDHAR, B. ; CHETTY, T.. **Spectroscopic and X-ray diffraction studies on fluid deposited rhombohedral graphite from the Eastern Ghats Mobile Belt, India**. 2006.

[140] MIRONOVA-ULMANE, N.; KUZMIN, A.; GRABIS, J.; SILDOS, I.; VORONIN, V.; BERGER, I. ; KAZANTSEV, V.. **Structural and magnetic properties of nickel oxide nanopowders**. In: SOLID STATE PHENOMENA, volumen 168, p. 341–344. Trans Tech Publ, 2011.

[141] BUDDHUE, J.. **The oxidation and weathering of meteorites. Univ. New Mexico Publ**. Meteoritics, 3:1–161, 1957.